UNIVERSITÀ DEGLI STUDI DI MILANO

Department of Medical Biotechnology and Translational Medicine

PhD school in
Physics, Astrophysics, and Applied Physics

Cycle XXXVII

Yielding phenomena in microgel suspensions across length scales

SSD PHYS-06/A

Director of the School: Prof. Aniello Mennella

Supervisor: Prof. Giuliano Zanchetta

Co-supervisor: Dr. Marco Caggioni

PhD Thesis of:
Afshin Azarpour

Academic Year 2024/2025

First, to Imam Zaman
Second, to the luminous hearts of my world:
Fatemeh, Rosa, Shirin, and Fereshteh

"Certainly We wrote in the Psalms, after the Torah: Indeed My righteous servants shall inherit the earth."
(Al-Anbiyaa 21:105)

Committee of the final examination:

Professor Giampaolo Mistura (Università di Padova)

Professor Rossana Pasquino (Università di Napoli F̈ederico IIÿ)

Professor Stefano Buzzaccaro (Politecnico di Milano)

Final examination:

Date: 07/04/2025

Università degli Studi di Milano, Milan, Italy

Contents

Summary and motivation

Most of the materials we encounter in our everyday life, such as food or personal care products, are complex fluids with a non-trivial mechanical behavior, including coexistence of viscous and elastic features and different responses on various time scales or to different stress levels. These properties represent a constitutive part of the action of such materials and of our perception, from spreadability to mouth or skin feeling, from release of active ingredients to stability or failure over time.
In particular, yield stress fluids (YSF) are materials which resist like solids when they are subjected to small stresses, while they flow like liquids when the stress exceeds a threshold value (the yield stress). The structural and dynamic precursors of this transition are widely debated, as well as its reversibility, its local scale counterparts and the role of microstructure.
YSF are typically based on space-spanning networks, such as gels of fibers or attractive colloidal particles, or on space-filling building blocks like microgels, i.e. micrometric, swollen cross-linked polymer particles. Better understanding the interplay of structure, microscale response and macroscopic behavior is of critical importance also for designing better and more sustainable materials.
Among the several questions currently investigated in the field, we focused on a few key questions regarding the connection between very different length scales:

- How do changes at the molecular level, like different degrees of solvation, determine the microscopic behavior of individual microgels and the mechanical response of packed microgels at the macro-scale level?
- How does yield stress, a quantity typically estimated through bulk measurements, propagate down to the micro-scale, namely determining the trapping or motion of solid inclusions?
- How do heterogeneities at the meso-scale affect the macroscopic response?

To address these issues, during my PhD research I mainly focused on Carbopol, a microgel model system for simple YSF, and investigated its yielding transition across different length scales and upon changing its swelling state, tuning pH or changing solvent, as summarized below and described throughout the chapters of the thesis.

Microgel rheology in aqueous and non-aqueous solvents

By tuning pH values, we studied how the degree of swelling of the microgels determines the effective volume fraction and yield stress of the samples. In aqueous systems, maximum swelling is found at neutral pH values, as widely reported in the literature. To explore the generality of such behaviour in other solvents, we conducted a systematic investigation of the dispersibility of Carbopol samples in a wide range of solvents with different molecular structure and polarity.
Overall, we find that, as expected, polar solvent are better solvents for microgel particles. Moreover, we also find that it is possible to tune pH values and swelling by addition of NaOH or other strong bases also in non-aqueous systems, and obtain homogeneous, transparent YSF in several of them. The maximum degree of swelling upon neutralization is readily identified as the maximum in the yield stress value at a certain mass concentration.
By means of full equilibration of the samples against pure solvent or a set osmotic pressure, we could reconstruct the full dependence of yield stress and linear viscoelastic moduli on concentration for different polar solvents. We find specific threshold concentrations and high concentration yield stress values for the various solvents, which can be correlated to the degree of swelling and aggregation within the system.

Trapping of solid inclusions in yield stress fluids

This study investigates the stable entrapment of particles in YSF, focusing on how the equilibrium between yield stress and gravitational stress is influenced by the size and density of the particles and the microstructure of the material. We determined the local microscopic yielding of materials and compared it with their bulk rheological features.
To explore conditions of stability and instability of glass microspheres in YSF, we can tune and enhance gravitational stresses via centrifugation, which allows to efficiently investigate a broad range of experimental parameters. We studied Carbopol samples at different concentrations and pH values, in both aqueous and non-aqueous solvents with varying polarity. We find that the number and size of non-sedimenting microparticles, along with their distribution within the vial, depend on the degree of swelling and on the solvent. However, for most of the samples the critical gravitational stress can be rescaled with the bulk yield stress of the matrix.
To access the transient dynamics of the samples under gravitational stress, we are developing a centrifuge equipped with optical access, to perform turbidity measurements online. We could reconstruct the profile of the tracers within the YSF sample in a semi-quantitative way, and monitor the approach to the steady state, identifying the threshold values for stability. A paper is currently in preparation.

Large field-of-view heterogeneity maps

The bulk rheology of microgel suspensions and other soft materials can be severely affected by the size and degree of clustering of the building blocks, which on turn can depend on preparation protocols.
Here a simple and efficient approach is introduced to evaluate the sample structural heterogeneity up to the millimeter scales, inaccessible to typical microrheology approaches. The technique is based on low magnification microscopy of semi-dilute microgel suspensions subjected to capillary forces. The motion of a large number of dispersed tracers is

tracked and the scaling of their mean square displacement with time enables the classification of the prevailing regime of motion, from arrested to diffusive to flowing, in each sample region.
We applied this method to various microgel suspensions and quantified the degree of heterogeneity of samples undergoing different preparation protocols at lab and plant scales. The analysis captures different degrees of sample inhomogeneities and cluster size distributions in the samples, which result from the overall applied shear, in turn impacting the viscosity of the sample. A paper is currently in preparation.

Motion of yield stress fluid droplets on lubricated surfaces

Droplets of YSF hardly move on solid surfaces, even on dry superhydrophobic ones, due to their high effective viscosity, while highly slippery lubricated surfaces disclose the full investigation of their dynamic wetting.
The spreading and motion of millimeter-sized droplets of aqueous Carbopol samples were studied on lubricant-infused surfaces. Dynamical phase diagrams were established by varying the concentration of the dispersions and the inclination angle of the surfaces. Carbopol droplets can move even at very low inclination angles, with a velocity determined by the shear flow of the oil film that covers the solid substrate. However, as the speed of the droplets increased, they transitioned from sliding to rolling motion, with rolling becoming more pronounced at higher inclination angles and lower solution concentrations.
A simple criterion based on the ratio between the yield stress of the Carbopol suspensions and the gravitational stress acting on the YSF droplets was found to identify the transition between the two regimes: while a solid-like droplet can only slide, a partially fluidized one can deform and roll down.
These findings may have implications for the control of the motion of YSF droplets in microfluidic devices and in the investigation of the dynamics of soft and biological fluids. This research, performed in collaboration with the Lab of Physics of Surfaces and Interfaces at Università di Padova, has been published as:
Mattia Carneri, Davide Ferraro, Afshin Azarpour, Alessio Meggiolaro, Sebastian Cremaschini, Daniele Filippi, Matteo Pierno, Giuliano Zanchetta, Giampaolo Mistura "Sliding and rolling of yield stress fluid droplets on highly slippery lubricated surfaces" Journal of Colloid and Interface Science 644, 487 (2023)
(Link)

Complementary research activity: Rheo-microscopy on viscoelastic surfact solutions

Wormlike micellar (WLM) solutions are widely studied for their peculiar viscoelastic properties, also relevant for their applications. In particular, the well known surfactant cetylpyridinium chloride, when mixed with diclofenac sodium, can form micrometer long micelles displaying interesting nonlinear rheology.
In parallel to bulk rheology, I have conducted rheo-microscopy measurements on a linear, strain-controlled shear cell coupled with a microscope, to reconstruct the flow profiles across the gap for start-up experiments at different shear rates. At low rates, the measured stress response is monotonically increasing, up to a steady state value, and the resulting velocity profile is stable. At high enough shear rates, pronounced strain hardening emerges, with a stress peak, accompanied by the onset of shear banding and

elastic instabilities.
A paper regarding this study, performed in collaboration with the Rheology lab at the Università di Napoli "Federico II" has been submitted to Journal of Colloid and Interface Science. The outcomes of this research contribute to a deeper understanding of the behavior of surfactant solutions in pharmaceutical applications and other fields, highlighting the significance of shear-induced changes in microstructure.

CHAPTER 1

General introduction to materials and methods

1.1 Probing the mechanical response of materials

Rheology, the study of material flow and deformation [1], is crucial for understanding the behavior of diverse materials ranging from liquids to solids. Its foundation lies in the idealized models of elasticity and viscosity. Hooke's law describes ideal elastic solids, where extension is directly proportional to the applied force, and complete recovery occurs upon force removal. Conversely, Newton's law defines ideal fluids as exhibiting irreversible flow under shear, with a shear rate directly proportional to the applied force. However, many materials don't neatly fit these ideal classifications; instead, they display a combination of elastic and viscous properties, i.e. viscoelasticity. This arises from microscopic structural rearrangements under deformation, making the material response highly dependent on the timescale and amplitude of applied stress [1,2]. Therefore, a comprehensive rheological experiment aims to fully characterize a material's mechanical properties across a broad spectrum of timescales and deformation magnitudes, linking these properties to the material's internal structure [3].

This chapter introduces the fundamental principles of rheology as a concise overview of key concepts and material functions used in subsequent analyses. In particular, yield stress fluids are described, together with the main approaches to their characterization. Moreover, microgel suspensions are introduced as benchmark yield stress fluids which have been thoroughly used in this thesis. In particular, Carbopol microgels, their properties, and preparation protocol are described.

1.1.1 Shear deformations

Complex fluids are often classified according to their stress response to externally induced deformation. The response governed by their microstructure establishes a direct connection between this microstructure and macroscopic flow behavior. This is often obtained by imposing well-defined flow fields to the material. One of the main types of flows used to describe complex fluids is shear flow, characterized by tangential deformation, to each fluid element, for example, with a parallel-plate geometry (Fig. 1.1).
For a fluid confined between parallel plates separated by a distance dy, with the upper plate moving with velocity v_x in the x direction, the shear strain γ 1.2 and shear stress (1.1) are defined as:

$$\sigma = \frac{F}{A} \tag{1.1}$$

$$\gamma = \frac{ds}{dy} \tag{1.2}$$

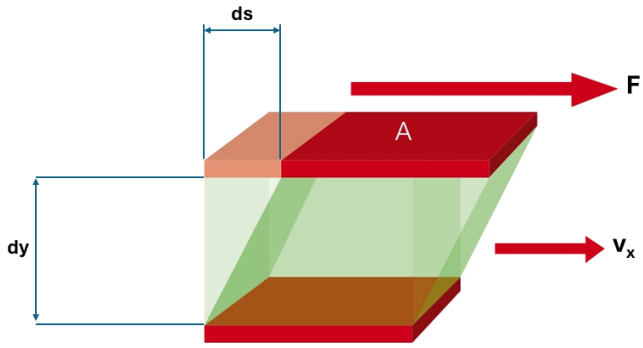

Figure 1.1: The sample is confined between two parallel surfaces, separated by a distance dy and cross-sectional surface area A. A deformation ds, corresponding to a shear strain $\gamma = \frac{ds}{dy}$ is applied to the sample by moving the top plate, and the force F exerted back from the material is measured, from which it is possible to obtain the shear strain (γ) and the shear stress ($\sigma = F/A$).

where ds is the infinitesimal displacement of a fluid element in time dt. The shear rate $\dot{\gamma}$ 1.3 is then:

$$\dot{\gamma} = \frac{d\gamma}{dt} = \frac{1}{dt}\frac{ds}{dy} = \frac{dv_x}{dy} \tag{1.3}$$

Rheological measurements, frequently performed with rotational shear rheometers, are crucial for characterizing this behavior. These rheometers control torque and measure angular displacement (or vice versa), depending on sample properties and geometry.
Measurements can be either strain-controlled (applying a defined strain and measuring the resulting stress) or stress-controlled (applying a defined stress and measuring the resulting strain). The relationship between shear stress σ (N m^{-2}), shear strain, and shear rate constitutes the fluid's constitutive equation, which varies significantly depending on the fluid's properties.

1.1.2 Viscoelasticity

Understanding the behavior of complex soft materials can be achieved by studying simpler, ideal materials. We can model these materials using springs (for elastic behavior) and dashpots (for viscous behavior), as shown in Fig. 1.2. This Figure illustrates two common rheological tests: creep and recovery (applying constant stress, then removing it), and stress relaxation (applying a sudden strain and observing the stress response).

Ideal elastic solids respond instantly to a step-stress with a constant strain proportional to stress (Figure 1.2 a1):

$$\sigma(t) = G_0\gamma(t) \tag{1.4}$$

where G_0 is defined as the elastic modulus (Pa). The stored energy is fully recoverable upon removal of the deformation and the strain fully recovers. In contrast, ideal fluids exhibit a linearly increasing strain under constant shear stress, with strain rate proportional to stress 1.2 a2):

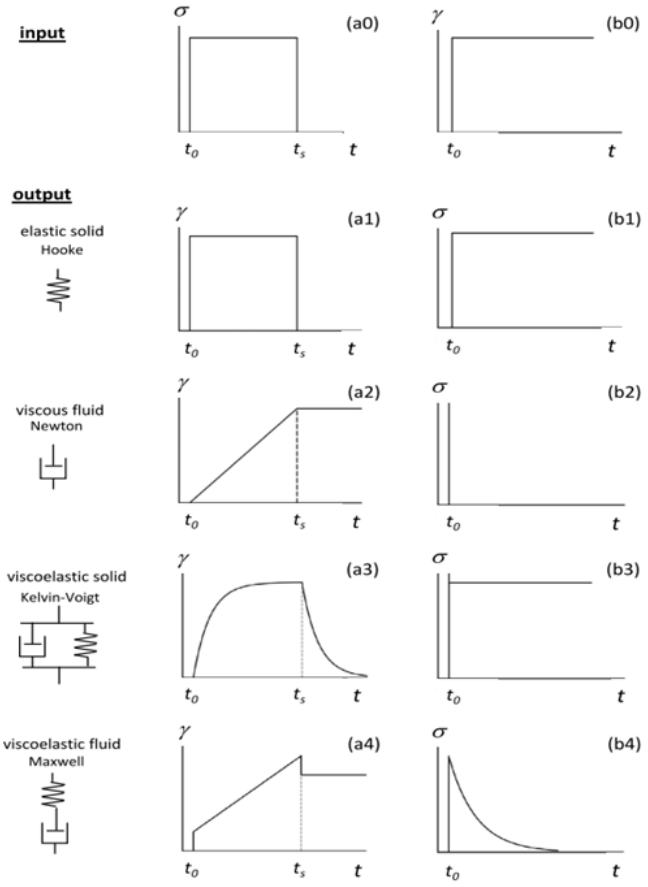

Figure 1.2: The left column depicts creep and recovery tests. (a0) shows a step stress applied at time t0 and released at time ts. Subsequent figures illustrate strain responses: (a1) ideal elastic solid; (a2) ideal viscous fluid; (a3) ideal viscoelastic solid; (a4) ideal viscoelastic fluid. The right column shows stress relaxation tests. (b0) illustrates a step strain applied at time t0. Subsequent figures show stress responses: (b1) ideal elastic solid; (b2) ideal viscous fluid; (b3) ideal viscoelastic solid; (b4) ideal viscoelastic fluid.[4]

$$\sigma(t) = \eta\dot{\gamma}(t) \tag{1.5}$$

where η is the dynamic shear viscosity (Pa·s). Here, energy dissipation is irreversible and the cumulated strain is retained upon stress removal.

Viscoelastic materials show a more complex behavior, which in some cases can be described as a combination of elastic and viscous elements. The Kelvin-Voigt model (spring and dashpot in parallel) represents a viscoelastic solid, like, e.g., a colloidal gel, an elastic matrix embedded in a viscous background. Its response to a step-stress is not instantaneous; strain increases slowly to a constant value, and recovery is also gradual. This is illustrated in Fig. 1.2 a3.

The Maxwell model (spring and dashpot in series) describes a viscoelastic fluid, like e.g. entangled polymers, whose response can be mainly elastic or mainly viscous de-

pending on the timescale of perturbation. Here, a step-stress causes an instantaneous strain followed by a linearly increasing strain due to the dashpot's viscous contribution. Strain recovery is incomplete (see Fig. 1.2 a4).

The responses of Hookean solids and Newtonian fluids to step-strain are shown in Fig. 1.2 b1 and b2, respectively: for ideal materials, a step-strain causes an instantaneous, constant stress in a solid and an instantaneous, short-lived stress peak in a fluid. The responses of Kelvin-Voigt and Maxwell elements are shown in Fig. 1.2 b3 and b4, respectively. In a Kelvin-Voigt material, the initial stress relaxes to a constant value. For a Maxwell fluid, a step-strain results in initial solid-like behavior followed by exponential stress relaxation[5,6]. For small applied stress values, which do not trigger additional structural changes, the stress-strain relationship can be expected to be linear. Material response is thus better described in terms of compliance (strain over applied stress, $J(t)$) or shear modulus (stress over applied strain, $G(t)$), allowing data from different stress levels to be combined into a single curve.

1.1.3 Oscillatory rheology

Since many materials exhibit a complex, time-dependent mix of elastic and viscous properties, a complete rheological investigation requires characterizing mechanical properties across a wide range of timescales and deformation amplitudes, ultimately connecting these macroscopic properties to the underlying microscopic structure.

Oscillatory shear rheometry, a technique pioneered by Andrew Gemant in 1935, offers a particularly powerful approach to investigate viscoelasticity[7]. This method simultaneously probes both the solid-like (elastic) (Fig. 1.3 a) and liquid-like (viscous) (Fig. 1.3 b) aspects of material behavior. Unlike steady-state shear measurements, oscillatory shear independently controls both the amplitude and frequency (representing the timescale) of the applied strain or stress, providing access to a broader spectrum of material properties. Critically, it enables the study of transient and nonlinear responses under steady-state conditions. The material response within each cycle can reach equilibrium, even during repeated loading and unloading cycles. This capability has established oscillatory shear as a widely used technique for the simultaneous characterization of microscopic dynamics[8–12]. Despite its advantages, interpreting the data obtained from oscillatory rheological experiments can be complex. The cyclical nature of the applied deformation — with its repetitive acceleration and deceleration phases — makes the direct link between the macroscopic response and microscopic dynamics challenging.

At a microscopic level, the deformation within a sheared material can be decomposed into two components: affine and non-affine. Affine deformation directly mirrors the macroscopic, externally imposed deformation. Non-affine deformation, however, arises from heterogeneities in the local elastic response or from plastic rearrangements within the material[13]. In the following, we assume only affine deformations. Although steady-state material behavior is independent of the control method, we will use the standard strain-controlled approach for oscillatory rheology[5,14,15].

Under small perturbations, following the Boltzmann superposition principle[16], a linear viscoelastic (LVE) response can be expressed in general as the sum of the infinitesimal, linear stress responses to strain deformations:

$$\sigma(t) = \int_{-\infty}^{t} G(t-t')\dot{\gamma}(t')dt' \tag{1.6}$$

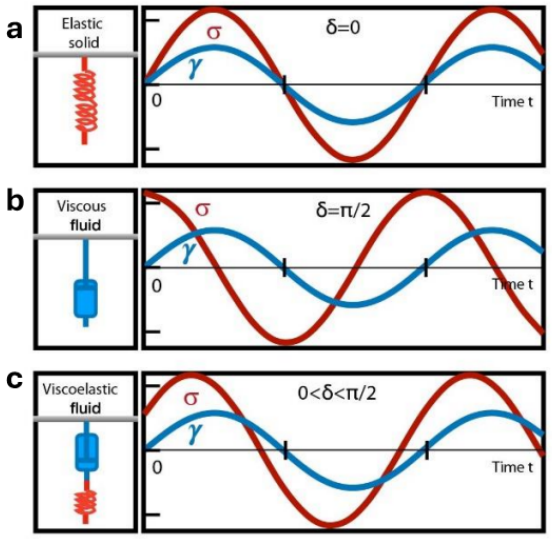

Figure 1.3: Oscillatory shear experiments: Schematic diagrams of shear strain γ (blue curve) with the resulting shear stress response σ (red curve). (a) For a phase angle of $\delta = 0$, the sample behaves as an elastic solid. (b) For a phase angle of $\delta = \frac{\pi}{2}$, the sample behaves as a viscous fluid. (c) viscoelastic fluid shows a phase angle between 0 and $\delta = \frac{\pi}{2}$.

where $G(t)$ is the stress relaxation modulus. In Fourier space, this simplifies to:

$$\hat{\sigma}(\omega) = \hat{G}(\omega)\hat{\dot{\gamma}}(\omega) = \hat{G}^*(\omega)\hat{\gamma}(\omega) \tag{1.7}$$

where the hat denotes the Fourier transform and $\hat{G}^*(\omega)$ is the complex modulus ($\hat{G}^*(\omega) = i\omega\hat{G}(\omega)$). Applying an oscillatory strain $\gamma(t) = \gamma_0 \sin(\omega t)$ allows experimental probing of the LVE regime. This yields:

$$\sigma(t) = \gamma_0[G' \sin(\omega t) + G'' \omega \cos(\omega t)] \tag{1.8}$$

The storage modulus, $G' = \Re(\hat{G}^*)$, and loss modulus, $G'' = \Im(\hat{G}^*)$, represent the in-phase and out-of-phase components of the complex shear modulus $\hat{G}^*$. $G'(\omega)$ relates to the energy stored per unit volume, while $G''(\omega)$ is proportional to the energy dissipation rate[17] (see Fig. 1.3 c for the viscoelastic fluid response).
Equation 1.8 can be rewritten as:

$$\sigma(t) = G'\gamma(t) + G''(\dot{\gamma}(t)/\omega) \tag{1.9}$$

For an ideal solid, $\hat{G}^* = G' = G_0$ and for a Newtonian fluid, $\hat{G}^* = iG'' = i\omega\eta$. G' and G'' thus relate to the stored and dissipated energy (W_{stored} and $\dot{W}_{diss}$) per unit volume per cycle[18,19]:

$$G'(\omega) = \frac{4\langle W_{stored}(\omega)\rangle}{\gamma_0^2} = \frac{2\langle \sigma(t)\gamma(t)\rangle}{\gamma_0^2} \tag{1.10}$$

$$G''(\omega) = \frac{2\langle \dot{W}_{diss}(\omega)\rangle}{\omega\gamma_0^2} = \frac{2\langle \sigma(t)\dot{\gamma}(t)\rangle}{\omega\gamma_0^2} \tag{1.11}$$

where the average is calculated throughout the oscillation period. The frequency dependence of these moduli fully characterizes the LVE response. Frequency sweep experiments can fully characterize the LVE response of materials across a broad range of timescales[5,20]. These experiments involve applying a sinusoidal strain of fixed magnitude (γ_0) to a material and measuring the resulting storage (G') and loss (G'') moduli as a function of oscillation frequency (ω)[21,22]. The ratio G''/G' ($\tan\delta$) can indicate whether elastic or viscous behavior dominates at a given frequency[21,23]. Substituting a sinusoidal strain into Equation 1.8 (and removing time dependence) gives:

$$\sigma^2 - 2G'\sigma\gamma + \gamma^2(G'^2 + G''^2) = (G''\gamma_0)^2 \tag{1.12}$$

A similar equation can be derived using the strain rate:

$$\omega^2\sigma^2 - 2G''\sigma\omega\dot{\gamma} + \dot{\gamma}^2(G'^2 + G''^2) = (G'\dot{\gamma}_0)^2 \tag{1.13}$$

These parametric equations represent ellipses in the stress-strain and stress-strain rate planes, known as Lissajous-Bowditch figures (Fig. 1.4). In the stress-strain representation, the response of an ideal viscous fluid appears as a perfect circle, while an ideal elastic solid shows a diagonal line. Correspondingly, the area enclosed by these curves relates to the dissipated and stored energy[24]:

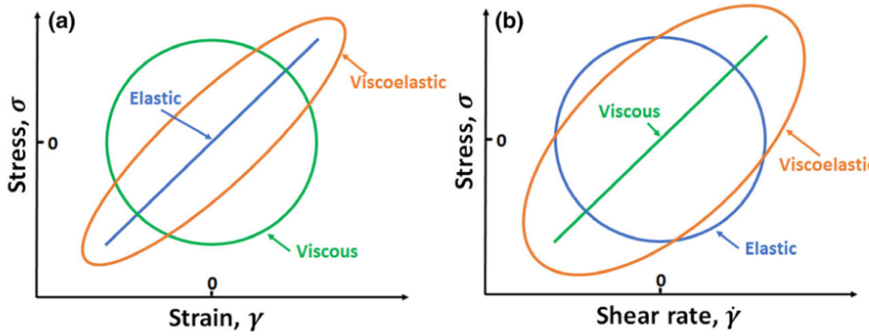

Figure 1.4: Lissajous plots for ideal materials where (a) stress versus strain or (b) stress versus shear (strain) rate can be plotted with LAOS data.[24]

$$W_{diss}(\omega) = \int_0^T \sigma(t)\dot{\gamma}(t)dt = \int \sigma(\gamma)d\gamma \tag{1.14}$$

$$W_{stored}(\omega) = \frac{1}{\omega}\int \sigma(\dot{\gamma})d\dot{\gamma} \tag{1.15}$$

These integrals are directly related to G'' (Equation 1.11) and G' (Equation 1.10).

Idealized viscoelastic models, such as the Kelvin-Voigt (solid-like) and Maxwell (fluid-like) models (Fig. 1.5 a,b), illustrate distinct frequency dependencies. The Kelvin-Voigt model displays a frequency-independent G' and a linearly increasing G'', with G' dominating at low frequencies and remaining finite at $\omega = 0$, characteristic of a solid. In contrast, the Maxwell model shows G' dominance only at high frequencies, while G'' dominates at low frequencies and increases linearly, typical of a fluid.

However, real materials rarely exhibit such idealized behavior. For instance, dense emulsions[25] (often classified as soft glassy materials, Fig. 1.5 c) typically demonstrate an almost frequency-independent G', but a non-linear G'' with a shallow minimum, indicating additional low-frequency dissipation mechanisms. Similarly, worm-like micellar systems[22,26] (viscoelastic fluids; Fig. 1.5 d) only display Maxwell fluid behavior at low frequencies; at higher frequencies, G'' increases due to segmental fluctuations within the micelles. Therefore, accurately predicting and interpreting frequency-dependent responses necessitates considering all relevant dynamic contributions within the system. Frequency sweep tests are thus a crucial tool, not only for fundamental understanding but also for applications such as modeling and process optimization of complex materials[21,22].

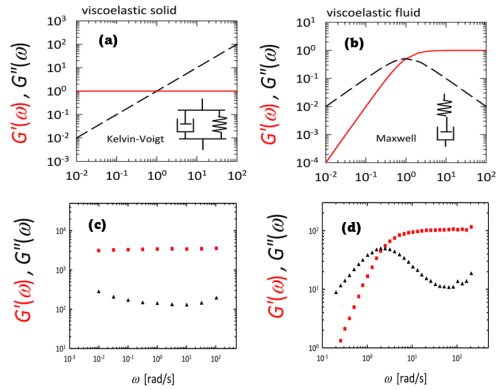

Figure 1.5: Frequency dependence of G' (red continuous line) and G'' (black dashed line) for (a) an ideal viscoelastic solid and (b) an ideal viscoelastic fluid, adapted from Roberto (2023)[6]. The plots illustrate the frequency dependence of G' (red squares) and G'' (black triangles) within the linear viscoelastic regime for (c) a dense emulsion and (d) entangled wormlike micelles, as described by Gurnon[27] (2014)

1.1.4 Nonlinear regime

Equation 1.7 states that in the linear viscoelastic (LVE) regime, a sinusoidal deformation produces a perfectly sinusoidal stress response directly proportional to the applied strain amplitude. However, as the strain amplitude increases, the material response becomes nonlinear[20,28], resulting in distorted stress profiles, higher harmonics, and dynamic moduli that depend on the deformation amplitude. In this nonlinear regime, Equation 1.7 is no longer strictly valid.

Nonlinear oscillatory tests, specifically strain sweeps (amplitude sweeps), are powerful tools for characterizing the nonlinear rheological behavior and yielding mechanisms of soft materials[19]. These tests involve applying an oscillatory strain with a constant frequency ($\omega = \omega_0$) and measuring the resulting storage (G') and loss (G'') moduli as a

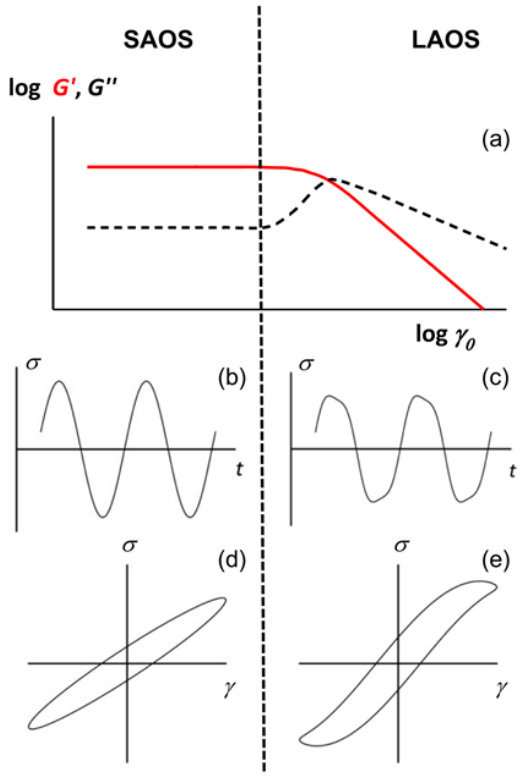

Figure 1.6: Strain sweep characterization of the viscoelastic response. (a) The transition from the linear viscoelastic (SAOS) to the non-linear viscoelastic (LAOS) regime is identified by a strain sweep performed at a fixed frequency. (b) In the SAOS regime, the storage (G') and loss (G'') moduli remain independent of strain amplitude, and the stress response is sinusoidal. (c) Conversely, the LAOS regime exhibits strain-amplitude-dependent moduli and a distorted stress response. This transition is further illustrated by the Lissajous plots: (d) an ellipse in the SAOS regime, and (e) a distorted ellipse in the LAOS regime.[6]

function of the applied strain amplitude. This allows for a detailed investigation of the material's response across different strain regimes.

A typical result of a strain sweep is schematically shown in (Figure 1.6 a). At low strain amplitudes, falling within the linear viscoelastic region (SAOS, small amplitude oscillatory shear), the material exhibits linear behavior. Both G' and G'' are independent of the strain amplitude, and the stress response remains sinusoidal, as depicted in (Figure 1.6 b). In this regime, the oscillatory shear measurements effectively probe the material's inherent microstructure and intermolecular interactions without significantly perturbing its equilibrium structure (the Lissajous curve is an ellipse).

However, upon increasing the strain amplitude beyond the linear viscoelastic limit, the material enters the large amplitude oscillatory shear (LAOS) regime. Here, both G' and G'' become strongly dependent on the strain amplitude. Accordingly, the stress response deviates significantly from a sinusoidal waveform (Figure 1.6c), exhibiting higher

harmonic contributions and leading to distorted Lissajous curves. Despite the mechanical moduli being poorly defined, the first harmonic components of the stress response are often used as estimates for energy storage and dissipation to define the viscoelastic characteristics of the system.[20].

Many soft matter systems in their arrested states, including dense emulsions, microgels, foams, colloidal glasses, and self-assembled polymer gels, exhibit a so-called type-III behavior[20], as illustrated in (Figure 1.6 a). This is defined by an overshoot in the loss modulus (G''), exceeding the storage modulus (G') above a certain strain value. Beyond this point, both moduli decrease with increasing strain amplitude, albeit at different rates, leading to an increase in the G''/G' ratio. These characteristics are often associated with the onset of yielding and plastic deformation[6,19]. Several models have been proposed to explain the type-III behavior, considering factors such as strain-induced microstructural changes, alterations in interparticle interactions, and forced relaxation processes[6,20]. Figure 1.7 compares the responses of two systems – a polysaccharide gel (panel a) and a dense micellar packing (panel b) – that exhibit quite similar type-III behavior in their first harmonic responses.

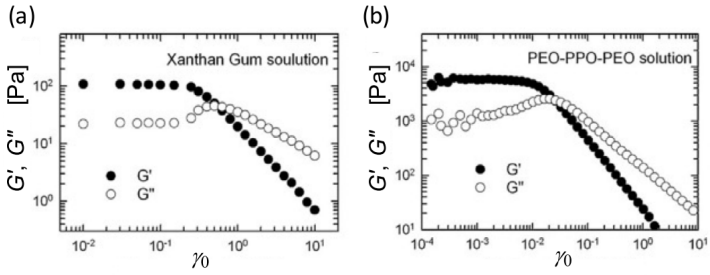

Figure 1.7: Strain dependence of (G') and (G'') (a) a polysaccharide gel formed from 4 wt% Xanthan gum in water and (b) a dense packing of micelles formed from 20 wt% PEO-PPO-PEO triblock copolymers in water[20]

The Xanthan gel (Figure 1.7 a) displays a steeper overshoot of G'', associated to a brittle yielding mechanism. In contrast, the micellar system (Figure 1.7 b) exhibits a smoother, more gradual growth, indicative of ductile yielding[29]. Overall, the robust observation of type-III behavior across diverse materials suggests that the first harmonic response is relatively insensitive to the specifics of the yielding mechanism. These finer details of the yielding process are likely encoded in the higher harmonic components of the stress response, appearing in the features of Lissajous curves[19].

1.2 Yield stress fluids

Yield stress fluids (YSF) are among the most widely used rheologically complex soft materials[30]. These materials exhibit a fascinating duality: they reversibly transition between solid-like and fluid-like behavior. At low stresses, they behave as solids, resisting deformation and maintaining shape; however, they flow like liquids when the applied stress surpasses a critical threshold – the yield stress[31,32]. This yielding transition is a defining characteristic with implications across diverse industries, including

food, cosmetics, pharmaceuticals, and manufacturing. Everyday examples range from mayonnaise and toothpaste to paints, foams, and wet cement[31,32]. Applications also include drug delivery, batteries, surface coatings, 3D printing and biomaterials (see Fig. 1.8).

The term 'yield stress' finds its roots in British Standard 5168 (1875), defined as 'that stress below which the substance is an elastic solid and above it a liquid'[33]. For decades, a central question in the field of YSF was whether the yield stress is a genuine physical phenomenon or merely an artifact, corresponding to a very high, yet finite, viscosity[33–35]. Although the robustness of the phenomenon is now well established, possible issues can arise on how to accurately determine the threshold value and on how to model the behavior of YSF across transition. Over the past 80 years, various, albeit not entirely equivalent, terms have been used to describe YSF in the literature. Rheologists have described them as viscoplastic, equivalent to Herschel-Bulkley fluids[32,36], elasto-viscoplastic[37], or thixotropic (time-dependent) viscoplastic[38]. Physicists, on the other hand, often classify them within the broader category of 'soft matter', encompassing soft solid particles, soft glassy materials, soft colloids/jammed systems, and soft particle suspensions/pastes/glasses. Chemical engineers and polymer chemists utilize a different set of descriptors, including polymer/colloidal gels/dispersions, and latex/carbomer dispersions/suspensions, or hydrogels.

As evidenced by the abundance of terminology, YSF behavior can be obtained using a wide array of chemistries and material structures. Fig. 1.9 illustrates various microstructures possibly giving rise to yield stress. Two main categories emerge: "glasses" (e.g., foams, microgel suspensions, emulsions, pastes, granular suspensions) characterized by crowded, repulsively interacting particles at high volume fractions, and "gels" (e.g., polymer networks, colloidal gels, capillary suspensions, magneto-rheological fluids) featuring attractive interactions and percolated networks even at low volume fractions. However, this distinction may become hazy when mixtures of repulsive and attractive interactions are available in the design space, as with 'attractive glasses' made of locally packed attractive colloidal particles.

The macroscopic behavior of YSF is a direct consequence of their disordered microstructure[47]. Unlike crystalline solids with their ordered atomic arrangements, these materials are amorphous, lacking long-range order. This amorphous nature complicates understanding the microscopic mechanisms underlying yielding. While plasticity in crystalline solids is well-understood in terms of dislocation motion[48], the lack of such defined structure in amorphous materials makes identification and analysis of structural fingerprints of yielding challenging. The concept of a unified 'jamming' phase diagram[49] suggests that temperature, applied stress, and packing fraction all influence the transition from a jammed (solid-like) to an unjammed (liquid-like) state. This framework has spurred research connecting macroscopic rheological properties with microscopic dynamics across various amorphous systems[50,51] and investigating the possibility of a unifying theoretical framework for the yield stress phenomenon[52].

However, the complexity is further amplified by the wide diversity of yield-stress materials, with particle sizes ranging from nanometers to millimeters[14,32]. This variation in length scales leads to distinct contributions of thermal fluctuations and differences in inter-particle interaction potentials[53]. For example, dry granular materials are dominated by friction, while surface tension plays a crucial role in foams and emulsions. Colloidal glasses are governed by entropic forces[54], whereas physical gels involve stronger attractive interactions. Understanding the yielding transition thus necessitates considering material-specific microscopic details alongside universal aspects of the transition.

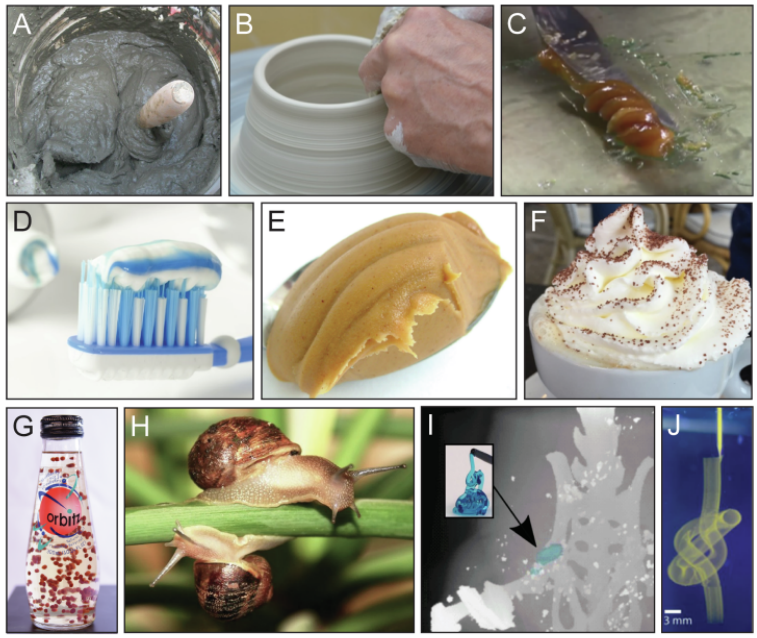

Figure 1.8: Diverse applications of yield-stress fluids. Examples include: (a) building mortar, (b) modeling clay, (c) Flemish paint medium, (d) toothpaste, (e) peanut butter, (f) whipped cream, (g) Orbitz beverage, (h) snail slime, (i) shear-thinning biomaterial (image adapted from [39]), and (j) 3D printing in a yield-stress fluid bath (image adapted from [40]). Images a, b, d, e, and f are in the public domain (CC0). Photographs courtesy A.Z.N. (g) and R.H.E. (h).[41]

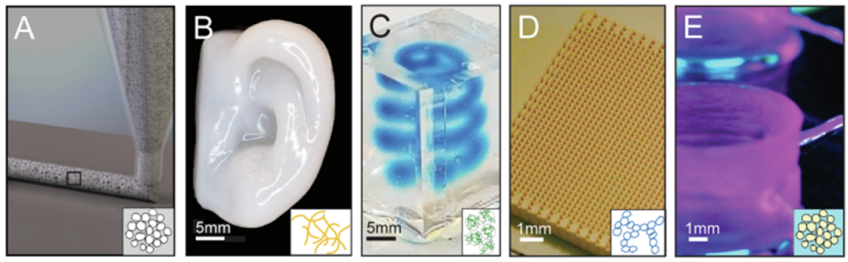

Figure 1.9: Diverse microstructural classes of yield-stress fluids for direct-write 3D printing. Despite belonging to distinct microstructural classes (inset schematics), these materials exhibit similar performance characteristics. Examples include: (a) foams for porous ceramics[42], (b) fibrillar networks for bioprinting[43], (c) crowded microgels within a supporting hydrogel[44], (d) colloidal particulate gel networks[45], and (e) crowded emulsions[46]. Image (b) adapted with permission from Markstedt et al.[43].

1.2.1 Measuring yield stress

The determination of yield stress (σ_y) in yield stress fluids remains a significant challenge despite their widespread use in various applications. While the fundamental concept — a critical stress marking the transition from elastic solid-like behavior to fluid-like flow — is simple, its consistent modeling is not straightforward; moreover, practical definition and measurement are inherently ambiguous and context-dependent. This ambiguity leads to substantial discrepancies in reported σ_y values, preventing the development of predictive models and robust engineering designs. The main rheological approaches to yield stress determination are stress- or strain rate-based and include:

Steady shear (flow curve): This established method consists in the application of a constant shear rate, in the range 10^{-3} to 10^{3} s^{-1}) and measuring the resulting steady-state shear stress; fitting the resulting flow curves (shear stress versus shear rate) to a suitable model provides the yield stress as a parameter (see below for a more systematic description).

Oscillatory shear: This method employs oscillatory strain or stress sweeps at a fixed frequency to measure the storage (G') and loss (G'') moduli. Several criteria exist for identifying the yield point from oscillatory data, each with limitations as highlighted by Dinkgreve et al.[55].

- **Characteristic modulus ($G' = G''$):** This method identifies the yield point as the intersection of G' and G''. Dinkgreve et al. found this criterion consistently yielded the highest σ_y and yield strain (γ_y) values, likely because viscous dissipation is already substantial at this point[55]. This approach can overestimate σ_y due to the onset of yielding occurring before the modulus crossover (Fig. 1.10 a).
- **Power-law fitting:** Fitting power-law functions to G' data well above and below the yield point, and determining their intersection, provides another yield point estimate[56,57]. The sensitivity of this method to the chosen fitting range requires careful consideration (Fig. 1.10 b).
- **Log-log plot intersection:** Analyzing a log-log plot of the total stress versus strain from oscillatory data, and identifying the intersection of low-strain linear and high-strain power-law regions[58–61], often produces values closer to steady shear results (Fig. 1.10 c).

Startup: This transient technique involves imposing a constant shear rate and measuring the stress evolution as a function of time/strain (see Figure 1.11). The yield stress can be defined from the departure from linearity, the stress overshoot (if present), or the attainment of steady-state stress[62,63], each leading to different values. The influence of the imposed shear rate and time resolution, along with the ambiguity in identifying the elastic limit prior to yielding, requires a wide range of shear rates. The sensitivity to the presence or absence of a stress overshoot, as observed in Carbopol microgel samples[55], also needs to be considered.

Creep compliance: Creep experiments, involving the application of constant stress and monitoring the resulting strain over time (see Figure 1.12), infer the yield stress from the transition between elastic deformation (constant strain plateau) and viscous flow (strain linearly increasing with time)[59], through a region with sub-linear growth. The inherent challenges of creep experiments — requiring an a priori estimate of yield stress

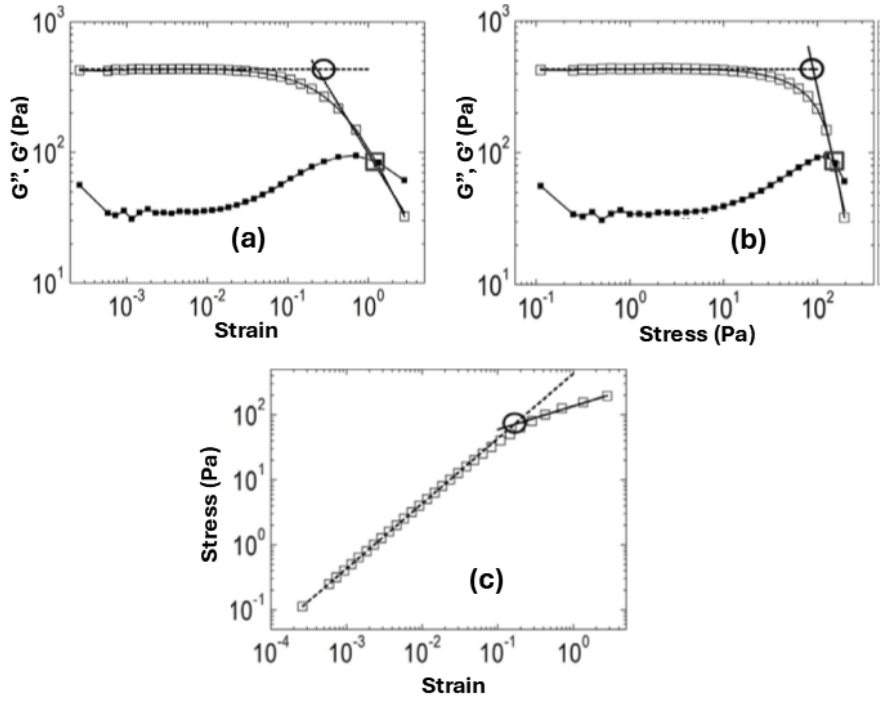

Figure 1.10: Rheological characterization of Carbopol Ultrez U10 samples. (a) Storage (G') and loss (G'') moduli as functions of strain (γ). Open symbols represent G', and filled symbols represent G''. The black line shows the power-law fit above the yield point, and black circles indicate where this line intersects the horizontal line marking the linear viscoelastic G' region. A black square highlights the characteristic modulus at which $G' = G''$. (b) G' and G'' as functions of stress (σ). Solid lines denote power-law fits above and below the yield point; their intersection is indicated by a black circle, and a black square again denotes the characteristic modulus where $G' = G''$. (c) Stress (σ) versus strain (γ) from the same oscillatory measurements in (a) and (b). The lines are power-law fits capturing the behavior well above and well below the yield point, with black circles marking their intersection[55].

and being sensitive to structural changes during long measurement times — require reassessment with systematic variations in applied stress and measurement duration.

Existing research highlights the significant variability in yield stress measurements obtained using different rheological techniques[55,66–68]. These studies reveal variations exceeding an order of magnitude, even for seemingly simple, non-thixotropic materials (although in many cases, yield stress parameters determined using different methods exhibit similar scaling with, e.g., concentration). This discrepancy arises not only from the choice of the rheological method but also from the complexities of data analysis and the influence of material-specific properties. A comprehensive and systematic comparison of multiple experimental techniques and data analysis approaches is crucial to obtain consistent estimates.

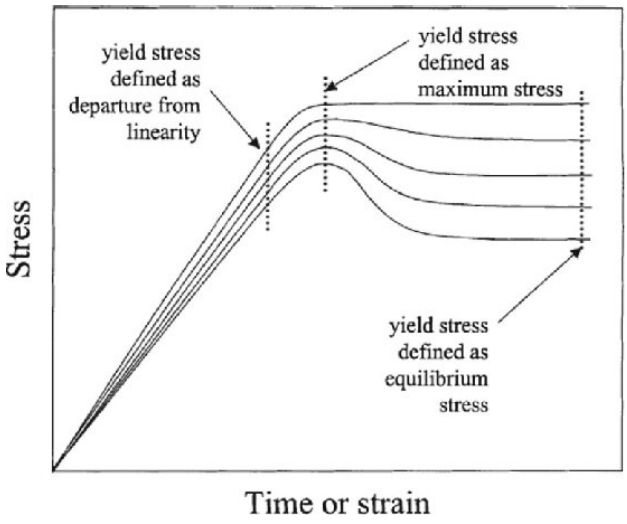

Figure 1.11: Sketch of the stress response in a startup experiment at a constant shear rate, with various associated definitions for the yield stress[64].

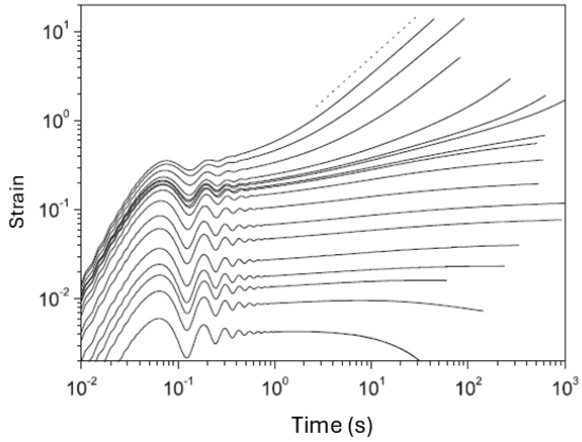

Figure 1.12: Typical deformation vs time for different stress values applied to a hair gel, from 0.8 (bottom curve) to 100 Pa (top curve). The dotted line is the curve of slope 1, corresponding to viscous flow[65].

1.2.2 Modelling of flow curves

Given the transition from solid-like to fluid-like behavior, a convenient and widely used approach to determine the yield stress is based on measuring the strain rate-dependent stress, creating a flow curve. Although practically useful, the precise yield stress (defined at zero shear rate) is impossible to measure directly. Instead, σ_y represents the stress threshold required to initiate viscous deformation by breaking down the material's internal structure. Below this threshold, the material behaves elastically with effectively

infinite viscosity. The simplest flow curve model for YSF is the Bingham model[69]:

$$\sigma = \sigma_y + \eta_{bg}\dot{\gamma} \tag{1.16}$$

where η_{bg} is a viscosity linked to the continuous phase viscosity. The Bingham model contains both elastic and viscous dissipation processes. Elastic dissipation is strain-dependent (stress is strain-rate independent), while viscous dissipation exhibits a linear, Newtonian stress-strain rate connection. At low shear rates, elastic dissipation is dominant, but viscous dissipation is dominant at high shear rates.

However, for systems like concentrated colloids and soft glassy materials, plastic rearrangements must be considered. The Hebraud-Lequeux model[70] incorporates local rearrangements triggered when local stress exceeds yield stress, leading to stress redistribution and further rearrangements, creating a strain rate-dependent plastic dissipation. Bocquet et al.[71] extended this to a kinetic elastoplastic model:

$$\sigma = \sigma_y + A\dot{\gamma}^{1/2} \tag{1.17}$$

where $A = \sigma_y\sqrt{t_k}$ and t_k is a stress relaxation time[72]. This model predicts a square root dependence of stress on strain rate at high strain rates, also predicted in models considering viscous friction[73] or interparticle lubrication forces[74]. Equation 1.17 describes rather well many soft glassy materials[74,75].

However, many YSF exhibit shear-thinning behavior that deviates from both linear and square root dependencies, often following an intermediate power law[76–78]. Such discrepancy is so common that has led to the widespread use of the empirical Herschel-Bulkley (HB) model to describe their flow curves[79–82]:

$$\sigma = \sigma_y + K\dot{\gamma}^n \tag{1.18}$$

where K is the so-called consistency coefficient and n is the flow behavior index. Although K and n lack clear physical interpretations and deviations are often observed, the HB model remains widely used to describe viscoplastic fluids such as emulsions, suspensions, polymeric gels, foodstuffs, and pastes[32].

The HB model exponent n often exhibits a strong and systematic dependence on the continuous phase viscosity (decreasing n with decreasing viscosity), indicating that this parameter is not solely a material property but is also influenced by experimental conditions[83]. This highlights a limitation of purely empirical models. For this reason, a three-component (TC) mechanistic model was developed by Caggioni et al. to describe the flow behavior of YSF[83]. This model incorporates elastic, plastic, and viscous stress contributions, integrating aspects of Bingham and kinetic elastoplastic models:

$$\sigma = \sigma_y + \sigma_y\left(\frac{\dot{\gamma}}{\dot{\gamma}_c}\right)^{1/2} + \eta_{bg}\dot{\gamma} \tag{1.19}$$

where $\dot{\gamma}_c$ is a critical shear rate, and η_{bg} is the background viscosity. This model accounts for deviations from purely plastic dissipation models observed at experimentally attainable shear rates where viscous dissipation becomes significant. The TC model proposes that the total stress is caused by the cumulative contributions of three separate processes, which correspond to the three components in Equation 1.19:

1. **Elastic dissipation:** Soft glassy materials exhibit elasticity; their structure deforms reversibly under stress. At low shear rates, stress primarily causes elastic deformation, proportional to strain but independent of strain rate. Upon stress removal, the material recovers its original shape, releasing stored elastic energy. The model provides this as a constant stress at low shear rates (Figure 1.13).

2. **Plastic dissipation:** Increasing shear rate leads to stress exceeding σ_y, causing irreversible structural rearrangements and dissipating energy[82]. The rate of energy dissipation is related to $\dot{\gamma}^{1/2}$, reflecting the non-linear stress-shear rate relationship characteristic of soft glassy materials beyond the yield point (Figure 1.13)[71,72,84].

3. **Viscous dissipation:** At high shear rates, the continuous phase viscosity (η_{bg}) dominates stress contribution, exhibiting Newtonian fluid behavior with linear increase (Figure 1.13[70]).

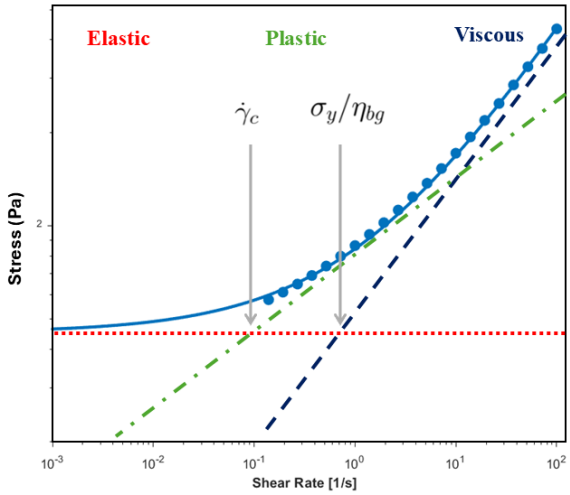

Figure 1.13: Schematic representation of the three-component (TC) model for the flow curve of a 5 wt% aqueous suspension of C971 NF (filled blue circle). The model decomposes the stress into three contributions: an elastic component (red dotted line), a plastic component scaling with $\dot{\gamma}^{1/2}$ (green dashed-dotted line), and a viscous component scaling linearly with $\dot{\gamma}$ (dark blue dashed line). The blue curve represents the total stress, the sum of these three components (the blue dots are experimental data). The intersection of the elastic and plastic components defines $\dot{\gamma}_c$, while the intersection of the elastic and viscous components defines σ_y/η_{bg}. The regions above the intersections are labeled to indicate dominance by elastic, plastic, and viscous dissipation, respectively.

The critical shear rate ($\dot{\gamma}_c$) is a key parameter, scaling the plastic contribution and reflecting the timescale of structural rearrangements. A larger γ_c indicates that a higher shear rate is required for significant plastic deformation.

The TC model provides a physically-based description of flow behavior, fitting experimental data (Figure 1.14) as well as the Herschel-Bulkley model but offering parameters (σ_y, γ_c, η_{bg}) with clear physical interpretation.

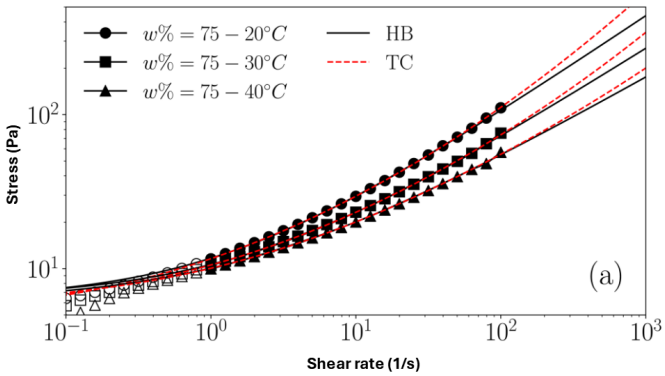

Figure 1.14: Flow curves for 75 wt% oil emulsions (6 Pa·s oil) measured at 20°C (circles), 30°C (squares), and 40°C (triangles). Solid black lines represent the best fits to the Herschel-Bulkley (HB) model; dashed red lines represent the best fits to the three-component (TC) model. The fitting range is restricted to shear rates ($\dot{\gamma}$) ≥ 1 s^{-1} to exclude data (open symbols) affected by slip.[83].

1.2.3 Rheology experiments

The rheological properties of all materials were characterized using an Anton Paar MCR302 stress-controlled rheometer (Fig. 1.15) equipped with a Peltier temperature control system and a 50 mm diameter cone-plate geometry (Fig. 1.16) (1° truncation angle). The experiments were conducted at a constant temperature of 22 °C. To minimize temperature gradients and solvent evaporation, an active temperature-controlled hood (achieving temperature gradients ≤ 0.1 °C) was employed.

Figure 1.15: Rheometer

A standardized pre-shear protocol was implemented prior to each series of rheolog-

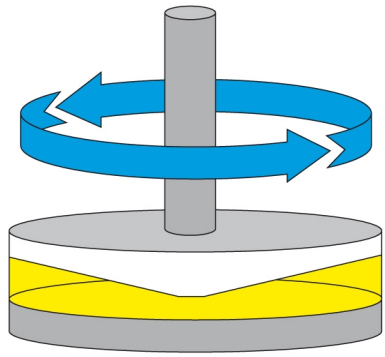

Figure 1.16: Cone

ical tests to ensure reproducibility and eliminate the influence of sample history. This involved a three-step preshear with the application of a constant shear rate of 100 s^{-1} for 120 s, followed by oscillations with a decreasing strain ramp from 500% to 0.1% at a constant angular frequency of 10 rad/s. A subsequent 120 s rest period allowed for complete stress relaxation before starting the test.

Subsequently, three distinct rheological tests were implemented in the experiment phase to comprehensively characterize the samples:

- **Frequency Sweep measurements:** These experiments investigated the linear viscoelastic response of the samples to oscillatory shear deformation. A constant strain amplitude of 0.1%, verified to remain within the linear viscoelastic region for all samples, was applied across a decreasing range of angular frequencies (ω) from 100 to 0.01 rad/s. The duration of each interval was set to ensure a steady-state response and a suitable number of cycles for each frequency. The resulting storage modulus (G'), representing the elastic component of the material response, and loss modulus (G''), representing the viscous component, were recorded and analyzed to determine characteristic relaxation times and identify any transitions in the microstructure.

- **Large Amplitude Oscillatory Shear (LAOS) measurements:** LAOS tests were conducted to probe the non-linear viscoelastic behavior of the fluids. These measurements were performed at a constant angular frequency of 1 rad/s, while systematically increasing the strain amplitude (γ) from 0.1% to 300%. This range encompassed both the linear viscoelastic regime and the non-linear regime, allowing for the identification of any yield stress or significant structural changes induced by large deformations. The resulting stress responses were analyzed to determine the extent of non-linearity and to extract parameters describing the material's behavior under large deformations.

- **Flow curves:** Steady shear experiments were conducted to determine the shear-thinning or shear-thickening behavior of the fluids. A constant shear rate sweep from 0.1 to 100 s^{-1} was applied, and the resulting shear stress (σ) was recorded once a steady state was reached at each shear rate ($\dot{\gamma}$). The resulting flow curves (shear stress (σ) versus shear rate ($\dot{\gamma}$)) were analyzed to determine the yield stresses. Data obtained at shear rates below 0.1 s^{-1} were excluded from the analysis due to the presence of wall slip (owing to the utilization of a non-roughened cone-plate

geometry). This slip, evidenced by deviations from expected flow behavior (e.g., non-monotonic shear stress increase with shear rate), was deemed to compromise the reliability of the low shear rate measurements.

1.3 Microgels

Microgels are crosslinked polymer networks that can expand in good solvent conditions[85–87] or, as defined by Rodriguez et al. (1994)[88], "aqueous dispersions of internally cross-linked, acid-containing lattices". Their attractiveness arises from the ability to control their swelling behavior in response to environmental stimuli, such as pH, ionic strength, or temperature. For example, pH-sensitive microgels can be made from poly-acids like poly(carboxylic acid) and poly(sulfonic acid), as well as poly-bases like poly(amine). However, the crosslinks restrict the maximum degree of swelling (Fig. 1.17). Microgel particle diameters typically range between a few nanometers to tens of micrometers[89–91].

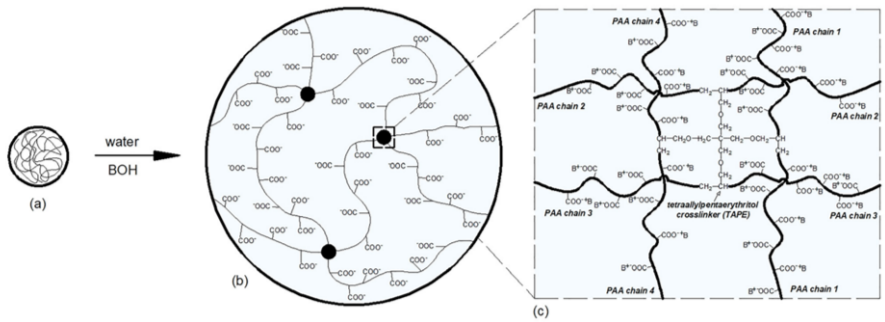

Figure 1.17: Schematic visualization of Carbopol particle. (a) in solid state with COOH groups, (b) after neutralization in an alkali aqueous solution with dissociated COO− groups where solid circles represent one particular crosslinked node shown in (c) in more detail[92]

Microgels form a suspension of soft elastic particles exhibiting rheological properties similar to both polymer gels (high elastic modulus) and particle suspensions (yield stress)[78,93]. Rheology is primarily tuned by the effective volume fraction ϕ_{eff} of the suspension, which develops yield stress when reaching random close packing. For microgels, the growth of σ_y typically exhibits two power-law regimes vs. concentration (C)[94], with very different exponents (Figure 1.18). Immediately above the threshold concentration, σ_y steeply increases with C, with a significant influence of inter-particle forces. For concentrations approaching $\phi_{eff} = 1$, the rate of increase of σ_y diminishes considerably. This shift indicates a change in the dominant yielding mechanism. At higher concentrations, yielding is likely governed by larger-scale microstructural rearrangements.

The rheology of microgel suspensions is tuned by several factors, including inter-particle interactions[32,95], particle size, and solvation[93]. Microgel softness and particle interactions are particularly important, both being influenced by the polymer network's chemistry, crosslinking density, and solvent quality. Crosslinking density significantly impacts a microgel's elastic modulus and softness. Highly crosslinked microgels are

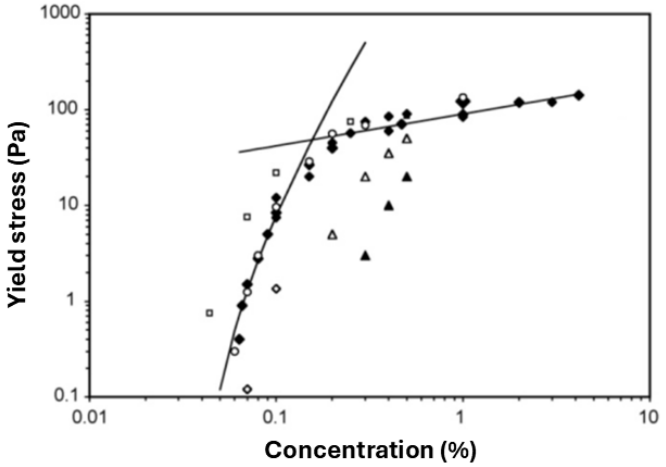

Figure 1.18: Yield stress as a function of weight concentration for neutralized Carbopol 940 dispersions. Lines represent different rheological regimes[94].

stiffer and behave similarly to hard-sphere colloids, while low crosslinking allows for increased chain mobility, resulting in behavior closer to core-shell particles with potential inter-penetration[95,96]. Intermediate crosslinking allows shape retention at low densities and deformation at high volume fractions. At high densities, where particle compression and deformation occur, lower crosslinking leads to greater deviations from hard-colloid behavior due to increased compressibility[97].

The effect of these parameters can be experimentally evaluated by examining the phase behavior (liquid-to-solid transition and threshold concentration) as the volume fraction increases. Figure 1.19 shows a rheological characterization of six Carbopol types at 0.1 wt%, 0.5 wt%, and 1.0 wt% (23°C), illustrating the influence of crosslinking density, interparticle interactions, and particle size on the liquid-to-solid transition and critical concentration. This analysis provides insights into the underlying mechanisms and aids in selecting appropriate Carbopol types for rheological modeling.

The figure is structured to provide a thorough understanding of Carbopol's rheological response across a broad range of conditions:

(a) Steady Shear Flow Measurements: This section (Figure 1.19a) illustrates the relationship between shear stress and shear rate, directly reflecting the fluid's viscosity. The plots clearly demonstrate the strong dependence of viscosity on both Carbopol type and concentration. At low concentrations (0.1 wt%), the differences between Carbopol types are minimal, with only slight shear-thinning, suggesting low viscosities. However, as concentration increases (0.5 wt% and 1.0 wt%), significant viscosity variations emerge among the different Carbopol types. Some display markedly higher viscosities and pronounced shear-thinning, highlighting the considerable influence of microgel composition on viscous properties. Higher concentrations exhibit more pronounced non-Newtonian behavior.

(b) Amplitude Sweep Tests: This section (Figure 1.19b) analyzes the viscoelastic properties (storage modulus, G', and loss modulus, G'') as a function of strain amplitude. This analysis is crucial for determining the linear viscoelastic region (LVR), the strain amplitude range where the material responds linearly and elastically. Across all Carbopol

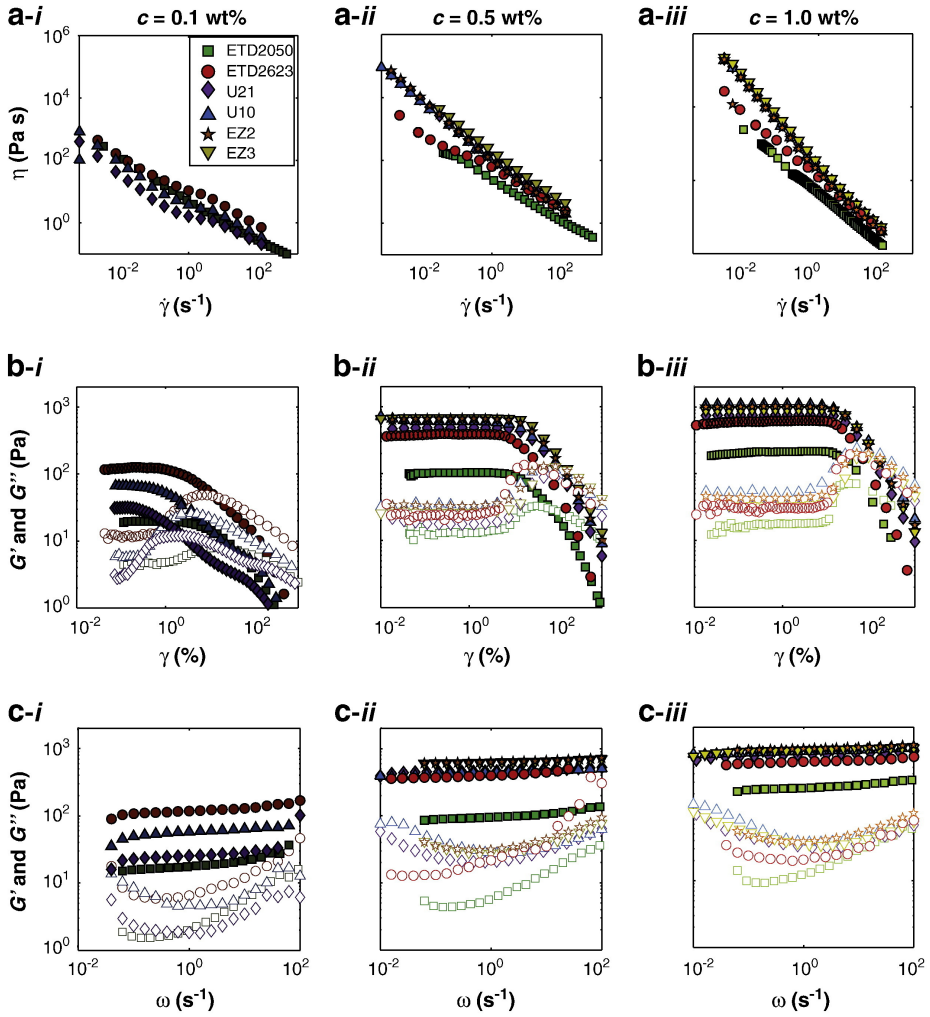

Figure 1.19: Rheological characterization of 6 different Carbopol samples at concentrations of 0.1 wt.%, 0.5 wt.%, and 1.0 wt.% at a constant temperature of 23 °C. (a) steady shear flow measurements, (b) amplitude sweep tests, and (c) frequency sweep tests. Results are presented graphically, with different symbols representing the specific Carbopol type used. Darker colors denote samples with lower Carbopol concentrations. In the frequency and amplitude sweep test results (b and c), filled symbols represent the storage modulus, G', and open symbols represent the loss modulus, G''.[98]

types and concentrations, G' consistently exceeds G'', indicating predominantly elastic behavior. However, significant differences in G' and G'' values appear across Carbopol types and concentrations. Higher concentrations lead to substantially increased G' and G'' values, signifying enhanced elasticity and structural integrity. The crossover point between G' and G'', varying across Carbopol types and concentrations, marks the onset of non-linear behavior and provides key insights into material strength and structure. The LVR range also expands with increasing concentration.

(c) Frequency Sweep Tests: Finally, this section (Figure 1.19c) examines the fre-

quency dependence of G' and G'' within the LVR established in the amplitude sweep tests. This frequency-dependent behavior reveals information about the structural relaxation timescales of the hydrogels. The consistent trend of increasing G' and G'' with concentration further reinforces the enhanced elasticity and structural integrity of more concentrated samples. Notably, the distinct frequency-dependent responses observed for the different Carbopol types underscore the influence of polymer composition on the complex viscoelastic structure.

Figure 1.19's detailed rheological characterization, encompassing steady shear flow and oscillatory measurements, provides critical insights into the effects of concentration and Carbopol type on the rheological properties. This comprehensive analysis demonstrates that the nature of the liquid-to-solid transition and the threshold concentration are strongly influenced by the interplay between crosslinking density, interparticle interactions, and particle size, all factors which are directly affected by the specific Carbopol composition. This detailed characterization forms a robust foundation for selecting appropriate Carbopol types for various rheological modeling applications.

1.3.1 Carbopol

Poly(carboxylic acid) gels have weak anionic properties and swell in basic solutions.[99,100] Above their pKa (about 4.5-5 for poly(acrylic acid)), carboxyl groups ($-COOH$) ionize to carboxylate anions ($-COO-$) and promote interaction with water dipoles as well as electrostatic repulsion between the charged groups, causing expansion. In contrast, reducing pH leads to protonation of the negatively charged groups, causing gel collapse. Salt addition also promotes shrinking by decreasing the osmotic pressure difference between the gel interior and the surrounding fluid. The addition of salt screens the electrostatic interactions between the charged groups, reducing the osmotic pressure within the gel and causing it to shrink. Poly(carboxylic acid) gels are commonly composed of poly(acrylic acid) (PAA), poly(methacrylic acid) (PMAA), and poly(2-ethylacrylic acid) (PEAA).

Carbopol, the main microgel system used throughout this thesis, is a brand name for crosslinked PAA polymers, also known as carbomers. Initially synthesized by Goodrich in the 1950s, these polymers are crosslinked with polyalkylene ethers or divinyl glycol[101]. The crosslinking density significantly impacts the final gel properties, influencing its swelling capacity, mechanical strength, and rheological behavior. Carbopol synthesis typically involves inverse emulsion polymerization in an organic solvent[102,103], resulting in a structure with a denser core and thinner outer shell due to a two-stage polymerization process. Carbopol, produced by Lubrizol, is widely used in cosmetics as a thickening, stabilizing, suspending, and emulsifying agent; moreover, it is used in pharmaceuticals[104,105] and various other industrial applications due to its non-toxicity and stability. The broad range of applications highlights the versatility and desirable properties of Carbopol, stemming from its unique structural and rheological characteristics. In their anhydrous state, they are powders with an average particle size of hundreds of nanometers and a molecular weight of around 100 MDa[106].

Despite its charged nature, its tunability makes it a valuable model system for studying YSF[94,107–109], while its transparency allows optical access[85,110]. Its elastic properties primarily result from jamming rather than other crosslinking mechanisms; it can be considered a microgel-based soft glass, often described by the Herschel-Bulkley model[94,111,112]. However, thixotropy has been observed in some systems[109,113,114], influenced by microstructure variations arising from preparation methods or additives[81,101,110,115,116]. The thixotropic behavior, characterized by the time-dependent recovery of viscosity after

shear, highlights the complex interplay between the microstructure and the rheological response of Carbopol gels, influenced by preparation conditions and additives.

Carbopol neutralized physical gels have been used in numerous applications over the past 40 years[94,94,107–109]. These materials are inexpensive, transparent and harmless, easy to prepare and clean. Carbopol aqueous gels are also quite popular for researchers involved in rheology and non-Newtonian fluid mechanics.

1.3.2 Dispersion protocol

Various commercial formulations exist, differing in size, softness and presence of other species. This section details the preparation of Carbopol dispersions using Carbopol 971 NF (Lubrizol) (C971NF), used for most of the experiments reported in this thesis[117]. C971NF is a flocculated powder consisting of particles averaging 0.2 μm in diameter[118], forming agglomerates up to 7 μm. C971NF increases its solubility and swells significantly in water (up to 1000 times its original volume) at pH around 6-8. Due to C971NF tendency to form clumps and to the dependence of rheological properties on shear history or presence of heterogeneities, a careful dispersion protocol is necessary, as described in detail below.

Preparation in water

C971NF dispersions are highly pH-sensitive. To prepare water-based dispersions, C971NF powder was added to Milli-Q water. The initial mixture was dispersed using a LABINCO L46 vortex mixer at maximum speed (2500 rpm) for 2 hours to achieve a homogeneous distribution of the polymer. This result in a strongly acidic dispersion (pH $\approx$ 3).

To promote swelling of the microgel particles and enhance homogeneity, the pH of the dispersion was adjusted using 10M NaOH. NaOH was added dropwise, with each addition followed by one hour of mixing with the vortex mixer at 22°C to ensure complete homogenization. The pH was monitored with a pH meter after each addition, and the total added NaOH was recorded for each sample. Preparation time varied depending on the desired Carbopol concentration; higher concentrations (above 5%) required longer processing times, up to 10 hours of mixing with a vortex mixer. In some cases, for optimal homogenization of high-concentration dispersions, samples were further treated with an ultrasonic cleaner (CEIA CP104 Standard Ultrasonic Cleaner) for one hour at 22°C. Following preparation, dispersions were stored at room temperature in 20 ml batches.

Preparation in non-aqueous, neutralizable solvents

The dispersibility, swelling behavior and rheological properties of C971NF were investigated in various solvents, with various degrees of polarity. Dispersibility was verified through visual inspection and rheological characterization was performed only in fully homogeneous and transparent samples. This section describes the preparation of homogeneous C971NF dispersions using two classes of solvents: protic solvents, in which neutralization is possible, and aprotic solvents, not susceptible to neutralization. All solvents were purchased from Sigma-Aldrich.

These solvents not only disperse C971NF but also exhibit pH-dependent properties upon neutralization. Carbopol powder was added to Propylene Glycol (PG) ($CH_3CH(OH)CH_2OH$, MW = 76.09 Da), Glycerol ($HOCH_2CH(OH)CH_2OH$, MW = 92.09 Da, >99%), Polyethylene Glycol 400 (PEG400, $H(OCH_2CH_2)_nOH$, MW = 400 Da), and Polyethylene Glycol 200 (PEG200, $H(OCH_2CH_2)_nOH$, MW = 200 Da). As for the

water-based dispersions, initial mixing was performed using a LABINCO L46 vortex mixer at 2500 rpm for 2 hours. For concentrations exceeding 3% in each solvent, the higher viscosity required the use of an ultrasonic bath for 1 hour at 50°C to promote homogenization. Once a transparent and homogeneous mixture was obtained, the pH was estimated using Whatman indicator papers. Although proper measurement with a pH-meter was not possible in non-aqueous solvents, consistent reading with different type of strips was verified. In the following, such estimates are referred to as 'apparent pH' and reported in Table 1.1

Table 1.1: Apparent pH Values of Solvents Before and After Neutralizer

Solvent	Apparent pH	pH after adding C971 NF (5 wt%)	pH after adding NaOH
PEG 200	6.5	6	7
PEG 400	6.5	6	7
PG	6	4.5	7
Glycerol	7	5	7

NaOH powder was then added incrementally, with 1 hour of mixing following each addition. The apparent pH was measured after each addition. For comparison, the apparent pH of the pure solvents and their mixtures with NaOH powder are also reported in Table 1.1

Note that neutralized PEG400 and PEG 200 samples were discarded due to a color change (yellowing) observed in the pure solvents upon addition of NaOH. All preparations, except those requiring ultrasonic treatment at 50°C, were conducted at room temperature (22°C).

In selected cases (aqueous suspension 1 wt%), the same procedure was applied for the addition of an alternative base, namely Triethylamine (TEA) , for comparison.

Preparation in non-aqueous, non-neutralizable solvents

Certain solvents effectively disperse C971NF, although pH cannot be defined nor tuned. This category includes Dimethyl sulfoxide (DMSO)($(CH_3)_2SO$, MW = 78.13 Da) and N,N-Dimethylformamide (DMF) ($HCON(CH_3)_2$, MW = 73.09 Da). Additional solvents, such as Methanol (CH_3OH, MW = 32.04 Da) and 1-Methyl-2-pyrrolidone (NMP) (C_5H_9NO, MW = 99.13 Da), exhibited less effective dispersion of C971NF, with a milky appearance, and their properties remained unchanged addition of NaOH. Dispersion preparation for all these solvents involved adding C971NF powder, followed by mixing with the vortex mixer at 2500 rpm for at least 2 hours. All preparations were carried out at room temperature (22°C).

1.4 Dynamic Light Scattering

Determining the size distribution of microgels is crucial for understanding their behavior and optimizing their applications[60,81,85,101,110,119–123]. These soft, cross-linked polymeric networks exhibit significant size variability influenced by factors such as solvent

Table 1.2: C971 NF in different solvents (wt%)

Solvent	C971 NF Concentration (wt%)							
Water + NaOH	5	4	3	2	1	0.7	0.5	0.4
Water + NaOH	0.3	0.2	0.15	0.12	0.07	0.05	0.03	0.01
Water	5	4	3	2	1.5	1	0.8	0.6
Water	0.5	0.4	0.3					
PG	5	4	3	2	1.75	1.5	1	
PG + NaOH	4	3	2	1.75	1.25	1	0.8	0.75
PEG 400	6	5	4	3	2	1.75	1	
PEG 200	6	5	4	3	2	1		
Glycerol	3	2	1	0.5				
DMF	6	5	4	3	2	1	0.7	0.5
DMF	0.3							
DMSO	10	6	5	4	3	2	1	0.8

quality, pH, temperature, ionic strength, and monomer composition[107,122,124–128]. Consequently, appropriate size measurement techniques must be carefully selected based on the required information and the limitations of each method.

While direct imaging techniques like electron microscopy (SEM, TEM) and confocal microscopy provide detailed morphological information, including particle shape and surface characteristics[101,128,129], they often require extensive sample preparation, are expensive and may not readily yield statistically robust size distributions from large populations[101,122,129]. Furthermore, they are not readily applicable to non-aqueous solutions and do not have access to the associated solvent layers.

Dynamic Light Scattering (DLS) represents a complementary, non-invasive technique measuring the motion of colloidal particles in solution[101,119,120,122,128–130]. From fluctuations in scattered light intensity over time, DLS allows to determine the mobility and thus the size and shape of particles in a solution. In concentrated polymer solutions, these fluctuations reflect diffusion within a complex environment, potentially including collective motions. However, in dilute solutions, diffusion is mostly determined by Brownian motion, i.e. the random movement caused by collisions with solvent molecules. Such motion leads to a mean square displacement ($\langle x^2 \rangle$) that grows linearly with time, Equation 1.20:

$$\langle x^2 \rangle = 6Dt \quad \text{(3-dimensional space)} \tag{1.20}$$

where D is the diffusion coefficient, linked to particle size, medium properties, and thermal energy via the Stokes-Einstein equation (Equation 1.21):

$$D = \frac{k_B T}{6\pi\eta R_h} \tag{1.21}$$

Here, k_B is the Boltzmann constant, T is the absolute temperature, η is the medium viscosity, and R_h is the hydrodynamic radius (the radius of a sphere with an equivalent volume to the particle, including the solvent dragged by the particle).

In DLS, scattered photons from an ensemble of particles (not too big as compared to light wavelength) interfere constructively or destructively depending on their relative position, creating a speckle pattern of fluctuating light intensity. These fluctuations of the light detected at a certain angle - and thus correspond to a typical lengthscale - are used to compute the intensity correlation function, $G_2(\tau)$ (Equation 1.22):

$$G_2(\tau) = \langle I(t)I(t+\tau)\rangle \tag{1.22}$$

where $\langle\rangle$ denotes a time average, $I(t)$ is the intensity at time t, and τ is the lag time between two acquisitions. $G_2(\tau)$ decays from $\langle I^2(0)\rangle$ to $\langle I\rangle^2$, and is normalized to $g_2(\tau)$ (Equation 1.23):

$$g_2(\tau) = \frac{\langle I(t)I(t+\tau)\rangle}{\langle I(t)\rangle^2} \tag{1.23}$$

Particle motion can also be described in terms of the electric field correlation function, $g_1(\tau)$ (Equation 1.24):

$$g_1(\tau) = \frac{\langle E(t)E(t+\tau)\rangle}{\langle E(t)\rangle^2} \tag{1.24}$$

$g_1(\tau)$ and $g_2(\tau)$ 1.23 are related by the (Equation 1.25), assuming homodyne scattering and random Gaussian photon counting:

$$g_2(\tau) = b + \beta|g_1(\tau)|^2 \tag{1.25}$$

where b is the baseline (typically 1) and β is the coherence factor, which depends on the scattering properties of the particles and the features of the collection setup (detector area, optical alignment, etc.). $g_1(\tau)$ decays exponentially (Equation 1.26):

$$g_1(\tau) = e^{-\Gamma\tau} \tag{1.26}$$

where Γ is the decay constant. Substituting this into the Siegert relation gives:

$$g_2(\tau) = 1 + \beta e^{-2\Gamma\tau} \tag{1.27}$$

In the monodisperse case, Γ is related to the diffusion coefficient and the Bragg wave vector, q (Equation 1.28):

$$\Gamma = Dq^2 \tag{1.28}$$

Finally, combining these equations yields:

$$g_2(\tau) = 1 + \beta e^{-2Dq^2\tau} \tag{1.29}$$

By fitting experimental data to exponential decays, the decay time constant can be determined, allowing for calculation of D and subsequently R_h using Equation 1.21, if the viscosity is known.

For polydisperse samples, $g_1(\tau)$ becomes an intensity-weighted integral over a distribution of decay rates (Equation 1.30):

$$g_1(\tau) = \int_0^\infty G(\Gamma)e^{-\Gamma\tau}d\Gamma \tag{1.30}$$

In such cases a simple exponential decay is insufficient to accurately model the dynamics. Instead, g_1 can be expressed as a stretched (Kohlrausch) exponential function, incorporating a stretching exponent β and thus expressed as:

$$g_1(\tau) = C + A\exp\left[-\left(\frac{\tau}{\tau_0}\right)^\beta\right] \tag{1.31}$$

where τ_0 is a characteristic relaxation time, and β (with $0 < \beta \leq 1$) describes the degree of stretching. A value of $\beta = 1$ recovers the standard exponential decay, while $\beta < 1$ indicates a broader, more heterogeneous distribution of decay processes. This approach provides a more nuanced representation of the dynamics in complex fluids, such as microgel dispersions, where multiple relaxation processes contribute to the observed behavior.

DLS efficiency, suitability for dilute and semi-dilute dispersions, and non-destructive nature are advantageous. However, polydispersity and multiple scattering, especially in concentrated samples, can lead to size determination inaccuracies[122]. Furthermore, the measured R_h may differ from other size measures depending on the microgel-solvent interaction. Studies highlighting the influence of polymerization conditions on microgel morphology and size and the challenges in accurately measuring microgel sizes underscore the importance of considering the limitations of each technique and the value of multiple methods for comprehensive characterization[122,128].

Bibliography

[1] B. Dobraszczyk and M. Morgenstern. Rheology and the breadmaking process. *Journal of cereal Science*, 38(3):229–245, 2003.

[2] R. B. Bird, G. Dai, and B. J. Yarusso. The rheology and flow of viscoplastic materials. *Reviews in chemical engineering*, 1(1):1–70, 1983.

[3] P. Coussot. Rheophysics. *Matter in all its states, Paris-Est: Springer*, 2014.

[4] R. Cerbino and V. Trappe. Introduction to viscoelasticity and plasticity, and their relation to the underlying microscopic dynamics in soft matter systems. *Physica A: Statistical Mechanics and its Applications*, 631:128653, 2023.

[5] C. W. Macosko. Rheology principles. *Measurements and Applications*, 1994.

[6] C. Roberto and T. Véronique. Introduction to viscoelasticity and plasticity, and their relation to the underlying microscopic dynamics in soft matter systems. *Physica A: Statistical Mechanics and its Applications*, 631:128653, 2023.

[7] A. Gemant. The conception of a complex viscosity and its application to dielectrics. *Transactions of the Faraday Society*, 31:1582–1590, 1935.

[8] P. Hébraud, F. Lequeux, J. Munch, and D. Pine. Yielding and rearrangements in disordered emulsions. *Physical Review Letters*, 78(24):4657, 1997.

[9] R. Höhler, S. Cohen-Addad, and H. Hoballah. Periodic nonlinear bubble motion in aqueous foam under oscillating shear strain. *Physical review letters*, 79(6):1154, 1997.

[10] G. Petekidis, A. Moussaid, and P. Pusey. Rearrangements in hard-sphere glasses under oscillatory shear strain. *physical review E*, 66(5):051402, 2002.

[11] N. C. Keim and P. E. Arratia. Yielding and microstructure in a 2d jammed material under shear deformation. *Soft Matter*, 9(27):6222–6225, 2013.

[12] E. D. Knowlton, D. J. Pine, and L. Cipelletti. A microscopic view of the yielding transition in concentrated emulsions. *Soft Matter*, 10(36):6931–6940, 2014.

[13] A. Basu, Q. Wen, X. Mao, T. Lubensky, P. A. Janmey, and A. Yodh. Nonaffine displacements in flexible polymer networks. *Macromolecules*, 44(6):1671–1679, 2011.

[14] R. G. Larson. *The structure and rheology of complex fluids*, volume 150. Oxford university press New York, 1999.

[15] P. Coussot. Rheophysics. switzerland: Springer international pu doi: 10.1007. *Springer International Pu*, 2016.

[16] G. Youssef. *Applied mechanics of polymers: properties, processing, and behavior*. Elsevier, 2021.

[17] A. Pertsinidis and X. S. Ling. Video microscopy and micromechanics studies of one-and two-dimensional colloidal crystals. *New Journal of Physics*, 7(1):33, 2005.

[18] N. W. Tschoegl. *The phenomenological theory of linear viscoelastic behavior: an introduction*. Springer Science & Business Media, 2012.

[19] G. J. Donley, P. K. Singh, A. Shetty, and S. A. Rogers. Elucidating the g" overshoot in soft materials with a yield transition via a time-resolved experimental strain decomposition. *Proceedings of the National Academy of Sciences*, 117(36):21945–21952, 2020.

[20] K. Hyun, M. Wilhelm, C. O. Klein, K. S. Cho, J. G. Nam, K. H. Ahn, S. J. Lee, R. H. Ewoldt, and G. H. McKinley. A review of nonlinear oscillatory shear tests: Analysis and application of large amplitude oscillatory shear (laos). *Progress in polymer science*, 36(12):1697–1753, 2011.

[21] Y. Liu, H. H. Winter, and S. L. Perry. Linear viscoelasticity of complex coacervates. *Advances in colloid and interface science*, 239:46–60, 2017.

[22] J. Van der Gucht, E. Spruijt, M. Lemmers, and M. A. C. Stuart. Polyelectrolyte complexes: Bulk phases and colloidal systems. *Journal of colloid and interface science*, 361(2):407–422, 2011.

[23] Å. Öhrlund. Evaluation of rheometry amplitude sweep cross-over point as an index of flexibility for ha fillers. *Journal of Cosmetics, Dermatological Sciences and Applications*, 8:47–54, 2018.

[24] S. Ozkan, C. Alonso, and R. McMullen. Rheological fingerprinting as an effective tool to guide development of personal care formulations. *International Journal of Cosmetic Science*, 42(6):536–547, 2020.

[25] T. Mason, J. Bibette, and D. Weitz. Elasticity of compressed emulsions. *Physical review letters*, 75(10):2051, 1995.

[26] S. A. Rogers, M. A. Calabrese, and N. J. Wagner. Rheology of branched wormlike micelles. *Current opinion in colloid & interface science*, 19(6):530–535, 2014.

[27] A. K. Gurnon, C. Lopez-Barron, M. J. Wasbrough, L. Porcar, and N. J. Wagner. Spatially resolved concentration and segmental flow alignment in a shear-banding solution of polymer-like micelles. *ACS Macro Letters*, 3(3):276–280, 2014.

[28] S. Rogers. Large amplitude oscillatory shear: Simple to describe, hard to interpret. *Physics Today*, 71(7):34–40, 2018.

[29] H. J. Barlow, J. O. Cochran, and S. M. Fielding. Ductile and brittle yielding in thermal and athermal amorphous materials. *Physical Review Letters*, 125(16):168003, 2020.

[30] G. R. Desiraju and J. Hulliger. Current opinion in solid state & materials science-molecular crystals and materials. *Current Opinion in Solid State & Materials Science*, 2(5):105–106, 2001.

[31] N. J. Balmforth, I. A. Frigaard, and G. Ovarlez. Yielding to stress: recent developments in viscoplastic fluid mechanics. *Annual review of fluid mechanics*, 46(1): 121–146, 2014.

[32] D. Bonn, M. M. Denn, L. Berthier, T. Divoux, and S. Manneville. Yield stress materials in soft condensed matter. *Reviews of Modern Physics*, 89(3):035005, 2017.

[33] H. Barnes and K. Walters. The yield stress myth? *Rheologica acta*, 24:323–326, 1985.

[34] P. Coussot. Bingham's heritage. *Rheologica Acta*, 56:163–176, 2017.

[35] A. Malkin, V. Kulichikhin, and S. Ilyin. A modern look on yield stress fluids. *Rheologica Acta*, 56:177–188, 2017.

[36] A. M. Putz and T. I. Burghelea. The solid–fluid transition in a yield stress shear thinning physical gel. *Rheologica Acta*, 48:673–689, 2009.

[37] C. J. Dimitriou, R. H. Ewoldt, and G. H. McKinley. Describing and prescribing the constitutive response of yield stress fluids using large amplitude oscillatory shear stress (laostress). *Journal of Rheology*, 57(1):27–70, 2013.

[38] P. R. de Souza Mendes. Modeling the thixotropic behavior of structured fluids. *Journal of Non-Newtonian Fluid Mechanics*, 164(1-3):66–75, 2009.

[39] R. K. Avery, H. Albadawi, M. Akbari, Y. S. Zhang, M. J. Duggan, D. V. Sahani, B. D. Olsen, A. Khademhosseini, and R. Oklu. An injectable shear-thinning biomaterial for endovascular embolization. *Science translational medicine*, 8(365):365ra156–365ra156, 2016.

[40] T. Bhattacharjee, S. M. Zehnder, K. G. Rowe, S. Jain, R. M. Nixon, W. G. Sawyer, and T. E. Angelini. Writing in the granular gel medium. *Science advances*, 1(8): e1500655, 2015.

[41] A. Z. Nelson, K. S. Schweizer, B. M. Rauzan, R. G. Nuzzo, J. Vermant, and R. H. Ewoldt. Designing and transforming yield-stress fluids. *Current Opinion in Solid State and Materials Science*, 23(5):100758, 2019.

[42] J. T. Muth, P. G. Dixon, L. Woish, L. J. Gibson, and J. A. Lewis. Architected cellular ceramics with tailored stiffness via direct foam writing. *Proceedings of the National Academy of Sciences*, 114(8):1832–1837, 2017.

[43] K. Markstedt, A. Mantas, I. Tournier, H. Martínez Ávila, D. Hagg, and P. Gatenholm. 3d bioprinting human chondrocytes with nanocellulose–alginate bioink for cartilage tissue engineering applications. *Biomacromolecules*, 16(5):1489–1496, 2015.

[44] C. B. Highley, K. H. Song, A. C. Daly, and J. A. Burdick. Jammed microgel inks for 3d printing applications. *Advanced Science*, 6(1):1801076, 2019.

[45] J. A. Lewis. Direct-write assembly of ceramics from colloidal inks. *Current Opinion in Solid State and Materials Science*, 6(3):245–250, 2002.

[46] B. M. Rauzan, A. Z. Nelson, S. E. Lehman, R. H. Ewoldt, and R. G. Nuzzo. Emulsions: Particle-free emulsions for 3d printing elastomers (adv. funct. mater. 21/2018). *Advanced Functional Materials*, 28(21):1870141, 2018.

[47] E. R. Weeks. Soft jammed materials. *Stat. Phys. Complex Fluids*, 2:87, 2007.

[48] C. Angell. Relaxation in liquids, polymers and plastic crystals—strong/fragile patterns and problems. *Journal of Non-Crystalline Solids*, 131:13–31, 1991.

[49] C. S. O'hern, L. E. Silbert, A. J. Liu, and S. R. Nagel. Jamming at zero temperature and zero applied stress: The epitome of disorder. *Physical Review E*, 68(1):011306, 2003.

[50] M. van Hecke. Jamming of soft particles: geometry, mechanics, scaling and isostaticity. *Journal of Physics: Condensed Matter*, 22(3):033101, 2009.

[51] A. Ikeda, L. Berthier, and P. Sollich. Unified study of glass and jamming rheology in soft particle systems. *Physical review letters*, 109(1):018301, 2012.

[52] R. Besseling, L. Isa, E. R. Weeks, and W. C. Poon. Quantitative imaging of colloidal flows. *Advances in colloid and interface science*, 146(1-2):1–17, 2009.

[53] T. Voigtmann. Nonlinear glassy rheology. *Current opinion in colloid & interface science*, 19(6):549–560, 2014.

[54] M. L. Falk and J. S. Langer. Dynamics of viscoplastic deformation in amorphous solids. *Physical Review E*, 57(6):7192, 1998.

[55] M. Dinkgreve, J. Paredes, M. M. Denn, and D. Bonn. On different ways of measuring "the" yield stress. *Journal of non-Newtonian fluid mechanics*, 238:233–241, 2016.

[56] V. De Graef, F. Depypere, M. Minnaert, and K. Dewettinck. Chocolate yield stress as measured by oscillatory rheology. *Food Research International*, 44(9):2660–2665, 2011.

[57] F. Rouyer, S. Cohen-Addad, and R. Höhler. Is the yield stress of aqueous foam a well-defined quantity? *Colloids and Surfaces A: Physicochemical and Engineering Aspects*, 263(1-3):111–116, 2005.

[58] F. Cyriac, P. Lugt, and R. Bosman. On a new method to determine the yield stress in lubricating grease. *Tribology Transactions*, 58(6):1021–1030, 2015.

[59] C. Christopoulou, G. Petekidis, B. Erwin, M. Cloitre, and D. Vlassopoulos. Ageing and yield behaviour in model soft colloidal glasses. *Philosophical Transactions of the Royal Society A: Mathematical, Physical and Engineering Sciences*, 367(1909):5051–5071, 2009.

[60] T. Mason, J. Bibette, and D. Weitz. Yielding and flow of monodisperse emulsions. *Journal of colloid and interface science*, 179(2):439–448, 1996.

[61] A. Saint-Jalmes and D. J. Durian. Vanishing elasticity for wet foams: Equivalence with emulsions and role of polydispersity. *Journal of Rheology*, 43(6):1411–1422, 1999.

[62] H. A. Barnes and Q. D. Nguyen. Rotating vane rheometry—a review. *Journal of non-Newtonian fluid mechanics*, 98(1):1–14, 2001.

[63] P. C. Møller, J. Mewis, and D. Bonn. Yield stress and thixotropy: on the difficulty of measuring yield stresses in practice. *Soft matter*, 2(4):274–283, 2006.

[64] M. Dinkgreve, M. M. Denn, and D. Bonn. "everything flows?": elastic effects on startup flows of yield-stress fluids. *Rheologica Acta*, 56(3):189–194, 2017.

[65] P. Coussot. Yield stress fluid flows: A review of experimental data. *Journal of Non-Newtonian Fluid Mechanics*, 211:31–49, 2014.

[66] A. James, D. Williams, and P. Williams. Direct measurement of static yield properties of cohesive suspensions. *Rheologica acta*, 26:437–446, 1987.

[67] Q. D. Nguyen, T. Akroyd, D. C. D. Kee, and L. Zhu. Yield stress measurements in suspensions: an inter-laboratory study. *Korea-Australia Rheology Journal*, 18(1): 15–24, 2006.

[68] L. Zhu, N. Sun, K. Papadopoulos, and D. De Kee. A slotted plate device for measuring static yield stress. *Journal of Rheology*, 45(5):1105–1122, 2001.

[69] E. C. Bingham. *Fluidity and Plasticity: By Eugene C. Bingham...* McGraw-Hill Book Company, Incorporated, 1922.

[70] P. Hébraud and F. Lequeux. Mode-coupling theory for the pasty rheology of soft glassy materials. *Physical review letters*, 81(14):2934, 1998.

[71] L. Bocquet, A. Colin, and A. Ajdari. Kinetic theory of plastic flow in soft glassy materials. *Physical review letters*, 103(3):036001, 2009.

[72] V. Mansard, A. Colin, P. Chaudhuri, and L. Bocquet. A molecular dynamics study of non-local effects in the flow of soft jammed particles. *Soft matter*, 9(31):7489–7500, 2013.

[73] N. D. Denkov, S. Tcholakova, K. Golemanov, K. Ananthpadmanabhan, and A. Lips. The role of surfactant type and bubble surface mobility in foam rheology. *Soft Matter*, 5(18):3389–3408, 2009.

[74] J. R. Seth, L. Mohan, C. Locatelli-Champagne, M. Cloitre, and R. T. Bonnecaze. A

micromechanical model to predict the flow of soft particle glasses. *Nature materials*, 10(11):838–843, 2011.

[75] M. Dinkgreve, J. Paredes, M. Michels, and D. Bonn. Universal rescaling of flow curves for yield-stress fluids close to jamming. *Physical Review E*, 92(1):012305, 2015.

[76] N. Koumakis, A. Pamvouxoglou, A. Poulos, and G. Petekidis. Direct comparison of the rheology of model hard and soft particle glasses. *Soft Matter*, 8(15):4271–4284, 2012.

[77] I. Kaneda and A. Sogabe. Rheological properties of water swellable microgel polymerized in a confined space. *Colloids and Surfaces A: Physicochemical and Engineering Aspects*, 270:163–170, 2005.

[78] C. Pellet and M. Cloitre. The glass and jamming transitions of soft polyelectrolyte microgel suspensions. *Soft matter*, 12(16):3710–3720, 2016.

[79] V. Herschel. Consistency of measurements rubber-benzene solutions. *Kolloid-Zeit.*, 39:291–300, 1926.

[80] A. Z. Nelson and R. H. Ewoldt. Design of yield-stress fluids: A rheology-to-structure inverse problem. *Soft matter*, 13(41):7578–7594, 2017.

[81] J.-Y. Kim, J.-Y. Song, E.-J. Lee, and S.-K. Park. Rheological properties and microstructures of carbopol gel network system. *Colloid and Polymer Science*, 281(7): 614–623, 2003.

[82] A. Ghosh, G. Chaudhary, J. G. Kang, P. V. Braun, R. H. Ewoldt, and K. S. Schweizer. Linear and nonlinear rheology and structural relaxation in dense glassy and jammed soft repulsive pnipam microgel suspensions. *Soft matter*, 15(5):1038–1052, 2019.

[83] M. Caggioni, V. Trappe, and P. T. Spicer. Variations of the herschel–bulkley exponent reflecting contributions of the viscous continuous phase to the shear rate-dependent stress of soft glassy materials. *Journal of Rheology*, 64(2):413–422, 2020.

[84] A. Gopal and D. Durian. Shear-induced "melting" of an aqueous foam. *Journal of Colloid and Interface Science*, 213(1):169–178, 1999.

[85] M. Cloitre, R. Borrega, F. Monti, and L. Leibler. Structure and flow of polyelectrolyte microgels: from suspensions to glasses. *Comptes rendus. Physique*, 4(2):221–230, 2003.

[86] W. A. Laftah, S. Hashim, and A. N. Ibrahim. Polymer hydrogels: A review. *Polymer-Plastics Technology and Engineering*, 50(14):1475–1486, 2011.

[87] E. M. Ahmed. Hydrogel: Preparation, characterization, and applications: A review. *Journal of advanced research*, 6(2):105–121, 2015.

[88] B. Rodriguez, M. Wolfe, and M. Fryd. Nonuniform swelling of alkali swellable microgels. *Macromolecules*, 27(22):6642–6647, 1994.

[89] S.-k. Ahn, R. M. Kasi, S.-C. Kim, N. Sharma, and Y. Zhou. Stimuli-responsive polymer gels. *Soft Matter*, 4(6):1151–1157, 2008.

[90] J. K. Oh, R. Drumright, D. J. Siegwart, and K. Matyjaszewski. The development of microgels/nanogels for drug delivery applications. *Progress in polymer science*, 33 (4):448–477, 2008.

[91] H. Kawaguchi. Thermoresponsive microhydrogels: preparation, properties and applications. *Polymer International*, 63(6):925–932, 2014.

[92] Z. Jaworski, T. Spychaj, A. Story, and G. Story. Carbomer microgels as model yield-stress fluids. *Reviews in Chemical Engineering*, 38(7):881–919, 2022.

[93] L. A. Lyon and A. Fernandez-Nieves. The polymer/colloid duality of microgel suspensions. *Annual review of physical chemistry*, 63(1):25–43, 2012.

[94] J.-M. Piau. Carbopol gels: Elastoviscoplastic and slippery glasses made of individual swollen sponges: Meso-and macroscopic properties, constitutive equations and scaling laws. *Journal of non-newtonian fluid mechanics*, 144(1):1–29, 2007.

[95] D. Vlassopoulos and M. Cloitre. Tunable rheology of dense soft deformable colloids. *Current opinion in colloid & interface science*, 19(6):561–574, 2014.

[96] D. Vlassopoulos and M. Cloitre. Bridging the gap between hard and soft colloids. *Soft Matter*, 8(15):4010–4013, 2012.

[97] P. J. Flory. Molecular theory of rubber elasticity. *Polymer journal*, 17(1):1–12, 1985.

[98] E. Di Giuseppe, F. Corbi, F. Funiciello, A. Massmeyer, T. Santimano, M. Rosenau, and A. Davaille. Characterization of carbopol® hydrogel rheology for experimental tectonics and geodynamics. *Tectonophysics*, 642:29–45, 2015.

[99] E. Jabbari and S. Nozari. Swelling behavior of acrylic acid hydrogels prepared by γ radiation crosslinking of polyacrylic acid in aqueous solution. *European Polymer Journal*, 36(12):2685–2692, 2000.

[100] T. Swift, L. Swanson, M. Geoghegan, and S. Rimmer. The ph-responsive behaviour of poly (acrylic acid) in aqueous solution is dependent on molar mass. *Soft matter*, 12(9):2542–2549, 2016.

[101] P. Lefrançois, E. Ibarboure, B. Payré, E. Gontier, J.-F. Le Meins, and C. Schatz. Insights into c arbopol gel formulations: microscopy analysis of the microstructure and the influence of polyol additives. *Journal of Applied Polymer Science*, 132(46), 2015.

[102] D. Benda, J. Šňupárek, and V. Čermák. Inverse emulsion polymerization of acrylamide and salts of acrylic acid. *European polymer journal*, 33(8):1345–1352, 1997.

[103] P. Menut, S. Seiffert, J. Sprakel, and D. A. Weitz. Does size matter? elasticity of compressed suspensions of colloidal-and granular-scale microgels. *Soft matter*, 8 (1):156–164, 2012.

[104] G. Bonacucina, S. Martelli, and G. F. Palmieri. Rheological, mucoadhesive and release properties of carbopol gels in hydrophilic cosolvents. *International journal of pharmaceutics*, 282(1-2):115–130, 2004.

[105] L. Boulmedarat, J. L. Grossiord, E. Fattal, and A. Bochot. Influence of methyl-β-cyclodextrin and liposomes on rheological properties of carbopol® 974p nf gels. *International journal of pharmaceutics*, 254(1):59–64, 2003.

[106] B. Barry and M. Meyer. The rheological properties of carbopol gels ii. oscillatory properties of carbopol gels. *International Journal of Pharmaceutics*, 2(1):27–40, 1979.

[107] J. Carnali and M. Naser. The use of dilute solution viscometry to characterize the network properties of carbopol microgels. *Colloid and Polymer Science*, 270:183–193, 1992.

[108] S. Curran, R. Hayes, A. Afacan, M. Williams, and P. A. Tanguy. Properties of carbopol solutions as models for yield-stress fluids. *Journal of food science*, 67(1): 176–180, 2002.

[109] T. Divoux, D. Tamarii, C. Barentin, and S. Manneville. Transient shear banding in a simple yield stress fluid. *Physical review letters*, 104(20):208301, 2010.

[110] F. Oppong and J. De Bruyn. Mircorheology and jamming in a yield-stress fluid. *Rheologica acta*, 50:317–326, 2011.

[111] R. Ketz, R. Prud'homme, and W. Graessley. Rheology of concentrated microgel solutions. *Rheologica acta*, 27:531–539, 1988.

[112] B. D. Jofore, P. Erni, G. Vleminckx, P. Moldenaers, and C. Clasen. Rheology of microgels in single particle confinement. *Rheologica Acta*, 54(7):581–600, 2015.

[113] M. Dinkgreve, M. Fazilati, M. Denn, and D. Bonn. Carbopol: From a simple to a thixotropic yield stress fluid. *Journal of Rheology*, 62(3):773–780, 2018.

[114] G. J. Donley, J. R. de Bruyn, G. H. McKinley, and S. A. Rogers. Time-resolved dynamics of the yielding transition in soft materials. *Journal of Non-Newtonian Fluid Mechanics*, 264:117–134, 2019.

[115] R. Barreiro-Iglesias, C. Alvarez-Lorenzo, and A. Concheiro. Poly (acrylic acid) microgels (carbopol® 934)/surfactant interactions in aqueous media: Part i: Non-ionic surfactants. *International journal of pharmaceutics*, 258(1-2):165–177, 2003.

[116] Z. Shao, A. S. Negi, and C. O. Osuji. Role of interparticle attraction in the yielding response of microgel suspensions. *Soft Matter*, 9(22):5492–5500, 2013.

[117] P. Panzade and P. K. Puranik. Carbopol polymers: A versatile polymer for pharmaceutical applications. *Research Journal of Pharmacy and Technology*, 3(3):672–675, 2010.

[118] Lubrizol. Molecular weight of carbopol®* and pemulen®* polymers. Technical Report 222, Lubrizol Technical Data Sheet, 2007.

[119] M. Karg, A. Pich, T. Hellweg, T. Hoare, L. A. Lyon, J. Crassous, D. Suzuki, R. A. Gumerov, S. Schneider, I. I. Potemkin, et al. Nanogels and microgels: From model colloids to applications, recent developments, and future trends. *Langmuir*, 35(19): 6231–6255, 2019.

[120] H. Nur, V. Pinkrah, J. Mitchell, L. Benée, and M. Snowden. Synthesis and properties of polyelectrolyte microgel particles. *Advances in colloid and interface science*, 158(1-2):15–20, 2010.

[121] T. Mason and D. Weitz. Linear viscoelasticity of colloidal hard sphere suspensions near the glass transition. *Physical review letters*, 75(14):2770, 1995.

[122] D. Lee, I. A. Gutowski, A. E. Bailey, L. Rubatat, J. R. de Bruyn, and B. J. Frisken. Investigating the microstructure of a yield-stress fluid by light scattering. *Physical Review E—Statistical, Nonlinear, and Soft Matter Physics*, 83(3):031401, 2011.

[123] B. M. Erwin, M. Cloitre, M. Gauthier, and D. Vlassopoulos. Dynamics and rheology of colloidal star polymers. *Soft Matter*, 6(12):2825–2833, 2010.

[124] M. Shafiei, M. Balhoff, and N. W. Hayman. Chemical and microstructural controls on viscoplasticity in carbopol hydrogel. *Polymer*, 139:44–51, 2018.

[125] N. Taylor and E. Bagley. Dispersions or solutions? a mechanism for certain thickening agents. *Journal of Applied Polymer Science*, 18(9):2747–2761, 1974.

[126] N. Taylor and E. Bagley. Rheology of dispersions of swollen gel particles. *Journal of Polymer Science: Polymer Physics Edition*, 13(6):1133–1144, 1975.

[127] N. Taylor and E. Bagley. Tailoring closely packed gel–particle systems for use as thickening agents. *Journal of Applied Polymer Science*, 21(1):113–122, 1977.

[128] N. Yasmeen, J. Kalecki, P. Borowicz, W. Kutner, and P. S. Sharma. Electrochemically initiated synthesis of polyacrylamide microgels and core-shell particles. *ACS Applied Polymer Materials*, 4(1):452–462, 2022.

[129] I. A. Gutowski, D. Lee, J. R. de Bruyn, and B. J. Frisken. Scaling and mesostructure of carbopol dispersions. *Rheologica acta*, 51:441–450, 2012.

[130] F. A. Plamper and W. Richtering. Functional microgels and microgel systems. *Accounts of chemical research*, 50(2):131–140, 2017.

CHAPTER 2

Microgel rheology in aqueous and non-aqueous solvents

The rheological behavior of Carbopol dispersions in aqueous systems has been extensively investigated[1–9]. On the contrary, research on Carbopol microgels in non-aqueous solvents is limited[10–12]. In particular, previous studies have explored the effects of solvents and co-solvents on Carbopol dispersions[13–15], revealing variations in viscoelasticity. However, the factors governing solvent suitability for Carbopol, solvent-induced swelling and its impact on intermolecular interactions are not fully elucidated.

This chapter aims to identify key parameters determining solvent suitability for Carbopol 971 NF formulation. We first thoroughly study aqueous systems before examining the impact of various non-aqueous solvents on the rheological properties of Carbopol dispersions. We discuss the effect of neutralization in polar solvents and the behavior of aprotic solvents, where neutralization is not possible.

2.1 Introductory concepts and tools

Chapter 1 provided a general introduction to microgels and rheology. The first section of this chapter will address additional concepts related to the swelling of microgels upon variation of solvent properties. Moreover, it will present a computational model used for the estimate of Carbopol compatibility with different solvents.

2.1.1 pH effect on Carbopol microgels

Carbopol microgels, composed of cross-linked polyacrylic acid, exhibit remarkable pH-responsive behavior that significantly impacts their swelling and packing characteristics. This responsiveness originates from the numerous carboxyl groups ($-COOH$) present along the polyacrylic acid backbone (see Figure 2.1). These carboxyl groups act as weak acid residues, making Carbopol a pH-responsive polyelectrolyte[16].

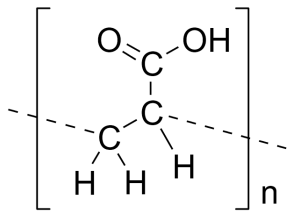

Figure 2.1: The chemical structure of (poly)acrylic acid.

At low pH values, carboxyl groups are predominantly protonated, thus in their neutral or weakly positive ($-COOH$) form. The resulting electrostatic repulsion between these groups is minimal, leading to a relatively compact and shrunk microgel structure[17–22]. This compact state facilitates denser packing of the microgels.

As the pH increases (e.g., around 7), the carboxyl groups progressively deprotonate, transforming into negatively charged ($-COO^-$) groups. The increased electrostatic repulsion between these negatively charged groups causes the polymer chains to expand, resulting in significant microgel swelling[9]. This swelling is a consequence of both osmotic pressure driving water influx into the charged microgel network and the increased volume occupied by the expanding polymer chains. The magnitude of swelling is amplified in low ionic strength solutions where electrostatic repulsions are not effectively screened, in contrast to high ionic strength solutions containing salts like NaCl[23]. The addition of basic excipients further enhances swelling by increasing the degree of ionization and thus electrostatic repulsion[23], whereas acidic excipients have the opposite effect.

In aqueous environments, the final swollen state of Carbopol, such as C971 NF, is influenced by the concentration of uncompensated ions along the polymer backbone[3]. A higher density of these ions leads to greater internal osmotic pressure, facilitating water influx and swelling. The pH-dependent swelling profoundly affects the close-packing behavior of Carbopol microgels. At high pH, the significant swelling increases the effective volume of each microgel, thereby enhancing crowding. This is further coupled to the viscoelastic properties of Carbopol, which are also pH-dependent[9,24–28]. The increased swelling at high pH may alter the microgel's deformability, influencing its ability to interpenetrate with neighboring microgels and thus affecting the overall packing density.

Carbopol's sensitivity to even minor pH or ionic strength changes is well-documented[29]. At high pH, while some deswelling might occur due to osmotic effects, the particles generally do not return to their initial size but rather relax, allowing greater particle motion[29]. The addition of ions, particularly positively charged ions at high pH, can further influence swelling by interacting with the negatively charged groups, reducing osmotic pressure and causing additional deswelling.

The strong interplay between pH, swelling behavior, and particle packing density in Carbopol microgels offers significant potential for applications demanding tunable material properties, including controlled drug release and rheological modification. Our study also focuses on elucidating the influence of pH on Carbopol microgels in both aqueous and non-aqueous media.

2.1.2 Osmotic pressure in microgel suspensions

A proper description of osmotic pressure is crucial for explaining microgel swelling behavior and the resulting macroscopic properties of concentrated suspensions, including rheological characteristics and glass transition phenomena[30]. The unique compressibility of microgels, allowing for both shape and volume changes, makes them exceptional model systems for investigating the fundamental physics of soft matter under confinement[31–35].

The ability to control osmotic pressure, either by adding polymers in solution (such as polyethylene glycol or dextran) or by modifying solvent conditions (pH, temperature, ionic strength)[36,37], enables systematic investigation of microgel swelling across a wide range of states, from highly swollen to completely collapsed[38].

At low concentrations, equilibrium swelling can be reasonably predicted using established theories, such as Flory-Rehner theory[39] and its extensions. However, for

higher and higher concentration, microgels transition from ideal swelling to more complex behavior[40,41], including deswelling and shape changes (faceting)[38]. This transition is particularly sensitive to the interplay between osmotic pressure and the intrinsic mechanical properties of the microgel network, which dictate its ability to withstand compression while maintaining structural integrity. Furthermore, in ionic microgels, swelling equilibrium is significantly influenced by the distribution of counterions within and surrounding the particle network[33,42,43].

In dilute conditions, where microgel interactions are minimal, the total osmotic pressure (π) within a single microgel can be modeled as the balance of three primary contributions[42]:

- **Mixing pressure (π_m)**: This arises from the mixing entropy of polymer chains and solvent molecules. Within the Flory-Huggins framework, it is given by:

$$\frac{\pi_m}{k_B T} = -\left[\frac{\phi_0}{\alpha^3}\left(\chi\phi_0^2 + \ln(1-\phi_0) + \phi_0\right)\right] \tag{2.1}$$

  where k_B is the Boltzmann constant, T is the absolute temperature, ϕ_0 is the polymer volume fraction in the unswollen state, α is the swelling ratio, and χ is the Flory interaction parameter, representing polymer-solvent interaction energies. A positive χ indicates unfavorable interactions, thereby reducing swelling.

- **Elastic pressure (π_{el})**: This pressure results from the elasticity of the crosslinked polymer network. As the microgel swells, the polymer chains are stretched, generating a restoring force that opposes further expansion. A simplified Gaussian model approximates it as:

$$\frac{\pi_{el}}{k_B T} = \frac{N_e}{3\alpha^3} \tag{2.2}$$

  where N_e is the effective number of polymer chains in the network. This term opposes swelling.

- **Ionic pressure (π_i)**: This accounts for the osmotic pressure of ions. In dilute solutions, most counterions reside inside the microgel to maintain electroneutrality. A simplified model is:

$$\frac{\pi_i}{k_B T} = \frac{Q}{\upsilon_p \alpha^3} \tag{2.3}$$

  where Q represents the total charge of the microgel, and υ_p is the volume of the unswollen microgel.

At equilibrium in dilute conditions, these pressures balance:

$$\pi = \pi_m + \pi_{el} + \pi_i = 0. \tag{2.4}$$

Bouhid de aguiar et al. introduced an extension to the classical description of Flory-Rehner, incorporating non-ideal chain elasticity at high swelling ratio[44]. The osmotic pressure within a microgel particle results from two opposing terms. The first is a mixing term, describing the mixing entropy and the enthalpy of solvent-monomer interactions, which promotes swelling. The mixing pressure is balanced by the elasticity of the chain segments between crosslinks.

Scotti et al.[38] provide further insights into these complexities, demonstrating that osmotic pressure is substantially affected by counterion concentration, particularly at

high concentrations where non-ideality becomes significant. Their membrane osmometry and dialysis experiments revealed that osmotic pressure is primarily governed by free ions escaping the microgel perimeter. Their model, which balances osmotic pressure terms with microgel bulk modulus to predict deswelling, shows a weak dependence on microgel size. The onset of deswelling is influenced by multiple factors, including microgel crosslinking density, interactions with the surrounding medium, and the osmotic pressure gradient. At even high microgel concentrations, significant mechanical interactions between particles set in, determining faceting and compression [44].

2.1.3 Computational model for solubility prediction

Predicting solvent solubility, particularly for complex polymers like Carbopol, involves numerous factors, including polymer architecture, crosslink density, and the inherent polyelectrolyte nature of the polymer backbone. Such complexity makes accurate solubility prediction a non-trivial endeavor. While no universally reliable method exists to handle every intricacy, the COnductor-like Screening MOdel for Realistic Solvation (COSMO-RS) has emerged as a promising approach for capturing essential solvation phenomena [45,46]. Its efficiency and reliability in predicting solubility across diverse solvent systems make it a suitable computational tool for exploring Carbopol's solubility behavior and guiding solvent selection.

COSMO

The COnductor-like Screening MOdel (COSMO) is the quantum chemical continuum solvation framework upon which COSMO-RS is built. In COSMO, the solvent is represented as a polarizable dielectric continuum rather than a collection of explicit solvent molecules. The solute molecule is placed in a cavity defined by overlapping atomic spheres, and the interaction between solute and solvent is evaluated by solving the Poisson equation with a conductor-like boundary condition. This boundary condition simplifies the treatment of solute-solvent electrostatic interactions, greatly reducing computational cost compared to more explicit continuum solvation methods.

The result of a COSMO calculation is a distribution of surface charges on the solute cavity (often referred to as the COSMO surface). This distribution reflects how the solute is polarized in the presence of the dielectric continuum. The surface charges are then collected into the so-called σ-profile, describing the charge density distribution over the solute surface.

COSMO-RS

COSMO-RS (COnductor-like Screening MOdel for Real Solvents) combines COSMO's quantum chemical foundation with statistical thermodynamics to predict the thermodynamic properties of liquid mixtures (Fig. 2.2) [45–48]. At the heart of COSMO-RS is the use of the surface charge density distribution (σ-profile) generated by the COSMO calculation. This σ-profile effectively encapsulates how a molecule interacts with its environment, capturing both electrostatic and non-electrostatic contributions (e.g., hydrogen bonding and dispersion forces).

By employing a statistical thermodynamic formalism, COSMO-RS evaluates the free energy of mixing based on pairwise interactions of molecular surface segments. These surface segments are classified by their local charge densities, enabling the model to account for complex intermolecular interactions. As a result, COSMO-RS can predict a

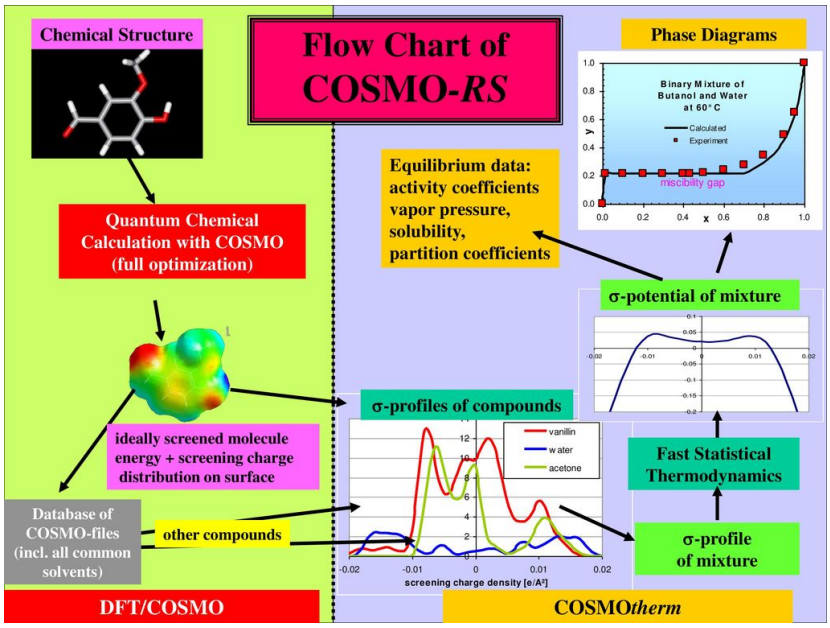

Figure 2.2: Flowchart depicting the computational steps within the COSMO-RS model, from input parameters to final property prediction[47].

range of thermodynamic properties relevant to solubility, including activity coefficients, partition coefficients and phase equilibria.

Unlike Hansen solubility parameter methods[49], which rely on group contribution concepts and can be less accurate for large, complex molecules, COSMO-RS offers an *a priori* predictive capability for a wide range of compounds, including polymers, relying solely on their molecular structures[50]. The element-specific parameterization in COSMO-RS further enhances its versatility: once the model is parameterized for a given element, no additional calibration is required when new molecules containing that element are introduced[51]. This feature is particularly advantageous in screening a large chemical space or investigating novel solvent systems.

Key advantages of COSMO-RS for solubility prediction include:

- **A priori prediction**: No experimental data are required beyond the molecular structure.
- **Applicability to complex molecules and mixtures**: The continuum approach and statistical treatment allow for modeling of polymers, ionic liquids, and other complex systems.
- **Computational efficiency**: Compared to explicit solvation approaches, COSMO-RS is relatively fast while retaining high accuracy.
- **Predictive power for a broad range of thermodynamic properties**: It can estimate activity coefficients, phase equilibria, and partition coefficients in addition to solubility.

Despite these strengths, it is important to acknowledge that the accuracy of COSMO-RS is still governed by the underlying model assumptions. For highly crosslinked or

polyelectrolyte polymers such as Carbopol, additional complexities — such as ionization effects, polymer chain entanglements, and potential phase behavior — may introduce discrepancies between computed and experimental results. Consequently, while COSMO-RS provides a powerful first-principles method for solubility ranking and parameter estimation, experimental validation remains essential to verify and refine computational predictions.

2.2 Materials and Methods

Chapter 1 provides a comprehensive overview of the general materials and methods employed throughout this thesis. This section details the specific experimental procedures used in this chapter, especially focusing on the following key aspects: solvent investigation; tuning of osmotic pressure and/or pH and rheological characterization of the resulting systems; estimates of microgel size from DLS or microscopy approaches.

2.2.1 Carbopol dispersibility in various solvents

The inherent dispersibility of C971 NF in various solvents, in the absence of a neutralizer, was investigated by adding Carbopol powder, corresponding to 0.5 to 1 % in weight fraction, and mixing in the vortex mixer for several hours, as for the preparation protocol discussed in Chapter 1. Sample observation after 24 hours allowed to detect whether the powder was fully dispersed, remained as aggregates, or settled.

The influence of neutralizer addition on C971 NF dispersibility was tested in water and several non-aqueous solvents.

A Mettler Toledo Sevencompact S220 pH/Ion meter provided precise pH values for aqueous samples, prepared as described in Chapter 1. Instead, fine-tuning neutralizer concentration in non-aqueous media presented a challenge due to the limitations of pH measurements. Whatman® indicator papers (WHA2613991, Colour Bonded, 0.0–14.0 range) provided a semi-quantitative measure of pH, with colorimetric responses compared against the manufacturer's color chart. The reliability and consistency of the estimates for PG and Glycerol were validated with titrations with known amounts of NaOH.

Sodium hydroxide (NaOH) or triethylamine (TEA) were used. NaOH was added in both aqueous and non-aqueous samples, while TEA was added only in aqueous samples. Aliquots of the stock solutions were added to the C971 NF dispersions to achieve the desired final concentrations. For non-aqueous samples, solid NaOH was added directly to the solvent to prepare 1 M solutions. These solutions were then added to the C971 NF dispersions to achieve neutralization. The amount of neutralizer added was recorded for all samples.

To determine how prior neutralization with NaOH affects the subsequent dispersibility in non-aqueous, aprotic solvents, aqueous samples of C971 NF 2% were neutralized with NaOH and then lyophilized, resulting in a dry powder mixture of C971 NF and NaOH. This powder was then added to DMSO and DMF but failed to get dispersed, while it could be dispersed in water again.

2.2.2 Tuning of osmotic pressure

To investigate the degree of expansion or contraction of Carbopol suspensions when exposed to different osmotic pressures, Thermo Scientific™ Slide-A-Lyzer™ MINI dialyzers (3.5 kDa MWCO) were employed. To measure the *free expansion*, i.e., the maximum equilibrium swelling of the microgels under zero osmotic pressure, the following procedure was used:

1. **Initial Weighing:** Empty dialysis tubes were weighed to obtain a reference mass.
2. **Sample Loading:** Approximately 0.2 mL of aqueous C971 NF suspensions at different concentrations (1, 0.5, 0.4, and 0.2 wt%) was introduced into each dialysis tube. The loaded tubes were reweighed to accurately determine the initial sample mass.
3. **Dialysis Setup:** The filled tubes were carefully placed in 50 mL vials containing Milli-Q water. This relatively large volume of water was used to ensure negligible pH changes over the course of the experiment. The vials were sealed to prevent evaporation.
4. **Equilibration Period:** The vials were stored at a constant temperature for at least 45 days to allow the system to reach equilibrium swelling.
5. **Final Weighing and Data Collection:** After equilibration, the dialysis tubes were removed, briefly blotted to remove any excess liquid on their surfaces, and reweighed. From the mass change, the final concentration of the Carbopol suspensions within the tubes was calculated (see Figure 2.3).

Throughout these experiments, the sample's pH was checked before and after expansion, and remained unchanged. Furthermore, using neutralized water rather than Milli-Q water did not affect the degree of expansion.

The same procedure was repeated for 1 wt% C971 NF suspensions in PG and DMSO, with the dialysis carried out against their respective pure solvents. This approach allowed the determination of the equilibrium swelling ratio for each sample, providing direct insight into the extent of Carbopol expansion or contraction under zero osmotic pressure.

To tune the osmotic pressure, microgel suspensions were placed in contact with aqueous solutions of polyethylene glycol (PEG, with average molecular mass of 8000 Da), a hydrophilic polymer. By varying PEG 8000 concentration, we can precisely control the osmotic pressure across the semipermeable membrane, following established methods[52], as plotted in Figure 2.4. As in the free expansion procedure, aqueous C971 NF samples (0.2 and 1 wt%) were placed within the dialysis tubes and put in contact with PEG 8000 solutions at different concentrations for at least 45 days.

2.2.3 Rheological characterization

The rheological properties of the various samples (whose preparation was detailed in Chapter 1 were characterized using similar procedures. Each sample underwent a preshear protocol followed by a series of rheological tests. Frequency sweep measurements were performed over a decreasing range of 0.1–100 Hz at a fixed strain of 1% within the linear viscoelastic regime. Large amplitude oscillatory shear (LAOS) measurements were conducted from 0.1% to 300% strain amplitude at a fixed frequency of 1 Hz, and

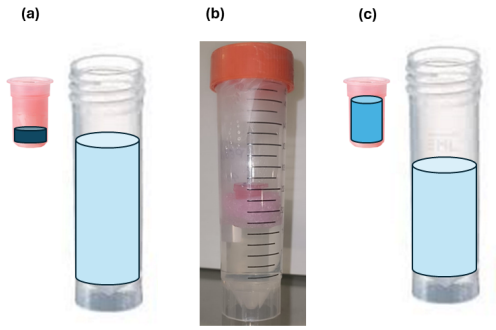

Figure 2.3: Schematic of osmotic experiments, (a): sample and solution bath before test (b): sample kept for 45 days at room temperature while they were sealed, (c): sample and solution bath after 45 days

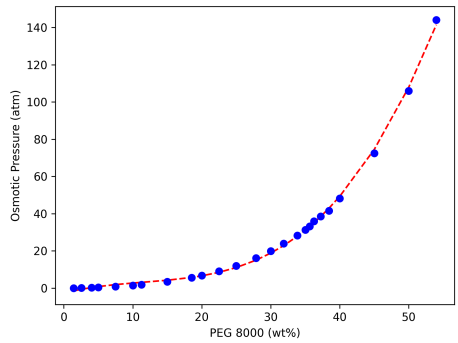

Figure 2.4: Plots of osmotic pressure vs. PEG 8000 weight percentage at 22 °C [52].

flow curve measurements were performed over a shear rate range of 0.01–100 $s^{-}1$ (the 0.01-0.1 range was often discarded because of slip onset). To ensure data reliability, several rheological experiments were repeated at least twice; the reproducibility of the data points was consistently within 2%.

Figure 2.5 shows a representative flow curve for various concentrations of C971 NF in neutralized water.

In frequency sweep tests (see Figure 2.6), the low-frequency value of the storage modulus G was used as an estimate for the 0-frequency modulus G_0 and its dependence on concentration or pH was compared to yield stress dependence.

The yield stress (σ_y) was determined from TC model fitting. An alternative way involves large amplitude oscillations: identifying the onset of nonlinearity in the storage modulus, a deviation from the small-strain linear viscoelastic region, and the following stages can provide access to σ_y. However, this transition is often gradual, hindering precise critical strain determination [53,54]. A practical approach involves the horizontal line representing the behavior of G' well below the yielding point with the power-law equation representing the behavior of G' well above the yielding point. The intersection point of these lines, shown as orange circles in Figure 2.7, can be considered an

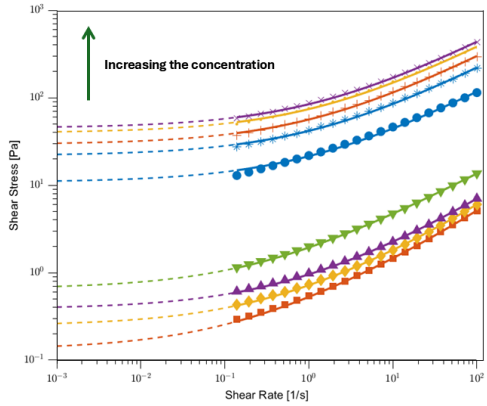

Figure 2.5: Flow Curve Measurements of C971 NF. Fitting with the TC Model. The graph uses the following markers for different weight percentages: Red Square (0.2 wt%), Yellow Diamond (0.3 wt%), Purple Triangle (0.4 wt%), Green Inverted Triangle (0.5 wt%), Blue Circle (1 wt%), Blue Star (2 wt%), Orange Cross (3 wt%), Yellow Dot (4 wt%), and Purple Crooked Cross (5 wt%).

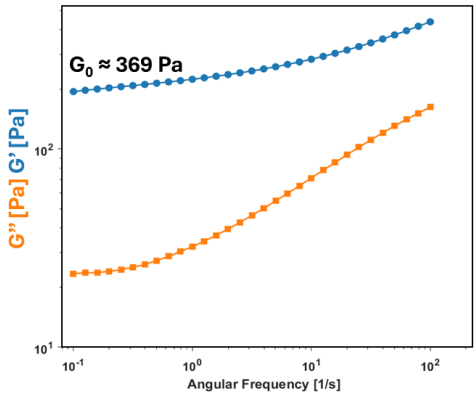

Figure 2.6: Frequency sweep data for C971 NF (5 wt%). The low-frequency storage modulus (G, blue circles) provides an estimate of the zero-frequency modulus ($G_0 \approx 369$ Pa), demonstrating modulus stability below the initial value. Loss modulus (G'', red squares) is also shown.

approximation of the critical strain at which the material transitions to liquid-like behavior[55,56]. The corresponding stress value provides an estimate for σ_y. On the other hand, the second approach based on this test is the intersection of G′ and G″ (shown as a blue circle), which tends to overestimate σ_y. A more unambiguous approach involves analyzing the full σ-γ response in LAOS, with two different power-law regimes clearly emerging in both the low-strain linear viscoelastic region and the high-strain nonlinear region (Figure 2.8). The intersection point can be used to define yield strain and stress.

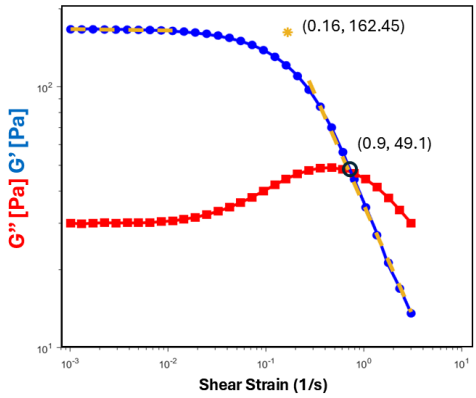

Figure 2.7: Results of large amplitude oscillatory shear measurements for C971 NF 5 wt%. The storage modulus (G') and loss modulus (G'') are plotted as functions of shear strain (γ). Blue circles correspond to G', while red squares correspond to G''. The orange dashed lines represent power-law fits of the behavior well above the yield point, with the intersection of these fits and the horizontal line through the linear G' data indicated by the orange circles. The dark blue empty circle represents the intersection of G' and G''.

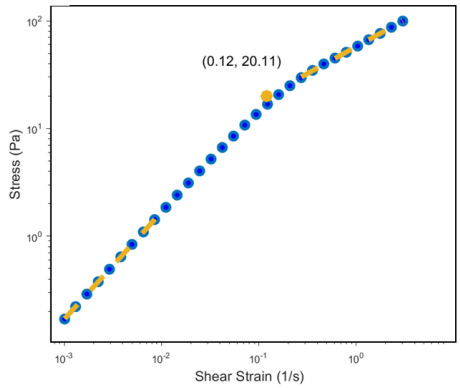

Figure 2.8: Results of large amplitude oscillatory shear measurements for C971 NF 5 wt%. The stress (σ) is plotted as a function of shear strain (γ). The orange dashed lines are power-law fits of the behavior well above and well below the yielding point, whose intersection is shown by the orange circle.

2.2.4 Dynamic Light Scattering

DLS was used to estimate the hydrodynamic size of diluted microgels dispersed in various media. To optimize measurement accuracy and minimize the influence of aggregates, a systematic preparation protocol and investigation of the effect of microgel concentration were undertaken.

Several microgel concentrations were tested to identify the optimal range for DLS analysis. To remove larger aggregates, samples were subjected to centrifugation. The centrifugation speed was carefully optimized; excessively high speeds resulted in com-

plete sedimentation of all particles, while insufficient speeds failed to adequately remove aggregates. As a compromise, 0.025 wt% was chosen for all samples, and the tests were conducted using neutralized water, PG, DMSO, and DMF microgels. The required centrifugation speed and time were found to be strongly dependent on the sample viscosity. Consequently, all samples except the PG (whose viscosity is about 50 times that of other solvents) were centrifuged at 3500 RPM for 1 hour, while the PG samples were centrifuged at 3500 RPM for 50 hours.

The DLS measurements were performed on a ST100 SciTech Instruments apparatus, equipped with a solid-state Nd:YAG laser operating at a doubled continuous wavelength of 532 nm. The laser intensity was controlled using the combination of a half-wave plate, rotating the light polarization, a polarization-maintaining optical fiber, and a Glan-Thompson polariser that set the incident light polarization as vertical.

Scattered light was collected at a 90-degree angle using a multimode fiber coupled to a vertical polarizer. The collected light was split and detected by two photomultiplier tubes (PMTs). The PMT signals were processed using a digital correlator (Flex-03D, correlator.com) to obtain the intensity pseudo-autocorrelation function, $g_2(q,t)$. Data acquisition and analysis were performed using a custom LabVIEW (National Instruments) program.

To ensure consistent experimental conditions, the temperature was maintained at 22 °C using a water bath. Samples were contained in either quartz square cuvettes or round glass vials immersed in the water bath to optimize thermal stability and minimize refractive index mismatch. For individual measurements, samples were loaded into flame-sealed cylindrical borosilicate glass capillaries (outer diameter: 3 mm; inner diameter: 2.4 mm). Five to ten correlation measurements were acquired for each sample and averaged. Subsequent data analysis was performed using custom Python scripts.

Depending on the optimized centrifugation protocol for different solvents, we obtained either bidisperse suspensions (containing distinct smaller and larger particle fractions) or broadly polydisperse Carbopol suspensions. To extract the average microgel sizes from these complex distributions, we fitted the measured correlation functions using either a stretched exponential or a double exponential model. The stretched exponential function, given by Equation 1.31, accurately captures a broad and continuous distribution of particle relaxation times, commonly observed in highly polydisperse or heterogeneous systems.

Figure 2.9 shows the correlation function plotted against lag times for a dilute aqueous Carbopol suspension, with its corresponding stretched exponential fitting.

2.2.5 Optical microscopy

Fluorescence microscopy, which commonly employs dyes or pigments for enhanced visualization[7,57–60], encounters limitations when imaging fully swollen Carbopol microgels. The refractive index of swollen microgels closely matches that of water, resulting in low contrast and hindering observation even with added colorants. While direct visualization of fully swollen microgels is challenging, the addition of a dye can aid in visualizing partially swollen, non-fully neutralized microgels. This approach was implemented by incorporating Rhodamine B into a non-neutralized C971 NF aqueous microgel suspension. Clearly, this approach only provides access to the size and structure of aggregates rather than individual microgels.

A neutralized 0.5 wt% suspension was diluted to 0.01 wt%, and 50 μl was deposited onto a glass slide. Subsequent addition of 10 μl of a 1 mM Rhodamine B solution induced observable changes in the microgel morphology. This dye addition lowered the

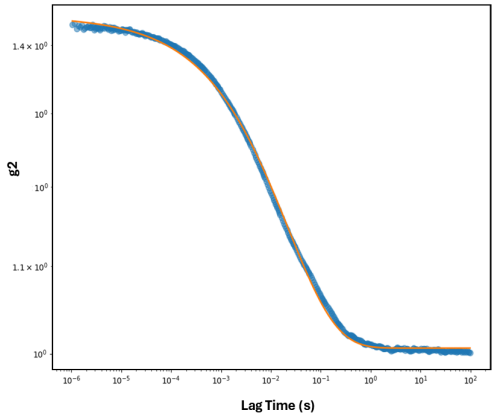

Figure 2.9: Correlation function versus lag time with corresponding stretched exponential fit for Carbopol in water (0.025 wt%). The stretching exponent β=0.42.

pH (to approximately pH 4), leading to a decrease in microgel swelling and increased aggregation. Similar experiments were conducted with PG and DMSO solvents, in which Rhodamin B was found to be soluble; however, no microgels were visible under these conditions, suggesting that microgels do not shrink nor aggregate upon addition of Rhodamin B in these solvents.

2.2.6 Particle tracking for microgels size measurement

To obtain an independent, qualitative assessment of microgel size and aggregate structure, the micro-rheo-mapping approach (later discussed in Chapter 4) was employed. Neutralized water and PG and DMSO samples were selected. For each sample, a concentration about 1.5 times above the corresponding critical concentration for onset of yield stress was used: 0.11 wt% for neutralized water, 1.1 wt% for neutralized PG, and 0.45 wt% for DMSO. Monodisperse carboxylated polystyrene (PS-COOH-B1477) tracer particles (diameter 0.816 ± 0.005 μm; 5% w/v aqueous suspension) were added to each sample to achieve a final tracer concentration of 0.01 wt%. Subsequently, 50 μl of each sample was placed between two glass slides under a microscope, allowing the sample to spread. After a 30-second equilibration period to allow for dissipation of initial sample inhomogeneities, a video was recorded and analyzed according to the methodology described in Chapter 4. This analysis provided semi-quantitative information on microgel aggregate size and distribution.

2.3 Results

2.3.1 Aqueous microgel suspensions

Neutralization and tuning of osmotic pressure

The influence of pH on the C971 NF microgels behavior was first investigated through a series of experiments addressing the effect of neutralizer type and amount on the swelling degree. Figure 2.10 shows titration curves obtained by adding a neutralizer (NaOH) to C971 dispersions at two different concentrations. The curves display a char-

acteristic triphasic profile, consistent with previously reported findings[3,16,61]. Initially, a gradual pH increase occurs as NaOH is added, reflecting the deprotonation of Carbopol monomers. This is followed by a region centered around pH 7 with a sharp pH increase with minimal neutralizer addition, indicating high sensitivity to charge changes as neutralization nears completion; nearly all monomers are compensated for the addition of every acid or base unit directly affecting the pH value. Finally, the curve transitions to a region of reduced slope, reflecting the protonation of Carbopol monomer at higher base concentrations.

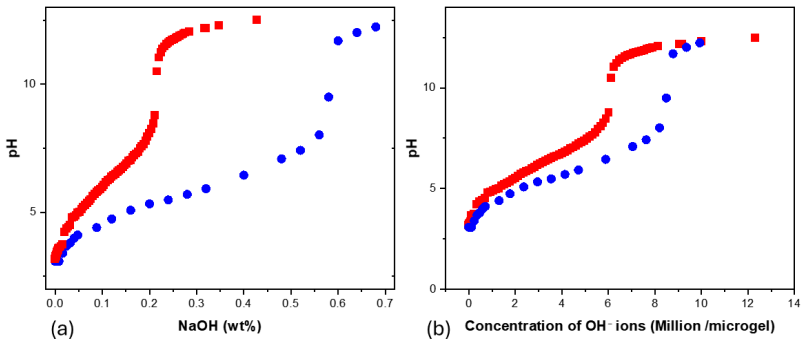

Figure 2.10: pH measurements as a function of (a) added NaOH (wt%) and (b) the number of hydroxide ions (OH^-) (millions) per microgel unit, for 0.5 wt% (red squares) and 1 wt% (blue circles) C971NF dispersions.

When adding NaOH, Sodium ions are introduced in solution, which may affect the overall behavior. To assess the impact of the neutralizer type and examine the influence of salt rather than only evaluating the pH, triethylamine (TEA), a base from a distinct chemical family, was also employed. The resulting pH vs. molarity plot (Figure 2.11) shows remarkable consistency between the two neutralizers, indicating that the type of base has a negligible impact on the overall pH response.

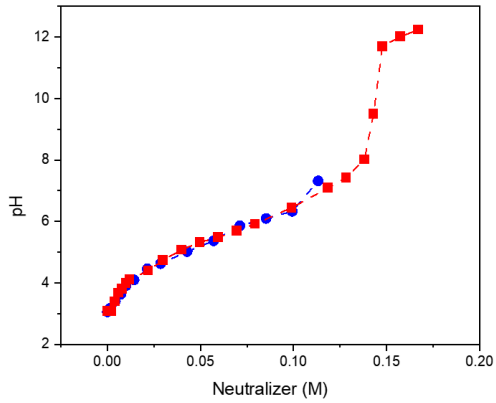

Figure 2.11: Comparison of pH response in 1 wt% C971 NF dispersions using NaOH (red squares) and TEA (blue circles).

At pH 7, we further explored the extent of microgel swelling, by tuning osmotic pressure from zero to very high values and assessing the resulting regimes of microgel concentration.

Free expansion Free expansion experiments, ideally reaching the maximum possible swelling of each single microgel present in the solution, also provide a simple yet effective method for determining the critical concentration of microgels for the onset of yield stress properties (see below). Indeed, Figure 2.12 presents the results of such experiments conducted in neutralized, water-based samples: whatever the initial concentration, the microgel suspension reaches a common final equilibrium concentration, corresponding to full volume occupancy of swollen microgels.

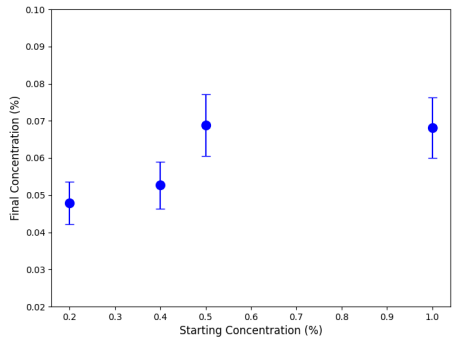

Figure 2.12: Free expansion of C971NF microgels in neutralized water after 45 days. The initial concentrations versus final concentration showed that all concentrations converge towards approximately 0.06 wt%.

Regulation of swelling and concentration through osmotic pressure By tuning the osmotic pressure, we can induce swelling or deswelling of microgels, even reaching a significant packing, which was assessed by comparing relative changes in concentration. Experiments involved exposing neutralized C971NF aqueous suspensions at a certain initial concentration to various osmotic pressure values, by using different concentrations of PEG 8000 (Fig. 2.4), and determining their final equilibrium microgel concentration.

At low to moderate osmotic pressures, the suspensions can undergo expansion, while high enough osmotic pressures (around 30 wt% PEG 8000 for 1 wt% C971NF) result in higher final concentrations, corresponding to microgel shrinking.

The correspondence between osmotic pressure and microgel equilibrium concentration is summarized in Figure 2.13. Two distinct phases are evident: an initial region of slow concentration increase (up to approximately 20 atm), followed by a sharp increase. This biphasic behavior can be explained by considering the microgel response to osmotic pressure in relation to its bulk modulus[38]:

- **Low Osmotic Pressures:** The pressure exerted by counterions leaving the microgel periphery is less than the bulk modulus. The microgel maintains its swollen volume (v_0) due to sufficient internal pressure to balance the external pressure. This represents ideal swelling.

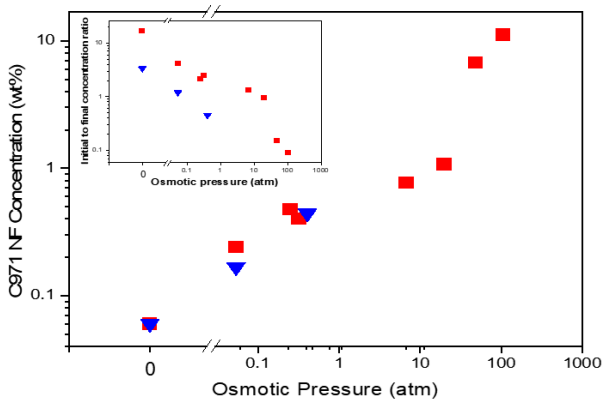

Figure 2.13: Final C971NF suspension concentration (wt%) as a function of osmotic pressure (atm). A biphasic response is observed, characterized by an initial slow increase in concentration followed by a rapid increase above ∼20 atm. Data points represent suspensions with initial concentrations of 1 wt% (red squares) and 0.2 wt% (blue inverted triangles). Inset: Relative degree of swelling, expressed as the ratio of initial to final concentration, plotted against osmotic pressure. Symbols correspond to the same initial concentrations as the main plot.

- **High Osmotic Pressures:** As osmotic pressure exceeds bulk modulus, the external pressure overcomes the internal forces maintaining the swollen state. The microgel gets compressed, initially through shape changes (faceting), and subsequently by deswelling (volume reduction). This marks the transition from ideal to non-ideal swelling. The exact pressure at which this occurs depends weakly on microgel size and crosslinker concentration, factors influencing bulk modulus[38].

Onset and growth of yield stress

The rheological behavior of concentrated Carbopol 971 NF dispersions, where particle packing is significant, is characteristic of soft glassy materials[2,4,62], defined macroscopically by the presence of a yield stress. Using the three-component TC model which is detailed in the chapter 1[63] and systematically varying Carbopol concentration across a wide range under both neutralized and non-neutralized conditions, reveals a characteristic rheological response as illustrated in Figure 2.14: σ_y only appears above a critical mass concentration, at which microgels start to significantly overlap, and approaches a plateau value through two main regimes.

As mentioned in chapter 1, alternative approaches to the estimate of yield stress are available, e.g. based on large amplitude oscillatory tests. The resulting values, reported in Figure 2.15, display a very similar behavior to flow curve data, although they are slightly different. Additionally, this approach allowed for the extraction of the yield strain values, as illustrated in Figure 2.15.

Yet another quantity, the low-frequency plateau modulus, $G - 0$, associated to the elastic properties of the suspensions and derived from frequency sweep measurements, displays a similar concentration dependence, as shown in Figure 2.16 for both neutralized and non-neutralized aqueous suspensions.

To describe the onset and growth of a stress-bearing network (we'll use, in the following, the yield stress values from flow curves), we can utilize a power-law model[64]:

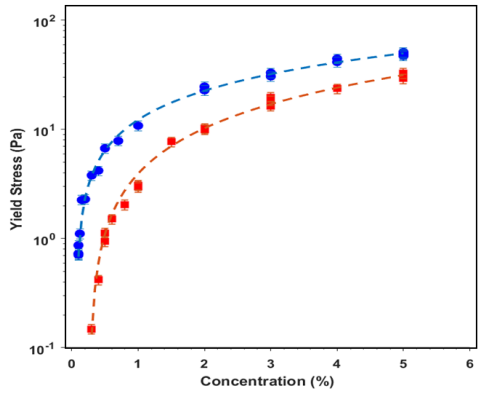

Figure 2.14: Yield stress values determined using the TC model for aqueous dispersions at varying concentrations. Data points represent neutralized (blue circles) and non-neutralized (red squares) samples. Dashed lines show power-law fits to the data according to Equation 2.5.

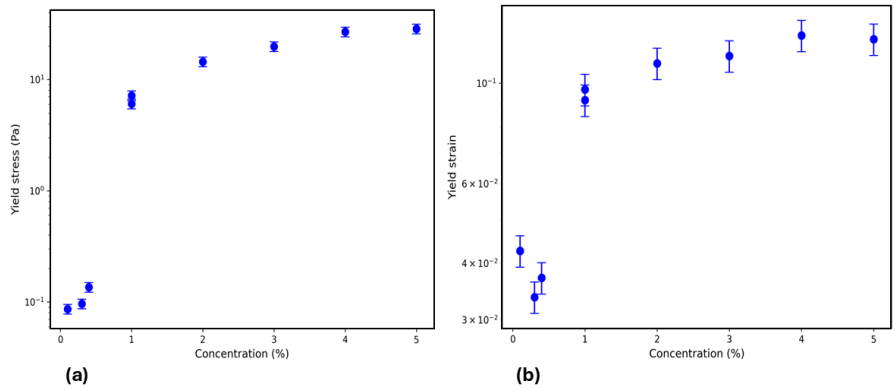

Figure 2.15: (a): Yield stress of neutralized aqueous dispersions as a function of concentration (b): Yield strain (critical strain) of neutralized aqueous dispersions as a function of concentration (determined via amplitude sweep).

$$\sigma_y = A[C - C_t]^B \tag{2.5}$$

where C is Carbopol concentration and C_t is the critical concentration at which the yield stress becomes measurable. This represents the concentration threshold where a continuous stress-bearing network structure begins to form, corresponding to full volume occupancy of microgels, which behave as soft spheres in their swollen state at neutral to basic pH values. A and B are fitting parameters reflecting the system's inherent properties and the nature of interparticle interactions. In particular, the B exponent reflects the efficiency of network formation and the sensitivity of the yield stress to changes in concentration. Fitting this model to the experimental yield stress data allows for quantitative determination of B, and C_t. These parameters provide valuable insights into the magnitude and concentration dependence of the yield stress. Specifically, two main regimes are observed:

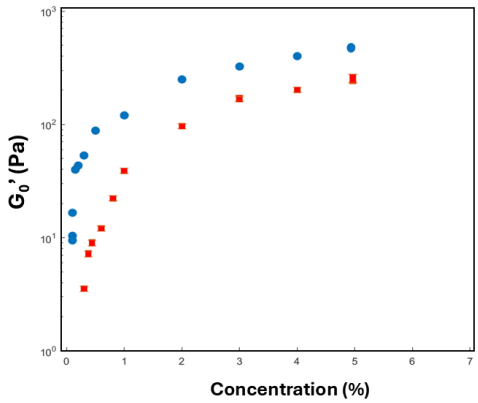

Figure 2.16: G_0 values obtained from frequency sweep tests of aqueous dispersions at varying concentrations. Data points represent neutralized (blue circles) and non-neutralized (red squares) samples.

- **Onset of stress-bearing network:** A steep increase in yield stress above a critical concentration (C_t) is observed. This marks the transition from a semi-dilute regime where individual microgels exert primarily steric repulsion of the shells to a regime where particle interactions begin to dominate[64]. Analysis of C_t reveals information about the system's microstructure: a lower C_t indicates a higher degree of swelling but can also be affected by aggregation phenomena. The degree of cross-linking significantly impacts the mechanical properties of microgels and also the onset of yield stress. Highly cross-linked microgels swell less and, therefore, display, in general, higher C_t values while reaching higher yield stress values than their uncross-linked counterparts[29]. However, throughout this work, the same Carbopol 971 NF samples were investigated, which allows us to explore the role of different neutralization states and solvents on swelling.

- **Slow growth:** Beyond the first regime, the yield stress exhibits a progressively slower increase with increasing concentration, approaching a plateau at high concentrations. This behavior is indicative of denser packing and compression of the microgels[64]. The values of the B exponent can provide an indication of the degree of interpenetration and compaction of the microgels.

pH effect on rheological properties

As reported in Figure 2.14, we observe the onset and growth of yield stress even in the absence of neutralization, albeit at significantly higher microgel concentrations. Therefore, we systematically investigated how the neutralization state affects the mechanical properties of Carbopol microgels. Specifically, we measured flow curves at various microgel concentrations while systematically varying the amount of neutralizer, thus altering the pH.

As shown in Figure 2.17, the yield stress exhibits a nonmonotonic, bell-shaped dependence on pH, reaching maximum values around neutral conditions (pH = 7). This behavior arises from competing physicochemical factors influencing microgel particle interactions, specifically particle swelling, electrostatic repulsion, ionic screening, and

microgel deformability[16].

At low pH values, the microgel particles are highly protonated, rendering them relatively compact due to limited electrostatic repulsion. Although the compact structure facilitates tighter particle packing, the diminished repulsive forces limit the rigidity and connectivity of the particle network, resulting in lower yield stress[17–22].

As pH increases to moderate values (approaching neutrality), enhanced deprotonation significantly increases the charge density on the microgel particles (–COO-) groups, substantially increasing electrostatic repulsion and causing the particles to swell. The enlarged, swollen particles occupy greater volumes and create a jammed network structure with reduced free space and increased interparticle friction, consequently maximizing the yield stress[23].

Further increasing the pH into basic conditions introduces additional complexities, including counterion effects and partial deswelling. The presence of excess counterions, notably Na^+, partially screens the electrostatic interactions and can induce the partial collapse of the swollen particles. These effects reduce the overall particle repulsion, loosen the network structure, and lower the interparticle friction, leading to decreased yield stress values at higher pH.

Hence, the observed nonmonotonic yield stress behavior reflects the intricate balance among particle swelling, electrostatic interactions, ionic screening, and structural rearrangements, all of which evolve differently across the examined pH range.

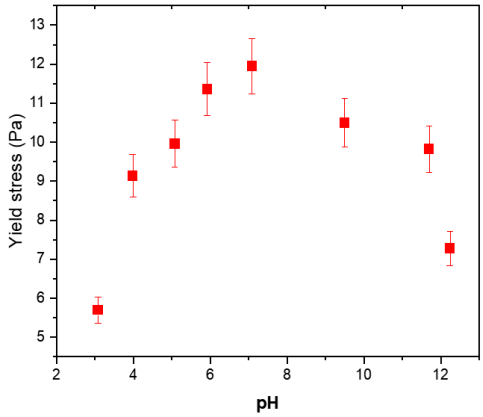

Figure 2.17: Yield stress as a function of pH for C971 NF 1 wt% in water

2.3.2 Non-aqueous microgel suspensions

Based on the observed effects of pH and concentration on the swelling of microgels in aqueous solutions and on their rheological properties, and intrigued by previous reports about the behavior of Carbopol in Glycerol and low-molecular-weight PEG[10], we extended our investigation to a much wider range of solvents.

Investigation of the solvent space

The selection of appropriate solvents for C971 NF dispersion was guided by the fact that, in general, polar solvents like water are expected to be effective for solvating PAA chains and swelling Carbopol microgels. Indeed, its hydrophilic nature, attributed to its

numerous carboxyl groups, facilitates strong interaction with polar solvents, bearing significant partial charges. The associated partial dissociation of the carboxyl groups gives rise to an osmotic pressure gradient that drives water uptake and enhances swelling. Certain organic polar solvents may exhibit an even greater affinity for the Carbopol network than water, thereby promoting internal solvent diffusion even at low degrees of carboxyl group dissociation. Furthermore, the ability of highly polar solvents to form hydrogen bonds with the carboxyl groups can enhance the thermodynamic convenience for the interaction[10,11]. For these reasons, it is useful to map solvents on the basis of their polarity. Because the dielectric constant, a well-established measure of polarity[65,66], is an average value, it easily misses the molecular details. We thus turned to the more complete, yet simple, COSMO-RS computational approach[51], thanks to the courtesy of Prof. Jean-Marie Aubry, as illustrated in section 2.1.3.

Over 160 common solvents were selected to be examined through the COSMO-RS model. The resulting predictions provided a qualitative overview of solvent suitability and formed the basis for further experimental investigation, performed with long equilibration times.

In Figure 2.18 the predicted logarithmic solubility ($\log_{10}(S)$) values from COSMO-RS are plotted against the dielectric constant for several tens of solvents. Such values, showing a broad correlation, clearly identify clusters of solvents with expected C971 NF dispersibility and others with poor predicted dispersibility; however, several solvents present conflicting predictions. Among these lies water, which indeed has various degrees of compatibility with Carbopol depending on pH. We thus experimentally tested Carbopol dispersibility for a significant number of solvents, (See Table 2.1)

The results are presented in Figure 2.18: the green dots represent solvents that can effectively disperse C971NF, the orange dots solvents with intermediate ability (corresponding to stable but turbid solutions) and the red dots solvents that cannot disperse at all. Gray dots denote solvents that have not been experimentally evaluated in this study. The resulting graph reveals four distinct solvent categories:

1. Low $\log_{10}(S)$ and low dielectric constant: These solvents, as expected, failed to disperse C971 NF.

2. High $\log_{10}(S)$ and low dielectric constant: Despite favorable predicted solubility, these solvents also proved ineffective.

3. High $\log_{10}(S)$ and high dielectric constant: Consistent with expectations, many solvents in this group could successfully disperse C971 NF.

4. Low $\log_{10}(S)$ and high dielectric constant: Surprisingly, several solvents within this category effectively dispersed C971 NF, but only in the presence of a neutralizer, a phenomenon detailed later in this chapter.

Based on these results, some of the protic and aprotic solvents demonstrating effective dispersion (besides water, PG, PEG 400, PEG 200, Glycerol, DMSO, and DMF) were selected for further characterization. These solvents were used to prepare C971 NF dispersions at concentrations ranging from 0.05 to 10 wt% for comprehensive analysis.

Neutralizable solvents

The behavior of Carbopol in polar, protic solvents was mainly investigated in PG and Glycerol, to assess the effect of different polarity on swelling properties and structure

Table 2.1: Solvent

Compound	Formula	Molecular Weight (g/mol)	Dielectric Constant
Water	H_2O	18.015	80.10
Dimethylsulfoxide (DMSO)	C_2H_6OS	78.13	46.68
Glycerol	$C_3H_8O_3$	92.09	46.50
Dimethylformamide (DMF)	C_3H_7NO	73.09	36.70
Acetonitrile	C_2H_3N	41.05	36.60
Methanol	CH_3OH	32.04	33.00
N-Methyl-2-pyrrolidone (NMP)	C_5H_7NO	99.15	32.00
Propylene glycol (PG)	C_3H_8O	76.09	32.00
Ethanol	C_2H_5OH	46.07	25.30
Acetone	C_3H_6O	58.08	20.70
2-Propanol	C_3H_8O	60.10	18.30
1-Butanol	$C_4H_{10}O$	74.12	17.80
1-Pentanol	$C_5H_{12}O$	88.15	15.30
1,2-Diaminoethane	$C_2H_8N_2$	60.10	14.20
Polyethylene glycol 400 (PEG 400)	$(C_2H_4O)_n$	380 - 420	14.10
1-Hexanol	$C_6H_{14}O$	102.17	13.30
1-Octanol	$C_8H_{18}O$	130.23	11.70
1-Decanol	$C_{10}H_{22}O$	146.29	9.70
Ethyl acetate	$C_4H_8O_2$	88.11	6.00
Chloroform	$CHCl_3$	119.38	4.80
Toluene	C_7H_8	92.14	2.38
Hexane	C_6H_{14}	86.18	1.89
Polyethylene glycol 200 (PEG 200)	$(C_2H_4O)_n$	190 - 210	-

buildup. Neutralization curves were measured at various C971NF concentrations by dissolving NaOH in PG, finding a qualitatively similar response to aqueous samples, with a steep increase from acidic to basic pH at a specific NaOH concentration, as shown in Figure 2.19.

However, important differences emerge between water and PG dispersions. First, Carbopol itself has a stronger buffering effect in water than in pH, as appreciated from the smaller pH value at 0 added NaOH. Moreover, if we consider the different densities of water and PG and convert both Carbopol and NaOH concentrations in molar units (the molar mass of the Carbopol monomer unit is 72 g/mol according to Lubrizol technical data sheets[67]), we can compare the titration curves expressed in terms of molar ratios. Figure 2.20 presents this molar ratio for both aqueous and PG samples. A linear relationship is observed for both systems, indicating a consistent neutralization stoichiometry. Interestingly, the slope for the aqueous samples is approximately 1, indicating a 1:1 stoichiometry, i.e. that each C971 NF unit requires one NaOH molecule for neutralization. Instead, for PG samples, the very different slope indicates that each C971

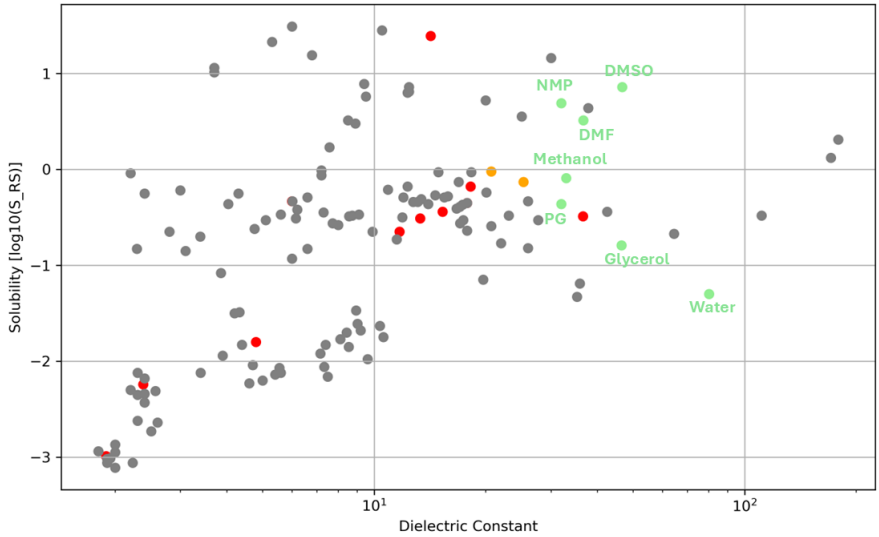

Figure 2.18: Correlation between COSMO-RS predicted $\log_{10}(S)$ and dielectric constant. The markers represent different dispersion categories: light green for well-dispersible, orange for poorly dispersible, red for non-dispersible, and grey for untested.

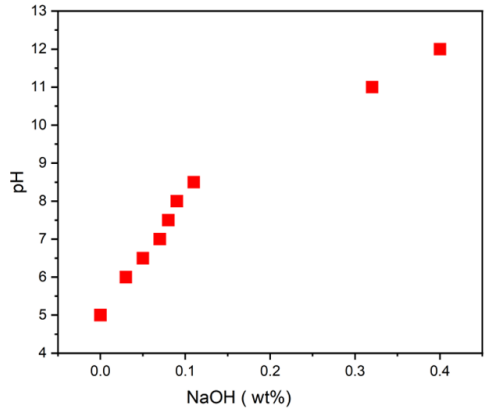

Figure 2.19: pH values of C971 NF dispersions in PG as a function of NaOH concentration. The data points correspond to a Carbopol concentration of 1 wt%. .

NF microgel unit requires approximately 14 monomer units of NaOH molecule for neutralization This distinct neutralization behavior in the non-aqueous environment, likely related to altered solvation and interactions within the microgel network is consistent with the different pKa values of C971 in water versus PG. Overall, fewer charges are switched on in PG, leading to a lower degree of swelling and smaller microgel size, in turn affecting the rheological properties of the dispersion.

As for water-based samples, we investigated the onset and growth of yield stress at increasing Carbopol mass concentration in PG, for acidic and neutral conditions. Once again, we could observe a qualitatively similar behavior but with rather different thresh-

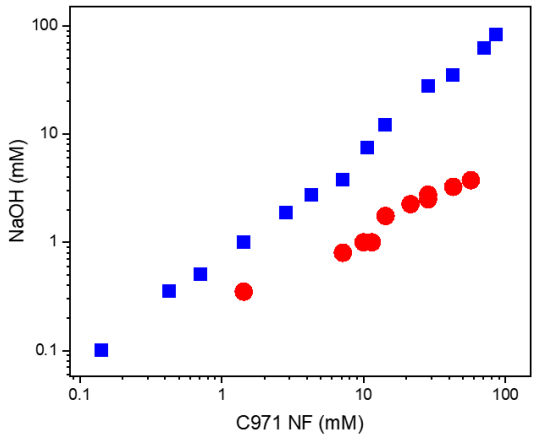

Figure 2.20: Molar ratio of added NaOH to C971 NF in aqueous (blue squares) and propylene glycol (PG) (red circles) suspensions.

old concentration and high-concentration regime, as reported in Figure 2.21, as well as the clear swelling effect of adding NaOH.

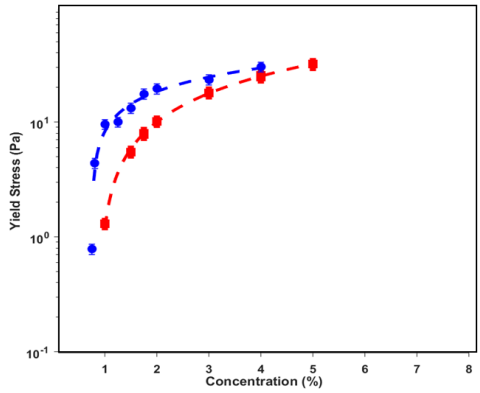

Figure 2.21: Yield stress of PG dispersions as a function of concentration, determined via the TC model. Neutralized samples (blue circles) and non-neutralized samples (red Squares) are shown, along with power-law fits (dashed lines).

We also studied how pH impacts yield stress for given microgel concentrations, as shown in Figure 2.22. A non-monotonic dependence occurs, with peak values, corresponding to the maximum degree of swelling, around pH = 7.

For Glycerol, since strong slip effects during flow curve measurements prevented accurate yield stress determination, the low-frequency limit of storage modulus G' from small amplitude oscillatory measurements was used as an alternative metric for the onset and growth of elastic properties (see Figure 2.23)[55]. Again, qualitatively similar behavior can be observed, but with different values for threshold concentration and ex-

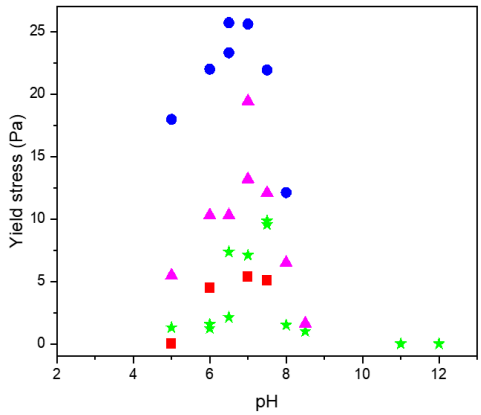

Figure 2.22: Yield stress of C971 NF microgel in PG as a function of pH. Data points represent concentrations of 0.8 wt% (red squares), 1 wt% (green stars), 1.5 wt% (pink rectangles), and 3 wt% (blue circles).

ponent. Moreover, in σ_y vs. pH measurements, the peak value lies around 7, again corresponding to maximum swelling occurring upon neutralization (see Figure 2.24). This is a further confirmation of the fact that Carbopol microgels reach a state of maximum solvation upon pH tuning also in non-aqueous solvents and that rheological measurements can be exploited as a sensitive "mechanical titration" for swelling state.

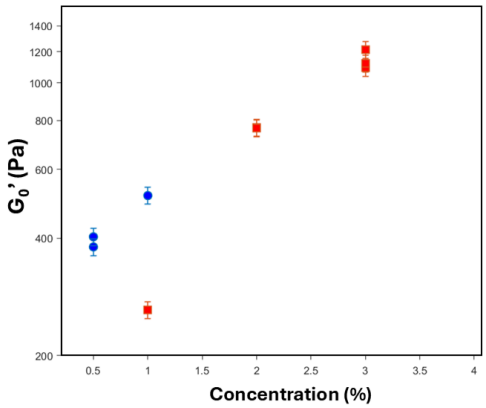

Figure 2.23: Low-frequency storage modulus (G_0') as a function of concentration for neutralized (blue circles) and non-neutralized Glycerol-based C971NF microgels.

Non-neutralizable solvents

Even in the case of aprotic solvents, in which neutralization of microgels is not possible, these can be dispersed providing a yield stress material above a threshold mass concentration, as shown for DMSO and DMF in Figure 2.25. As compared to neutralized aqueous dispersions, the measured threshold concentrations are higher, but the curves

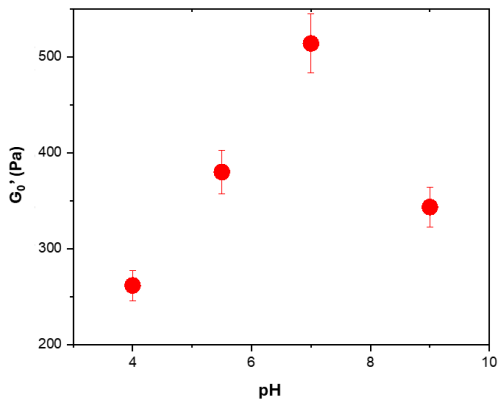

Figure 2.24: Storage modulus as a function of pH (based on pH strips) for C971 NF 1wt% in Glycerol.

reach higher values at large concentrations.

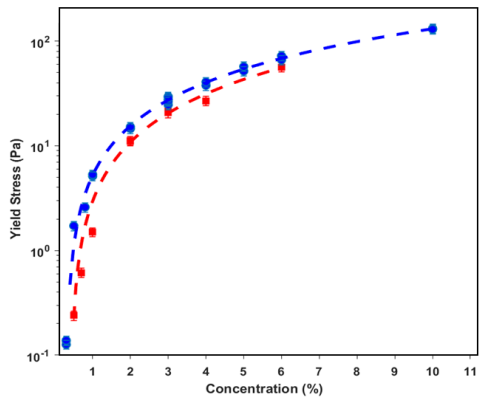

Figure 2.25: Yield stress of DMSO (blue circles) and DMF (red squares) dispersions as a function of concentration, determined via the TC model. Dashed lines represent power-law fits to the data.

Free expansion experiments against zero osmotic pressure allow to independently assess the critical concentration of microgels in various solvents. Figure 2.26 presents the results of such experiments conducted on neutralized water-based, neutralized PG, and DMSO C971NF microgels. Interestingly, the critical concentrations obtained from these free expansion tests exhibit excellent agreement with those derived from fitting yield stress versus concentration data (Figure 2.26) using a power-law model, thus validating the accuracy of these findings. Furthermore, the consistency of final concentrations obtained from free expansion tests in water, initiated at various initial concentrations (Figure 2.12), confirms the reliability of this experimental approach.

2.3.3 Comparison of microgel behavior in water and other solvents

We observed several common features between water-based dispersions and non-aqueous systems at different pH values. Free expansion experiments against zero osmotic pressure allow to independently assess the critical concentration of microgels in various solvents. Figure 2.26 presents the results of such experiments conducted on neutralized water-based, neutralized PG, and DMSO C971NF microgels. These values are in good agreement with those derived from the power-law fit.

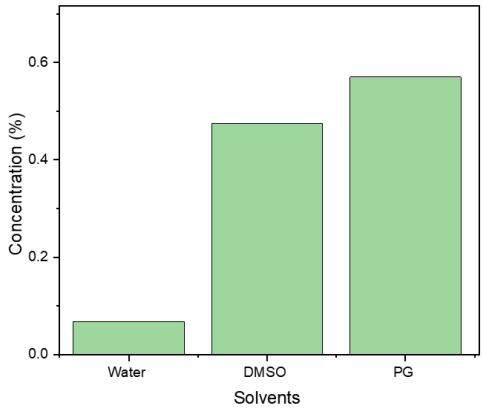

Figure 2.26: Free expansion of 1 wt% initial concentration C971NF microgels in neutralized water, neutralized PG, and DMSO after 45 days. Green bars represent final concentrations (0.062 wt% in neutralized water, 0.57 wt% in neutralized PG, and 0.47 wt% in DMSO).

Scaling of microgel rheological properties

In order to get a unified description of the microgel behavior, we compared the fitting parameters obtained from the power-law model in the various samples. Figure 2.27 presents the critical concentration (C_t) and scaling exponent (B) for each sample. The neutralized aqueous dispersion exhibits the lowest C_t but also a relatively small B, while the non-neutralized aqueous dispersion exhibits both bigger C_t and larger B. Interestingly, dispersions in PG, both neutralized and non-neutralized, exhibit even higher C_t values but lower B compared to the water-based systems. Finally, dispersions in DMSO and DMF are characterized by relatively small C_t values and high exponents. To better compare the curves, Figure 2.28 shows a plot of yield stress vs. the rescaled concentration $C - C_t$ for all samples, providing a more direct visualization of the yield stress growth rate above the critical concentration.

The rheological behavior of microgel dispersions is significantly influenced by solvent conditions and degree of neutralization. These effects primarily stem from a combination of degree of microgel swelling and aggregation.

The role of microgel size

We can estimate the average size of the microgels, or their aggregates, at the onset of yield stress from the critical concentration C_t of Carbopol C971 NF, assuming it to be close to the overlap concentration in a homogeneous dispersion. Using the molar weight

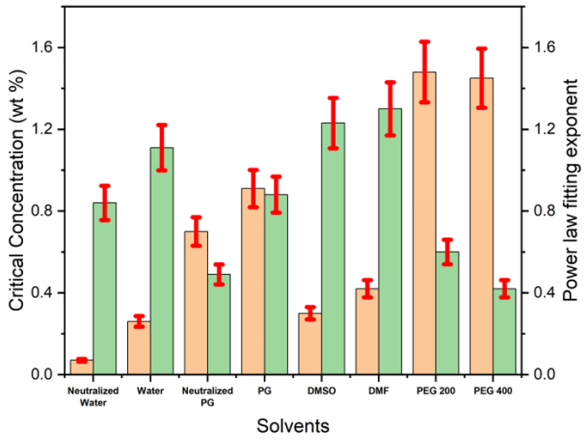

Figure 2.27: Critical concentration and exponent of power-law fitting for various samples. The orange bar represents the critical concentration, while the green bar denotes the exponent of the power-law fitting.

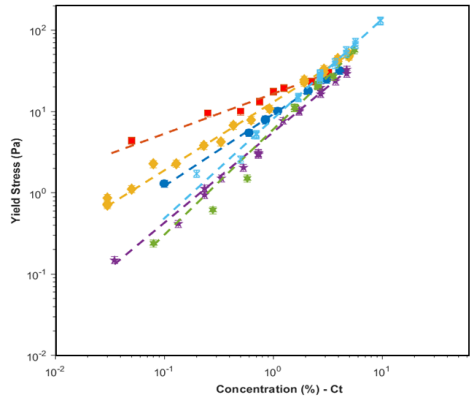

Figure 2.28: Log-log plot of yield stress vs. $C - C_t$ for various samples. This plot illustrates the yield stress growth rate above the critical concentration C_t. Data shown: PG (blue circles), neutralized PG (red squares), neutralized Water (orange diamonds), water (purple stars), DMF (green hexagons), and DMSO (light blue crosses).

of Carbopol 941, reported by Carnali and Naser to be approximately 3300 monomer units (or 237,600 g/mol)[3], which is equivalent to C971 NF data[67], we can estimate the number density of microgels and thus their size.

The radius (r) of a spherical microgel particle can be calculated using the following equation:

$$r = \sqrt[3]{\frac{3N_A m}{4V\rho M_w}} \tag{2.6}$$

where r is in cm, N_A is Avogadro's number (6.022×10^{23} mol^{-1}), m is the mass fraction of Carbopol 941 (wt%), V is the total volume of the microgel suspension (g/cm^3), and M_w is the molar mass of Carbopol 941 (g/mol).

The figure 2.29 reports the so-extracted microgel radius in various solvents and conditions. No published data are available for the size of Carbopol 971 NF microgels. However, considering Carbopol 974 NF as the closest analogue based on Lubrizol reports [21], we find the estimates in literature to closely match our findings for the neutralized water system [5,60,68], thus corroborating the observed differences in other solvents.

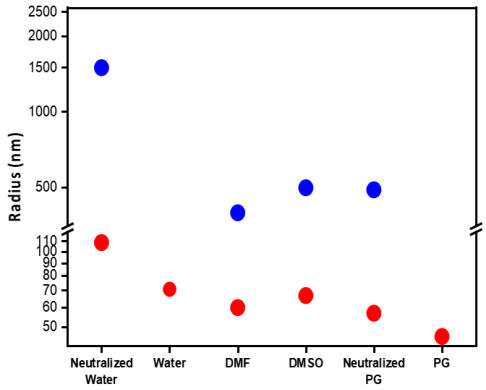

Figure 2.29: Comparison of estimated microgel radius based on critical concentration (C_t) (red circles) and average hydrodynamic radius determined by DLS (blue circles) in various solvents.

Alternatively, we can estimate the typical size of microgels from DLS experiments on diluted samples in the respective solvents (Figure 2.29). In all samples, the measured hydrodynamic radii of diffusing particles are significantly larger than those extracted from threshold concentrations, indicating a non-negligible, persistent contribution from aggregates, despite the careful procedure to minimize their presence. However, the typical size measured in neutralized water, about 2.2 μm, is significantly larger than in other samples, consistent with its critical concentration, the lowest among the measured samples.

We can further compare the size estimates through optical microscopy, either by direct imaging or through particle tracking. Microscopic analysis of non-neutralized aqueous C971 NF microgels revealed round aggregates (Figure 2.30). Size distribution ranged from 1.5 to 4 μm, with an average radius of approximately 2.5 μm. It is noteworthy that dye addition induced the gradual appearance of smaller particles, which subsequently aggregated to form larger structures of microgel aggregates. Indeed, pH increae upon addition of NaOH caused these particles to disappear, confirming that the visualized structures are composed of partially swollen, dye-stained microgels.
This aggregation tendency was not observed in e.g. PG or DMSO, which partially explains the higher homogeneity and lower contrast of microscopy images in these solvents.

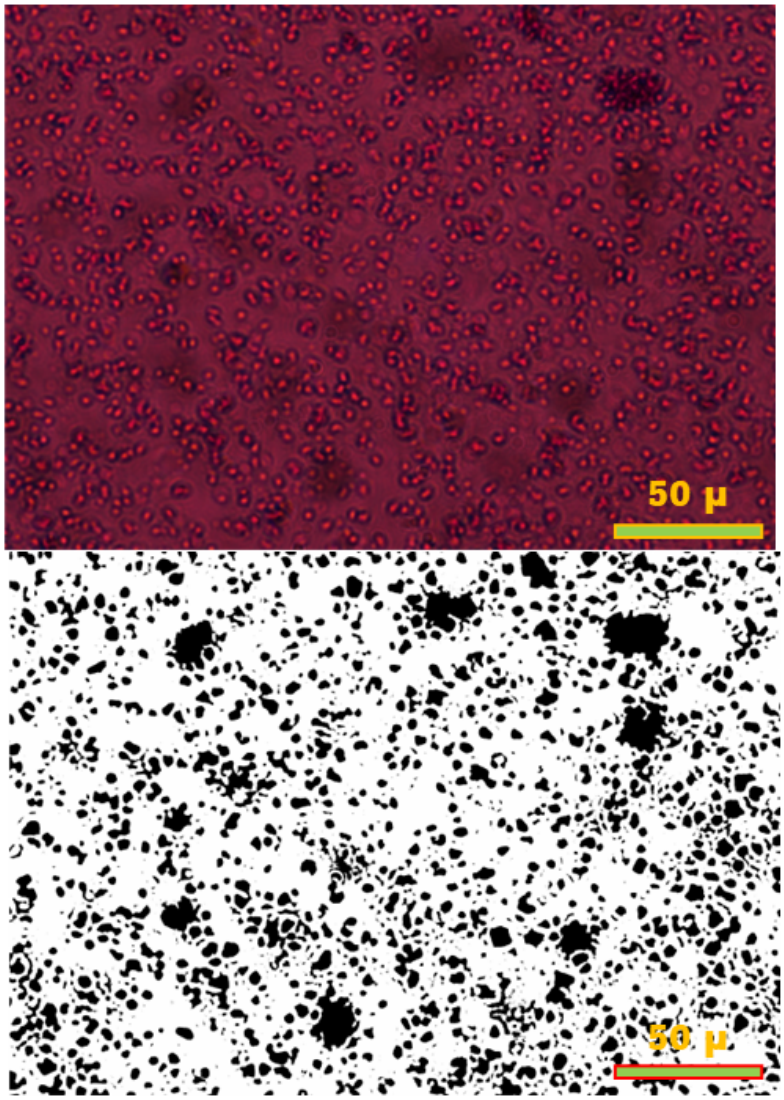

Figure 2.30: Microscopic image of a 50 μL drop of 0.01 wt% C971 NF with 10 μL of 1 mM Rhodamine B added, showing an average aggregate microgel size of approximately 4 μm at pH 4. The raw image (top) is thresholded (bottom) to determine the microgel size distribution.

To characterize the heterogeneity of the samples and the size distribution of microgel clusters in semi-diluted samples, we exploited the approach described in chapter 4, based on tracking the motion of tracers upon application of a weak flow. The resulting heterogeneity maps provided a semi-quantitative assessment of the polydispersity of microgel aggregates on larger scales. Figure 2.31 displays heterogeneity maps for neutralized water, neutralized PG and DMSO samples. In these maps, blue regions represent fluid areas with mobile tracers, red regions are predominantly elastic areas with

immobile tracers, while green regions represent intermediate, viscoelastic or intermittent areas. The extent and spatial distribution of red regions thus provides an estimate of the microgel clusters present in the sample (in the specific conditions of testing).
The water sample exhibited red regions in the 5-20 μm size range and extended green regions. Conversely, PG and Glycerol samples displayed considerably smaller red areas, while the DMSO sample showed larger green areas, somewhat indicative of looser structures. However, the semiquantitative nature of this analysis limits its comparison to other approaches (we provide examples of its fruitful application in chapter 4).

2.4 Conclusions

In this chapter, we have characterized the dispersion of Carbopol microgels in water and several other solvents. We have investigated the effect of pH on the degree of swelling and aggregation of microgels, as well as the dependence of rheological properties on concentration and neutralization state. A strong, non-monotonic pH dependence is found in aqueous dispersions: while non-neutralized dispersions form aggregates and only partially swell, at increasing neutralization negative charges promote more and more significant microgel swelling, which on turn leads to microgel packing and onset of yield stress at lower critical concentrations (C_t). When pH = 7 is exceeded, reduced swelling leads to a drop in yield stress. The state of the building blocks also reflects the power-law dependence of yield stress on concentration: denser microgel aggregates in non-neutralized samples lead to steeper growth, while in fully swollen microgels, interactions among the shells allow smoother growth.
Qualitatively similar behavior is reported for the first time in other solvents, like Propylene Glycol: neutralization promotes swelling and onset of yield stress at lower concentrations, yet higher than for neutral aqueous suspensions. By assessing the size of microgels in dilute and semi-dilute suspensions through various approaches, we find a good correspondence between the degree of swelling and aggregation and the rheology of the samples. However, direct assessment of density profiles of the microgels, through, e.g., SANS, will be necessary to capture the structural and interaction contributions to rheology, from semidilute to fully packed microgels. Finally, some aprotic solvents like DMSO and DMF also prove to be good solvents for Carbopol microgels, despite the impossibility of tuning pH in these solvents. A distinct concentration dependence is found for yield stress in aprotic solvents, with low critical concentration and strong increase with concentration.

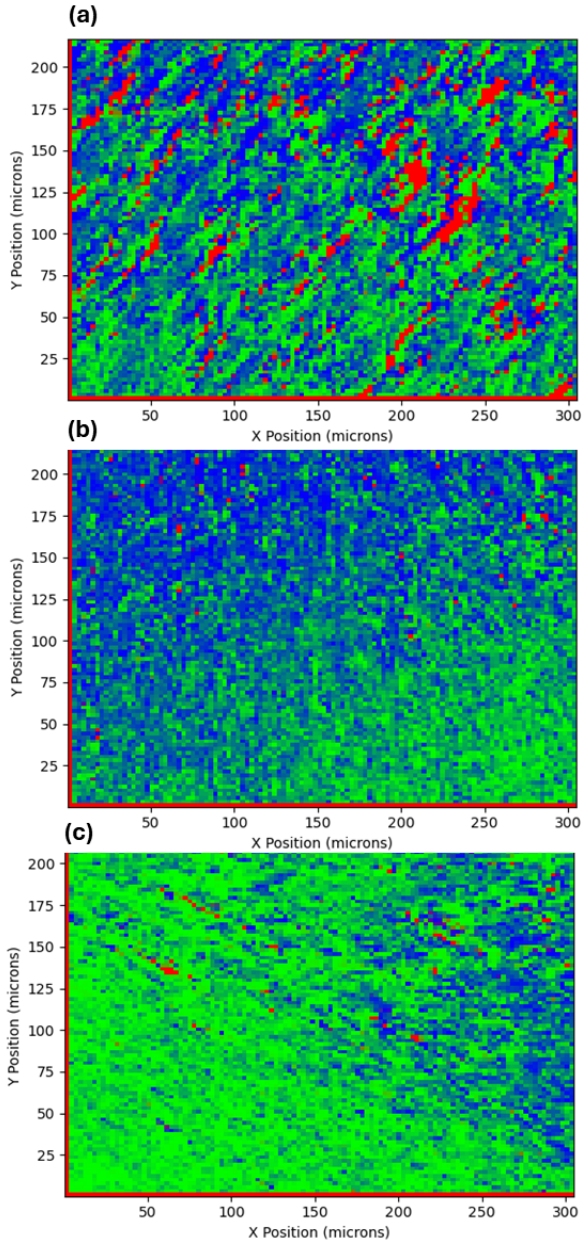

Figure 2.31: Heterogeneity maps for (a): neutralized water , (b): neutralized PG, and (c): DMSO samples.

Bibliography

[1] B. Barry and M. Meyer. The rheological properties of carbopol gels ii. oscillatory properties of carbopol gels. *International Journal of Pharmaceutics*, 2(1):27–40, 1979.

[2] R. Ketz, R. Prud'homme, and W. Graessley. Rheology of concentrated microgel solutions. *Rheologica acta*, 27:531–539, 1988.

[3] J. Carnali and M. Naser. The use of dilute solution viscometry to characterize the network properties of carbopol microgels. *Colloid and Polymer Science*, 270:183–193, 1992.

[4] J.-M. Piau. Carbopol gels: Elastoviscoplastic and slippery glasses made of individual swollen sponges: Meso-and macroscopic properties, constitutive equations and scaling laws. *Journal of non-newtonian fluid mechanics*, 144(1):1–29, 2007.

[5] D. Lee, I. A. Gutowski, A. E. Bailey, L. Rubatat, J. R. de Bruyn, and B. J. Frisken. Investigating the microstructure of a yield-stress fluid by light scattering. *Physical Review E—Statistical, Nonlinear, and Soft Matter Physics*, 83(3):031401, 2011.

[6] T. Bhattacharjee, C. P. Kabb, C. S. O'Bryan, J. M. Urueña, B. S. Sumerlin, W. G. Sawyer, and T. E. Angelini. Polyelectrolyte scaling laws for microgel yielding near jamming. *Soft matter*, 14(9):1559–1570, 2018.

[7] M. Dinkgreve, M. Fazilati, M. Denn, and D. Bonn. Carbopol: From a simple to a thixotropic yield stress fluid. *Journal of Rheology*, 62(3):773–780, 2018.

[8] Z. Jaworski, T. Spychaj, A. Story, and G. Story. Carbomer microgels as model yield-stress fluids. *Reviews in Chemical Engineering*, 38(7):881–919, 2022.

[9] E. Di Giuseppe, F. Corbi, F. Funiciello, A. Massmeyer, T. Santimano, M. Rosenau, and A. Davaille. Characterization of carbopol® hydrogel rheology for experimental tectonics and geodynamics. *Tectonophysics*, 642:29–45, 2015.

[10] S. Migliozzi, G. Meridiano, P. Angeli, and L. Mazzei. Investigation of the swollen state of carbopol molecules in non-aqueous solvents through rheological characterization. *Soft Matter*, 16(42):9799–9815, 2020.

[11] S. Migliozzi, P. Angeli, and L. Mazzei. Gelation kinetics of non-aqueous carbopol

dispersions. *Colloids and Surfaces A: Physicochemical and Engineering Aspects*, 577: 84–95, 2019.

[12] M. A. Zaman, G. P. Martin, G. D. Rees, and P. G. Royall. The effect of hydration on the thermal behaviour of hydrophilic non-aqueous gels stabilised by carbopol 974p. *Thermochimica acta*, 417(2):251–255, 2004.

[13] J. S. Chu, D. M. Yu, G. L. Amidon, N. D. Weiner, and A. H. Goldberg. Viscoelastic properties of polyacrylic acid gels in mixed solvents. *Pharmaceutical research*, 9:1659–1663, 1992.

[14] G. Bonacucina, S. Martelli, and G. F. Palmieri. Rheological, mucoadhesive and release properties of carbopol gels in hydrophilic cosolvents. *International journal of pharmaceutics*, 282(1-2):115–130, 2004.

[15] P. R. Varges, C. M. Costa, B. S. Fonseca, M. F. Naccache, and P. R. de Souza Mendes. Rheological characterization of carbopol® dispersions in water and in water/glycerol solutions. *Fluids*, 4(1):3, 2019.

[16] G. Kocak, C. Tuncer, and V. Bütün. ph-responsive polymers. *Polymer Chemistry*, 8 (1):144–176, 2017.

[17] Lubrizol. Carbopol ultrez 21 polymer. Technical Report 297, Lubrizol Technical Data Sheet, 2002.

[18] Lubrizol. Carbopol ez-3 polymer. a versatile, high efficiency, self-wetting rheology modifier for household and ii applications. Technical Report 735, Lubrizol Technical Data Sheet, 2009.

[19] Lubrizol. Formulating hydroalcoholic gels with carbopol polymers. Technical Report 255, Lubrizol Technical Data Sheet, 2009.

[20] Lubrizol. Neutralizing carbopol and pelumen polymers in aqueous and hydroalcoholic systems. Technical Report 237, Lubrizol Technical Data Sheet, 2009.

[21] Lubrizol. Carbopol etd2623 polymer. an efficient fast hydrating rheology modifier for household and ii applications. Technical Report 732, Lubrizol Technical Data Sheet, 2010.

[22] Lubrizol. Carbopol ez-2 polymer. a high efficiency, self-wetting rheology modifier for home care applications. Technical Report 734, Lubrizol Technical Data Sheet, 2013.

[23] N. Sharmin, M. Al-Mamun, and R.-u. Jalil. A novel method to study the effect of ph and excipients on water uptake and swelling behaviour of carbopol polymers. *Bangl Pharm J*, 3(2):1–7, 2010.

[24] F. K. Oppong and J. R. de Bruyn. Diffusion of microscopic tracer particles in a yield-stress fluid. *J. Non-Newtonian Fluid Mech.*, 142(1-3):104–111, 2007.

[25] F. Oppong and J. De Bruyn. Mircorheology and jamming in a yield-stress fluid. *Rheologica acta*, 50:317–326, 2011.

[26] T. Divoux, D. Tamarii, C. Barentin, and S. Manneville. Transient shear banding in a simple yield stress fluid. *Physical review letters*, 104(20):208301, 2010.

[27] T. Divoux, C. Barentin, and S. Manneville. From stress-induced fluidization processes to herschel-bulkley behaviour in simple yield stress fluids. *Soft Matter*, 7(18): 8409–8418, 2011.

[28] N. J. Balmforth and A. C. Rust. Weakly nonlinear viscoplastic convection. *Journal of Non-Newtonian Fluid Mechanics*, 158(1-3):36–45, 2009.

[29] I. A. Gutowski. The effects of ph and concentration on the rheology of carbopol gels. 2010.

[30] M. Guo and H. M. Wyss. Micromechanics of soft particles. *Macromolecular Materials and Engineering*, 296(3-4):223–229, 2011.

[31] J. Mattsson, H. M. Wyss, A. Fernandez-Nieves, K. Miyazaki, Z. Hu, D. R. Reichman, and D. A. Weitz. Soft colloids make strong glasses. *Nature*, 462(7269):83–86, 2009.

[32] S. P. Meeker, R. T. Bonnecaze, and M. Cloitre. Slip and flow in soft particle pastes. *Physical Review Letters*, 92(19):198302, 2004.

[33] A. Fernández-Nieves, A. Fernández-Barbero, B. Vincent, and F. De Las Nieves. Charge controlled swelling of microgel particles. *Macromolecules*, 33(6):2114–2118, 2000.

[34] K. Han, R. Tiwari, T. Heuser, and A. Walther. Simple platform method for the synthesis of densely functionalized microgels by modification of active ester latex particles. *Macromolecular Rapid Communications*, 37(16):1323–1330, 2016.

[35] B. Sung, C. Kim, and M.-H. Kim. Biodegradable colloidal microgels with tunable thermosensitive volume phase transitions for controllable drug delivery. *Journal of colloid and interface science*, 450:26–33, 2015.

[36] J.-J. Lietor-Santos, B. Sierra-Martin, R. Vavrin, Z. Hu, U. Gasser, and A. Fernandez-Nieves. Deswelling microgel particles using hydrostatic pressure. *Macromolecules*, 42(16):6225–6230, 2009.

[37] C. Pellet and M. Cloitre. The glass and jamming transitions of soft polyelectrolyte microgel suspensions. *Soft matter*, 12(16):3710–3720, 2016.

[38] A. Scotti, M. Pelaez-Fernandez, U. Gasser, and A. Fernandez-Nieves. Osmotic pressure of suspensions comprised of charged microgels. *Physical Review E*, 103(1): 012609, 2021.

[39] P. J. Flory and J. Rehner. Statistical mechanics of cross-linked polymer networks i. rubberlike elasticity. *The journal of chemical physics*, 11(11):512–520, 1943.

[40] P. Van Der Scheer, T. Van De Laar, J. Van Der Gucht, D. Vlassopoulos, and J. Sprakel. Fragility and strength in nanoparticle glasses. *ACS nano*, 11(7):6755–6763, 2017.

[41] P. S. Mohanty, S. Nöjd, K. van Gruijthuijsen, J. J. Crassous, M. Obiols-Rabasa,

R. Schweins, A. Stradner, and P. Schurtenberger. Interpenetration of polymeric microgels at ultrahigh densities. *Scientific Reports*, 7(1):1487, 2017.

[42] G. Romeo, L. Imperiali, J.-W. Kim, A. Fernández-Nieves, and D. A. Weitz. Origin of de-swelling and dynamics of dense ionic microgel suspensions. *The Journal of Chemical Physics*, 136(12), 2012.

[43] A. Fernández-Nieves, A. Fernández-Barbero, B. Vincent, and F. De las Nieves. Osmotic de-swelling of ionic microgel particles. *The Journal of chemical physics*, 119(19): 10383–10388, 2003.

[44] I. Bouhid de Aguiar, T. Van de Laar, M. Meireles, A. Bouchoux, J. Sprakel, and K. Schroën. Deswelling and deformation of microgels in concentrated packings. *Scientific reports*, 7(1):10223, 2017.

[45] A. Klamt and G. Schüürmann. Cosmo: a new approach to dielectric screening in solvents with explicit expressions for the screening energy and its gradient. *Journal of the Chemical Society, Perkin Transactions 2*, (5):799–805, 1993.

[46] A. Klamt. Conductor-like screening model for real solvents: a new approach to the quantitative calculation of solvation phenomena. *The Journal of Physical Chemistry*, 99(7):2224–2235, 1995.

[47] A. Klamt and F. Eckert. Cosmo-rs: a novel and efficient method for the a priori prediction of thermophysical data of liquids. *Fluid Phase Equilibria*, 172(1):43–72, 2000.

[48] F. Eckert and A. Klamt. Fast solvent screening via quantum chemistry: Cosmo-rs approach. *AIChE Journal*, 48(2):369–385, 2002.

[49] C. M. Hansen. *Hansen solubility parameters: a user's handbook*. CRC press, 2007.

[50] A. Benazzouz, L. Moity, C. Pierlot, V. Molinier, and J.-M. Aubry. Hansen approach versus cosmo-rs for predicting the solubility of an organic uv filter in cosmetic solvents. *Colloids and Surfaces A: Physicochemical and Engineering Aspects*, 458:101–109, 2014.

[51] A. Klamt. The cosmo and cosmo-rs solvation models. *Wiley Interdisciplinary Reviews: Computational Molecular Science*, 8(1):e1338, 2018.

[52] C. B. Stanley and H. H. Strey. Measuring osmotic pressure of poly (ethylene glycol) solutions by sedimentation equilibrium ultracentrifugation. *Macromolecules*, 36(18): 6888–6893, 2003.

[53] K. Hyun, M. Wilhelm, C. O. Klein, K. S. Cho, J. G. Nam, K. H. Ahn, S. J. Lee, R. H. Ewoldt, and G. H. McKinley. A review of nonlinear oscillatory shear tests: Analysis and application of large amplitude oscillatory shear (laos). *Progress in polymer science*, 36(12):1697–1753, 2011.

[54] C. Yüce and N. Willenbacher. Challenges in rheological characterization of highly concentrated suspensions—a case study for screen-printing silver pastes. *Journal of visualized experiments: JoVE*, (122):55377, 2017.

[55] F. Rouyer, S. Cohen-Addad, and R. Höhler. Is the yield stress of aqueous foam a well-defined quantity? *Colloids and Surfaces A: Physicochemical and Engineering Aspects*, 263(1-3):111–116, 2005.

[56] M. Dinkgreve, J. Paredes, M. M. Denn, and D. Bonn. On different ways of measuring "the" yield stress. *Journal of non-Newtonian fluid mechanics*, 238:233–241, 2016.

[57] E. Younes, M. Himl, Z. Stary, V. Bertola, and T. Burghelea. On the elusive nature of carbopol gels: "model", weakly thixotropic, or time-dependent viscoplastic materials? *Journal of Non-Newtonian Fluid Mechanics*, 281:104315, 2020. doi: 10.1016/j.jnnfm.2020.104315.

[58] R. Graziano, V. Preziosi, D. Uva, G. Tomaiuolo, B. Mohebbi, J. Claussen, and S. Guido. The microstructure of carbopol in water under static and flow conditions and its effect on the yield stress. *Journal of Colloid and Interface Science*, 582: 1067–1074, 2021. doi: 10.1016/j.jcis.2020.09.003.

[59] I. A. Gutowski, D. Lee, J. R. de Bruyn, and B. J. Frisken. Scaling and mesostructure of carbopol dispersions. *Rheologica acta*, 51:441–450, 2012. doi: 10.1007/s00397-011-0614-6.

[60] P. Lefrançois, E. Ibarboure, B. Payré, E. Gontier, J.-F. Le Meins, and C. Schatz. Insights into c arbopol gel formulations: microscopy analysis of the microstructure and the influence of polyol additives. *Journal of Applied Polymer Science*, 132(46), 2015.

[61] M. Cloitre, R. Borrega, F. Monti, and L. Leibler. Structure and flow of polyelectrolyte microgels: from suspensions to glasses. *Comptes rendus. Physique*, 4(2):221–230, 2003.

[62] B. D. Jofore, P. Erni, G. Vleminckx, P. Moldenaers, and C. Clasen. Rheology of microgels in single particle confinement. *Rheologica Acta*, 54(7):581–600, 2015.

[63] M. Caggioni, V. Trappe, and P. T. Spicer. Variations of the herschel–bulkley exponent reflecting contributions of the viscous continuous phase to the shear rate-dependent stress of soft glassy materials. *Journal of Rheology*, 64(2):413–422, 2020.

[64] V. Trappe and P. Sandkühler. Colloidal gels—low-density disordered solid-like states. *Current opinion in colloid & interface science*, 8(6):494–500, 2004.

[65] T. R. Griffiths and D. C. Pugh. Correlations among solvent polarity scales, dielectric constant and dipole moment, and a means to reliable predictions of polarity scale values from cu. *Coordination Chemistry Reviews*, 29(2-3):129–211, 1979.

[66] J. Wyman Jr. Dielectric constants of polar solutions. *Journal of the American Chemical Society*, 56(3):536–544, 1934.

[67] Lubrizol. Molecular weight of carbopol® and pemulen® polymers. Technical report, Lubrizol, 2007. Technical Data Sheet.

[68] I. A. Gutowski, D. Lee, J. R. de Bruyn, and B. J. Frisken. Scaling and mesostructure of carbopol dispersions. *Rheologica acta*, 51:441–450, 2012.

CHAPTER 3

Trapping of solid inclusions in yield stress fluids

3.1 Introduction

The sedimentation of particles in yield stress fluids (YSF) differs significantly from that in Newtonian fluids. In Newtonian fluids, sedimentation is governed by the balance between gravitational forces and viscous drag. However, YSF introduces the crucial parameter of yield stress (σ_y), the minimum stress required for flow initiation[1,2]. Below σ_y, the fluid behaves as a solid[1], profoundly impacting particle settling. A settling particle generates shear stresses in its vicinity. When these stresses exceed σ_y, a localized yielded region forms around the particle[1–5]. This region, where fluid flow occurs, enables particle sedimentation. The boundary of this yielded region, the yield surface, separates the flowing fluid from the rigid, solid regions[1]. In Bingham plastics, stagnation points can lead to the formation of solid "caps" attached to the sphere[1] (Figure 3.1). This localized yielding and its dependence on particle and fluid properties is central to understanding sedimentation in YSF.

While extensive research has investigated and simulated particle sedimentation in YSF for various materials[1,4,7–13], the sedimentation of small beads within microgel suspensions—especially under high yield stress conditions—remains relatively unexplored. Addressing this gap could yield significant insights into the interplay between microstructure and bulk rheological properties. This study aims to investigate this relationship and proposes a method to connect bulk rheological properties with small-scale behavior in structured fluids.

Holenberg et al. (2012) provided valuable insights into the shape and characteristics of yielded regions around sedimenting particles[14,15]. Their work examined how particle properties, including surface roughness, weight, and sedimentation velocities, affect these regions. For rough, slow-moving particles, the yielded region exhibited a fore-and-aft symmetrical, peach-like shape, aligning with findings from numerical simulations[1,4] (see Figure 3.2).

The size and shape of the yielded region are dynamic and influenced by particle size and shape, fluid yield stress (σ_y), fluid rheology (e.g., Bingham plastic, Herschel-Bulkley fluid), particle concentration, and wall effects[15]. Higher particle concentrations can lead to overlapping yielded regions, which alter flow patterns and sedimentation rates, potentially causing aggregation or flocculation[2]. Wall effects are particularly significant at low Reynolds numbers (where flow is laminar), diminishing below a critical sphere-to-tube diameter ratio[4].

The interaction between sedimenting particles and the surrounding fluid is governed by the formation of a yielded region, which occurs when local stresses induced by a moving particle exceed the yield stress of the fluid. This results in localized flow while adjacent areas remain solid-like[1,2]. Understanding this process is crucial for elucidating

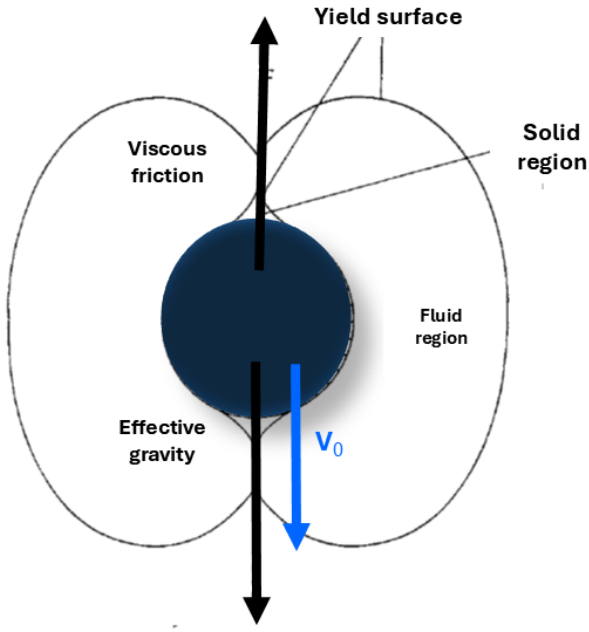

Figure 3.1: Plastic and solid regions for the flow surrounding a solid sphere falling in a Bingham plastic material[6].

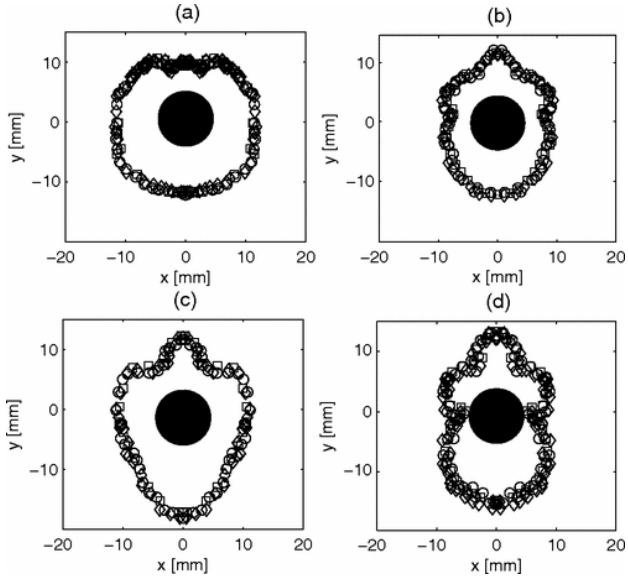

Figure 3.2: Yielded region boundaries for: (a) light rough bead; (b) heavy rough bead; (c) light smooth bead; (d) heavy smooth bead. Various markers correspond to separate runs.[15].

sedimentation dynamics in YSF, marking a departure from the behavior of Newtonian fluids, which lack yield stress. Moreover, recent investigations have revealed the breakdown of fore-aft symmetry in the flow field around the settling sphere, the development of a negative wake, and an extended upstream flow region[15,16].

3.1.1 Sedimentation of a particle in a yield stress fluid

Microgels, viscoelastic YSF components behaving like solids under modest forces like gravity, exhibit fascinating sedimentation phenomena, including delayed sedimentation[17–20]. Extensive research on colloidal particles and microgels reveals a complex interplay between equilibrium thermodynamics and nonequilibrium dynamic processes, but the relationship between their microstructure and macrostructure remains challenging[21–26].

Predicting particle sedimentation requires understanding the balance of forces and the fluid's complex response. This section introduces dimensionless parameters quantifying these interactions, going beyond bulk yield stress.

Net gravitational stress

The primary external force on a sphere in a fluid is the net buoyant force:

$$F_g = \frac{4}{3}\pi R_0^3(\rho_p - \rho_s)g \tag{3.1}$$

where ρ_p is the sphere density, ρ_s is the fluid density, R_0 is the sphere radius, and g is the gravitational acceleration. The gravitational stress can be obtained by dividing the force by a proper surface, which is taken as half of sphere surface:

$$\sigma_g = \frac{2}{3}R_0(\rho_p - \rho_s)g \tag{3.2}$$

Dimensionless yield stress (Y)

Sedimentation in YSF is governed by the interplay between the fluid's yield stress and the stress exerted by the sedimenting particle. The dimensionless yield stress, Y, is the ratio of the fluid's yield stress (σ_y) to the gravitational stress[1,9]:

$$Y = \frac{\sigma_y}{\sigma_g} = \frac{\sigma_y 2\pi R_0^2}{\frac{4}{3}\pi R_0^3(\rho_p - \rho_s)g} = \frac{1.5\sigma_y}{R_0(\rho_p - \rho_s)g} \tag{3.3}$$

Equation (3.3) compares the yield stress magnitude with the applied gravitational stress[9,27]. Sedimentation occurs when particle stress significantly exceeds the fluid's yield stress, initiating flow; sufficient yield stress prevents sedimentation[12,28–31].

The exact value of Y depends on a suitable description of the rheology of the material. Early models of the yielded region around a sedimenting particle utilized Bingham[6,8,32] or Herschel-Bulkley[33] fluid models. Beris et al. (1985) predicted a critical Y value (Y_{crit}) of approximately 0.14 above which sedimentation ceases; however, experimental observations show significant variability (0.12 to 0.60)[34]. The Y values smaller than 1 correspond to the fact that the gravitational stress exerted by the particle must exceed a value large enough to "fluidize" a portion of material surrounding the particle. In other words, the effective radius over which the particle exerts its gravitational stress is larger than the particle's physical radius. This variability is attributed to wall effects[8], microstructural

time-dependence[14,35,36], particle shape[30], deviations from ideal fluid behavior[37], and sensitivity to whether Y_{crit} is measured during cessation or onset of flow[34]. This highlights the limitations of relying solely on bulk yield stress, underscoring the crucial role of the fluid's microstructure[38]. More sophisticated models incorporating microstructural details are necessary[39,40].

Sedimentation in YSF is a coupled process: particle motion drives yielded region formation, while the fluid's response determines the settling velocity[1,2]. Sedimentation occurs only when Y is below a critical value[1], with a plastic boundary layer forming near the critical yield stress[1]. This contrasts with Newtonian sedimentation, which is primarily determined by the balance between gravity and viscous drag. In YSF, sedimentation is governed by a complex interplay of gravity, yield stress, and the fluid's dynamic response within the evolving yielded region[1,2,4,5].

In theory, a practitioner could design a suspension using Y_{crit} to predict the maximum particle size and density a given fluid yield stress can stabilize. However, if structural effects make the Y_{crit} vary too widely, such an approach is not general. In fact, the range of $Y_{crit} = 0.1\tilde{}0.6$ cited above represents a fascinating idea: Two different fluids with the same bulk yield stress can differ in their ability to offset a given particle stress by about six times.

In other words, two fluids with similar yield stresses could differ significantly in their dissipation of particle gravitational stresses, and the bulk yield stress does not fully characterize the fluid response to particle stress at small length scales. This highlights the importance of considering the yielded region's formation and evolution for a complete understanding of sedimentation in yield stress fluids.

Centrifugation studies have further elucidated the relationship between the critical force for motion initiation and particle diameter[2]. This chapter investigates the conditions governing the stability or sedimentation of slightly polydispersed glass microparticles within a suspension of swollen Carbopol microgels. The use of centrifugation allows for precise control of the effective gravitational stress, enabling exploration of a wide range of conditions. This approach offers advantages over traditional sedimentation experiments, where precise control over the applied stress is more challenging.

3.1.2 The role of microstructure

The limitation of bulk yield stress in predicting sedimentation within YSF arises from the complex interplay between macroscopic rheological properties and microscopic fluid structure[38,41]. While bulk yield stress (σ_y) represents the minimum stress required for overall fluid flow, it fails to fully capture the heterogeneous nature of YSF at the particle scale. Sedimentation isn't simply a matter of exceeding σ_y; rather, it depends critically on the fluid's microstructural response to the localized stress field generated by a settling particle[4,11].

The dimensionless yield stress, Y, defined as the ratio of the fluid's yield stress (σ_y) to the stress exerted on the fluid by a particle, quantifies this microstructural influence on sedimentation. A higher Y value indicates a greater ability of the YSF to resist particle sedimentation. The size of the yielded region around a sedimenting particle is directly related to Y. A smaller yielded volume implies less stress dissipation and potentially easier sedimentation. Conversely, a larger yielded volume leads to greater stress dissipation and resistance to sedimentation.

To illustrate this, consider different types of yield stress materials with varying structures (Figure 3.3). Glasses, like aqueous Carbopol, are highly loaded systems with a sponge-like consistency. Gels, such as shampoos, are more dilute suspensions with

strongly interacting particles exhibiting thixotropy. These microstructural differences significantly influence the minimum yielded volume required for particle movement. For example, microfibrous cellulose, with its more open structure, requires a smaller yielded volume compared to the densely packed Carbopol. This difference in minimum yielded volume directly impacts Y_{crit}; microfibrous cellulose can suspend a particle at a lower overall yield stress (and hence a lower Y value) resulting in a lower Y_{crit}. A fluid with a significant minimum yielded volume will have a Y_{crit} value smaller than unity, as predicted by Beris et al. (1985) for Bingham fluids and confirmed in Carbopol systems[1]. However, variations in microstructure lead to different minimum yielded region sizes and, thus, variations in Y_{crit}.

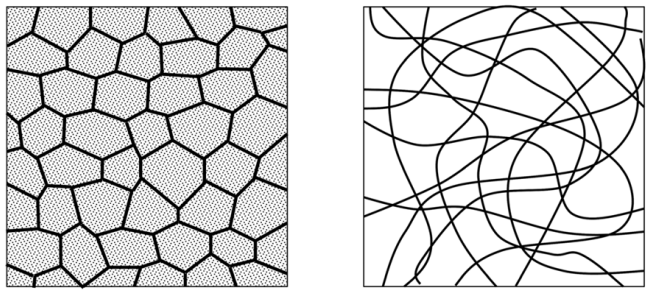

Figure 3.3: Cartoon representation of the two main types of microstructures of YSF: a glassy system of tightly packed, swollen polymer microgel particles with a sponge-like consistency[42], and a gel of high aspect ratio fibers (like microfibrillated cellulose) at low volume fraction[9].

This underscores the importance of considering microstructure when predicting sedimentation in YSF, as bulk yield stress alone is insufficient to fully characterize the fluid's response to localized particle stresses.

3.2 Material and methods

3.2.1 Sample preparation

The microstructure of YSF can be examined using micron-sized particles, either as passive tracers smaller than the fluid constituents or as inclusions larger than the building blocks. In this study, we utilized particles nearly ten times the dimensions of the building blocks (see figure 3.4).

It was explained in chapter 1 that water-based samples were prepared in two states, neutralized and non-neutralized. Then about 0.05 wt% of 50 µm microbeads (Soda-lime glass GL0191B5/45-53 from Mo-Sci Specialty Products, L.L.C, density 2.5 g/cm^3, diameter 50 ± 3 µm) were dispersed into each prepared YSF sample. These samples were mixed for 10 minutes using a power mixer (at 2500 rpm) to ensure uniform tracer distribution.

Each sample was then analyzed by taking multiple images, which were processed using ImageJ software. The analysis provided data on the number and size distribution of micro-beads within the samples, revealing a Gaussian distribution centered around 52

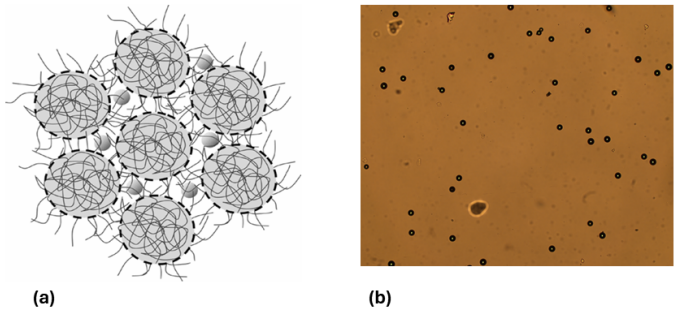

Figure 3.4: (a): A schematic representation of microbeads within the structure of Carbopol suspensions, (b): An actual picture of 0.05 wt% polydispersed glass microparticles inside C971NF 0.5 wt% was taken under a microscope

µm in diameter. Figure 3.5 illustrates a representative distribution from sample C971NF at 0.5 wt%.

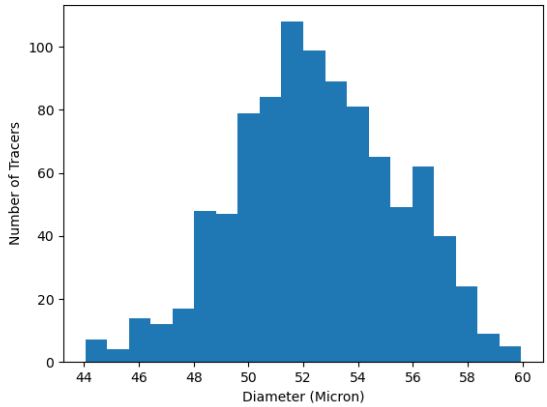

Figure 3.5: Size distribution of soda lime glass microspheres in sample C971NF at 0.5 wt%.

3.2.2 Centrifugation

Centrifugation allows us to select an effective "artificial gravity" for a density-mismatched particle suspended in a medium and thus to tune the force acting on it (see Figure 3.6)

$$F_{eff} = \frac{4}{3}\pi R_0^3(\rho_p - \rho_s)\omega^2 r \tag{3.4}$$

where r is the radius of the rotor and ω the rotational speed. Centrifugation was performed using an Eppendorf® Centrifuge model 5702 (Max. RCF: 3000 x g, Rotor length 12 cm), capable of angular speeds ranging from 100 to 4400 rpm, generating effective accelerations from 1g to 3000g, depending on speed and radial distance.

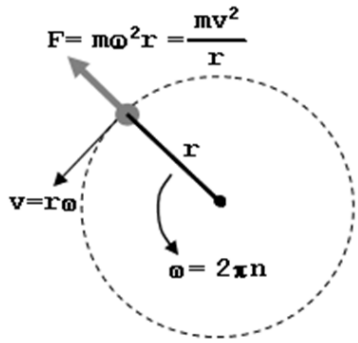

Figure 3.6: demonstrating effective gravitational influence on the sample, dependent upon distance, velocity, and mass of the particle

By introducing the microparticles into YSF samples and subjecting them to centrifugal forces provides a controlled method to investigate trapping mechanisms within the fluid's structure. A centrifuge allows for precise tuning of the applied stress over a wide range. This method offers two degrees of freedom for manipulating the stress experienced by the tracers: (1) radial position within the centrifuge, with greater centrifugal force exerted on microparticles farther from the center of rotation; and (2) rotation speed, with higher speeds generating greater forces. By varying both radial position and rotation speed, a range of forces can be applied to the tracers, enabling systematic study of their trapping behavior within the YSF microstructure.

Importantly, in this work, it was verified that, within the range of centrifugation speeds employed, no significant compression or restructuring of the specimen occurred.

3.2.3 Capillary test

This section visually demonstrates the concept of gravitational effects on microparticles using capillary. Thin rectangular hollow glass capillaries (internal dimensions: 0.50 mm × 5.00 mm, wall thickness: 0.35 mm ± 20%, CM Scientific) were filled with a well-mixed sample containing microparticles. Both ends of each capillary were sealed with Norland Optical Adhesive 81 (NOA81) and cured using UV light for 5 minutes.

The capillaries were positioned vertically within centrifuge tubes, oriented radially to expose them to a gradient of gravitational stress. This setup produced a spectrum of particle sedimentation within each capillary, allowing for direct observation of how varying gravitational forces influence particle distribution (see Fig. 3.7 a, b, and c). The images illustrate the filled and sealed capillary, the trapped microparticles observed under a microscope, and the resulting spectrum of microparticle distribution, respectively, which indicates a decrease in particle concentration towards areas of higher gravitational stress due to centrifugation.

This experimental approach utilizing capillaries (Figure 3.7) provided clear visual confirmation of size-dependent sedimentation behavior.The gradient of gravitational stress within the capillary allowed for observation of a clear spatial distribution of microparticles along the length of the capillary. Furthermore, concentrations below 0.05 wt% beads were tested; reducing the bead concentration did not affect the threshold location in the capillary.

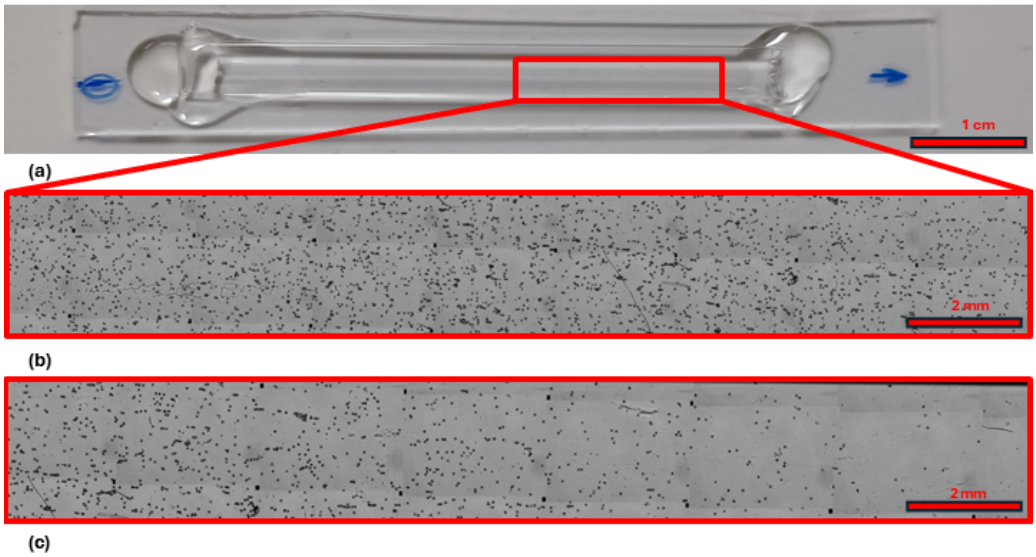

Figure 3.7: (a): The appearance of filled and sealed capillary; (b): The highlighted portion of the capillary imaged in the microscope before centrifugation; (c): The same portion after centrifugation.

3.2.4 Assessment of particle trapping

The samples were transferred into 1.5 ml microtubes, which were then placed within larger centrifuge tubes; each larger tube accommodated four microtubes. This arrangement allowed for the simultaneous application of varying centrifugal forces within a single centrifuge run, creating four distinct zones of differing stress. Prior to centrifugation, the initial distribution of tracers in each microtube was characterized. A droplet from each microtube was sandwiched between two glass slides and imaged using a Nikon TE 200 inverted microscope equipped with Nikon objective lenses (5x), a TE-PSE100 lamp, and a Nikon DS-Fi3 camera. A TANGO 3 Desktop device (Marzhauser Sensotech) controlled automated stage movement for image acquisition. All imaging was performed under incoherent spatial illumination achieved by opening the condenser aperture diaphragm to obtain a relatively narrow focal depth and, thus, a better resolution across the sample gap. By using ImageJ software, all recorded images were analyzed, and the number and size distribution of the tracers were recorded for each microtube.

In the following step, each sample was subjected to a variety of forces to evaluate the maximum capacity of their structure to capture tracers.

To ensure that steady-state conditions were achieved in each experiment, the possible sedimentation time was calculated using a numerical solution to the equation of motion. This equation considered the average particle size located at the highest part of the sample, which must traverse the entire vial. The calculation was performed by equating gravitational stress and yield stress, where yield stress is a function of shear-dependent viscosity and shear rate (the viscosity sets the sedimentation velocity of untrapped particles, which on turn determines the shear rate and thus the effective viscosity experienced

by the particles).

In a sedimentation scenario, sedimentation occurs when the effective gravitational stress exceeds the yield stress of the material and the particle proceeds at constant velocity, with equal viscous drag and gravitational drive. In a rotating system with angular frequency ω and radial position $R_r = X$, the effective gravitational force is obtained by replacing g with the centrifugal acceleration $\omega^2 R_r$:

$$\sigma_g = \frac{2}{3} R_0(\rho_p - \rho_s)\omega^2 X \tag{3.5}$$

Equating the gravitational stress to the viscous stress, which is modeled as $\sigma_y = \eta(\dot{\gamma})\dot{\gamma}$ where $\eta(\dot{\gamma})$ is the shear-dependent viscosity and $\dot{\gamma}$ is the shear rate, yields:

$$\frac{2}{3} R_0(\rho_p - \rho_s)\omega^2 X = \eta(\dot{\gamma})\dot{\gamma} \tag{3.6}$$

The shear rate is estimated as:

$$\dot{\gamma} = \frac{\dot{X}}{2R_0} \tag{3.7}$$

Substituting this into Equation 3.6, we obtain a differential equation for the particle position $X(t)$:

$$\frac{dX}{dt} = \dot{X} = \frac{4R_0^2(\rho_p - \rho_s)\omega^2 X}{3\eta(\dot{\gamma})} \tag{3.8}$$

Assuming a constant viscosity η, the equation is separable and can be integrated to yield:

$$\int_{X_{initial}}^{X_{final}} \frac{dX}{X} = \int_0^t \frac{4R_0^2(\rho_p - \rho_s)\omega^2}{3\eta} dt \tag{3.9}$$

This leads to the final expression for the sedimentation time t:

$$t = \frac{3\eta}{4R_0^2(\rho_p - \rho_s)\omega^2} \ln\left(\frac{X_{\text{final}}}{X_{\text{initial}}}\right) \tag{3.10}$$

This equation provides an estimate of the time required for sedimentation of unlocked particles. Note that this model assumes a fixed value for viscosity η; the acceleration equation allows us to calculate the sedimentation time by applying the equations of motion for a particle. These calculations presume a constant centrifugal force at the nearest point to the center of the centrifuge, which approximates the maximum force necessary for the entire sample.

This method corresponds to a maximum sedimentation time of 16 hours for the smallest microparticles at the highest concentration. The 16-hour duration is a conservative upper bound, as the actual time to reach steady state depends on factors such as concentration, density mismatch, particle size, and applied gravitational stress. To guarantee steady-state conditions for all samples, each was centrifuged for at least 16 hours before resampling.

Control experiments were performed using 3 wt% neutralized C971NF samples. These samples were placed directly into larger centrifuge tubes, without the use of microtubes, and their sedimentation behavior over time was compared to theoretical calculation (Fig. 3.8). Resampling involved collecting samples from the midpoint of each microtube to

determine the number and size distribution of the remaining microparticles. Given the known distance from the center, the precise gravitational force may be determined. All samples were sampled from the middle of the tube, and all experiments and sampling were conducted at room temperature (22°C).

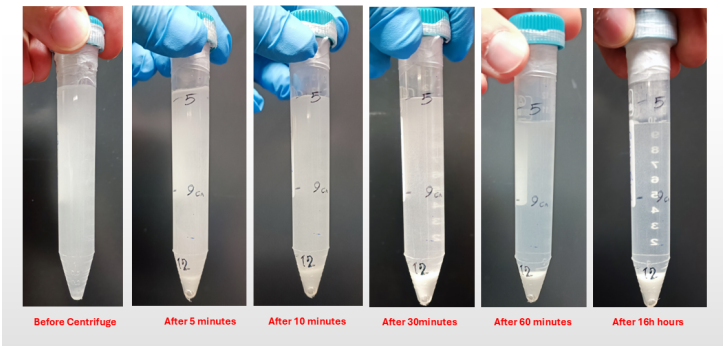

Figure 3.8: Evolution of sedimentation of dispersed microparticles in 3 wt% C971 NF suspension in water over 16 hours centrifugation

Pre- and post-centrifugation samples were analyzed to establish a baseline and monitor microparticle retention. Prior to centrifugation, microparticle size distributions were influenced by microparticle concentration and the number of images acquired. Figure 3.5 illustrates a representative distribution from sample C971NF at 0.5 wt%. To ensure consistency across samples and minimize errors in the study, the same number of eight images was maintained for all samples, and efforts were made to keep particle concentration consistent. The post-centrifugation analysis focused on the remaining microparticle number and size distribution. A threshold for microparticle retention was defined as the point at which the number of microparticles decreased to 50% of the initial count (Figure 3.9 a), identifying the critical gravitational stress. The analysis demonstrated consistent agreement between this threshold and the observed changes in the size distribution. Beyond the 50% drop in the number of remaining microparticles, we also see a decrease in their average size. However, because many microparticles have been lost, the remaining sample size is smaller. This smaller sample size leads to a higher degree of variability or uncertainty in the average size calculation. Essentially, the reduced statistical power of the smaller sample size makes it difficult to accurately determine the true average size and increases the likelihood that the smallest tracers might not be reliably detected within the remaining population. The biggest remaining tracer diameter is plotted, which is systematically larger than but has the same trend as the average diameter (Figure 3.9 b).

Using this 50% retention threshold as a criterion, the experiment was repeated for various concentrations of C971NF, both with and without neutralizer, resulting in a comprehensive data set 3.17.

3.2.5 Optical assessment of particle trapping during centrifugation

To explore the time-dependent concentration of suspended particles in the yield stress fluid (YSF), which is influenced by the shear-thinning nature of the material, we designed a modified centrifuge setup that provides optical access to the rotating samples. This arrangement enables real-time turbidity measurements during centrifugation.

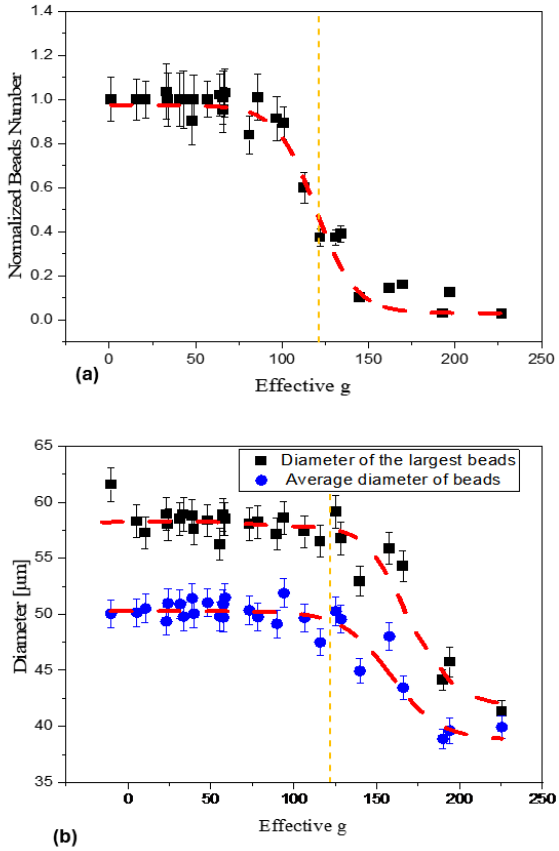

Figure 3.9: (a):The graph shows the normalized number of microparticles from the initial sampling before centrifugation, plotted versus effective gravity. (b): The plot shows how the maximum (squares) and average (circles) radii of microparticles dropped as gravity increased after reaching the critical gravitational stress.

Experimental setup. A Thorlabs LC100 Smart Line Camera (USB 2.0) was used, featuring a 2048-pixel linear Si CCD array (350–1100 nm detection range, pixel size: $14\,\mu$m $\times$ $56\,\mu$m, pitch $14\,\mu$m). The camera was mounted on a bench centrifuge with a modified open lid, allowing direct optical access to the sample. Sedimentation experiments were conducted in BrandTech™ BRAND™ plastic spectrophotometer cuvettes (2 mm path length, 2 mL volume). A custom 3D-printed cell holder was designed to secure the cuvette and provide unobstructed illumination paths (Figure 3.10).

Illumination and optical access. An LED strip beneath the cuvette provided homogeneous illumination, with multiple diffusing layers to minimize light intensity variation. A custom circular plate with a rectangular aperture was used as a mask, confining the illuminated region and creating a dark background elsewhere. The entire setup was placed in a dark room to reduce ambient light interference. However, because there were no collection optics above or below the cuvette, the final recorded signal lacked optimal resolution.

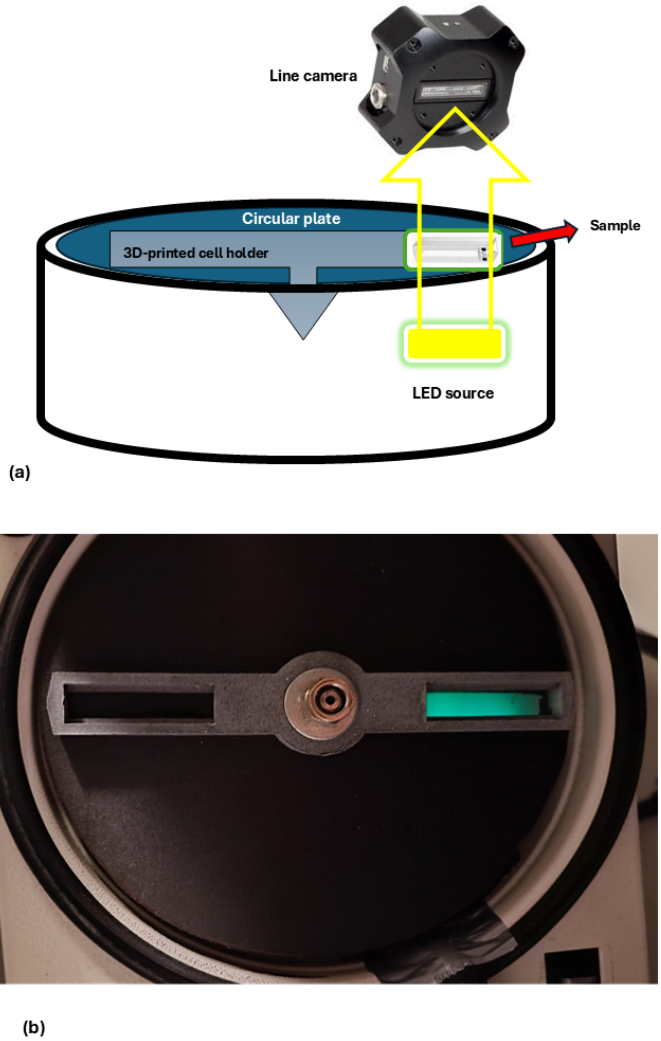

Figure 3.10: (a) Schematic of the device showing the LED source, the sample in the centrifuge holder and the line camera. (b) Top view of the custom-built cuvette holder: a circular aperture plate with a rectangular window restricts illumination to the region of interest.

In our setup, some factors were not fully optimized:

- **Lack of collection optics:** Close positioning of the line camera to the sample allowed to estimate transmitted light through different layers of the sample but the absence of illumination or collection optics hindered a proper imaging scheme and significantly reduced effective spatial resolution.
- **Camera speed and triggering:** The Thorlabs LC100 camera has no built-in trigger option, so we recorded continuously during centrifugation. This continuous recording averaged the transmitted light signal, reducing temporal resolution.
- **Illumination intensity:** Although an LED strip and diffusers provided uniform

illumination, the intensity was not optimized for maximum contrast.

Initial calibration. Before each experiment, a blank cuvette (filled only with solvent) was recorded to establish a baseline intensity profile (Figure 3.11). Subsequent turbidity profiles were normalized by this baseline to correct for systematic intensity variations and to focus on relative changes caused by particle sedimentation.

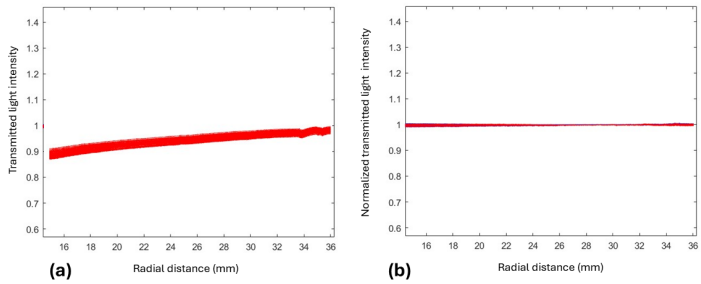

Figure 3.11: Illustration of baseline correction at 2000 rpm. (a) Raw data. (b) Normalized data.

Spatial resolution and concentration calibration. To determine the effective spatial resolution, we placed black masks of known dimensions and positions on the cuvette (Figure 3.12). The transmitted light profile served as calibration, indicating how distinct features were determined. As shown in the Figure, severe smoothing of profiles is observed.

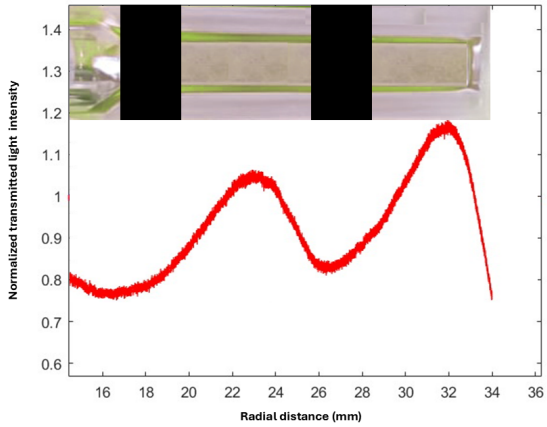

Figure 3.12: Spatial resolution assessment at 2000 rpm using black markers of known width. The measured width in the image helps estimate effective system resolution.

A semi-quantitative intensity–concentration relationship was also determined by measuring transmitted light through serial dilutions of microparticles (Figure 3.13). The measured intensity I scales as $I \propto c^{-\alpha}$, where $\alpha = 0.07$.

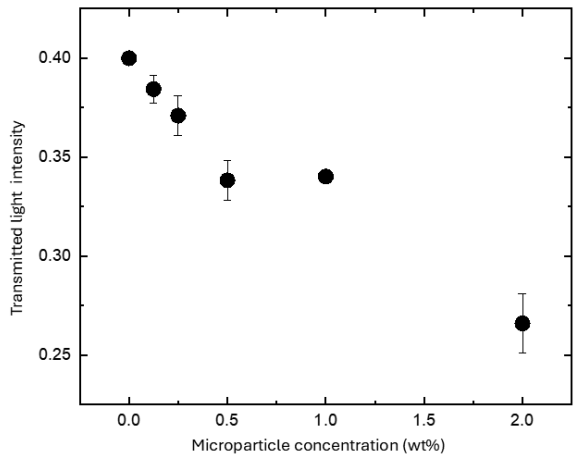

Figure 3.13: Calibration curve showing the relationship between transmitted light intensity and microparticle concentration.

Sedimentation dynamics. When the centrifuge speed exceeded a critical threshold, particle sedimentation in the YSF was observed, altering the transmitted light intensity both spatially and temporally. Despite the aforementioned limitations in camera speed, triggering, and optics, continuous intensity profiles recorded by the line camera provided valuable real-time insights into the evolving distribution of particles during centrifugation.

3.3 Results and discussion

This chapter investigates the stable entrapment of microparticles in YSF, focusing on the equilibrium between yield stress and gravitational stress. We explore the conditions of (in)stability of glass microspheres (50 µm diameter, 2.5 g/cm³ density), which are smaller than previously investigated inclusions but still larger than the building blocks of the YSF, thus enabling a continuum description. Centrifugation allowed tuning of the gravitational stress, enabling a wide range of applied stresses. The samples comprised Carbopol suspensions at varying concentrations and pH levels, using both aqueous (water-based) and non-aqueous (PG) solvents.

In Figure 3.14, we provide a schematic overview of the particle trapping experiments using centrifugation. Figure 3.14(a) provides a simplified representation of the experimental setup and the particle trapping principle, illustrating the relationship between particle size and force experienced during centrifugation. Larger microparticles, subjected to greater centrifugal forces, are depicted as being more readily untrapped. Figure 3.14(b) shows a Cryo-SEM image of the C974NP microgel structure, very similar to the C971 used in these experiments[43].

Panels 3.14(c) and 3.14(d) depict the effects of increasing gravitational stress (σ_g) on density-mismatched particles within the YSF matrix. These figures simulate the behavior observed during centrifugation, effectively representing a localized creep experiment. Below the yield stress (σ_y) of the YSF, the material behaves as a solid and all tracer particles remain trapped (Figure 3.14(c)). Increasing the centrifugation speed (and thus σ_g)

leads to sedimentation of larger particles first, while smaller particles remain trapped (Figure 3.14(d)). Further increases in σ_g, exceeding σ_y, result in sedimentation of all tracer particles (Figure 3.14(d)). This observation highlights the relationship between applied stress, particle size, and the trapping capacity of the YSF. The effect of particle size on sedimentation in YSF, showing larger particles sedimenting and small particles remaining trapped, is consistent with the concept of an "inverted sieve" separating particles based on their size, with the threshold set by the applied stress [2].

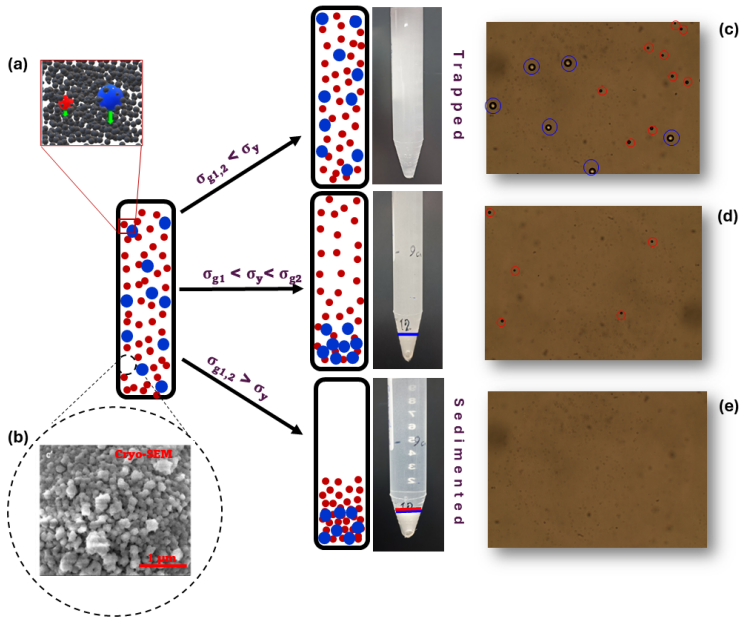

Figure 3.14: (a): A cartoon illustration of the trapped tracers in Carbopol gels (b): Cryo-SEM pictures of Carbopol 974P NF at 0.25 wt% adjusted to pH 7.4 [43]. Depending on particle size and applied stress, the outcomes are varied: (c) all particles remain trapped; (d) only smaller particles remain trapped, while larger ones get untrapped; or (e) all particles sediment through the sample.

3.3.1 Correlation between bulk yield stress and critical gravitational stress

Chapter 2 detailed bulk yield stress (σ_y) determination using a rotational rheometer and the TC model. We now explore the relationship between σ_y and the critical gravitational stress ($\sigma_{g,crit}$) initiating sedimentation, determined as the stress at which 50% of microparticles remained entrapped.

Experiments across various Carbopol concentrations showed a linear correlation between critical gravitational stress ($\sigma_{g,crit}$) and yield stress (σ_y) for both neutralized and non-neutralized aqueous samples (Figure 3.16). The slope of about 5.3, corresponding to a dimensionless yield stress (Eq. 3.3), i.e. the ratio of σ_y to $\sigma_{g,crit}$ of 0.19 ± 0.02, indicates a fluidized region extending beyond the particle surface [9,44]. A simple scaling argument based on this stress ratio leads to an estimate of an effective radius of $r_{\text{fluidized}} \approx \sqrt{5.3} R_0 \sim 2.3\, R_0$. In classical creeping-flow analyses, a similar stress ratio lead to an estimate of $r_{\text{fluidized}} \approx 1.7\, R_0$ [1,9].

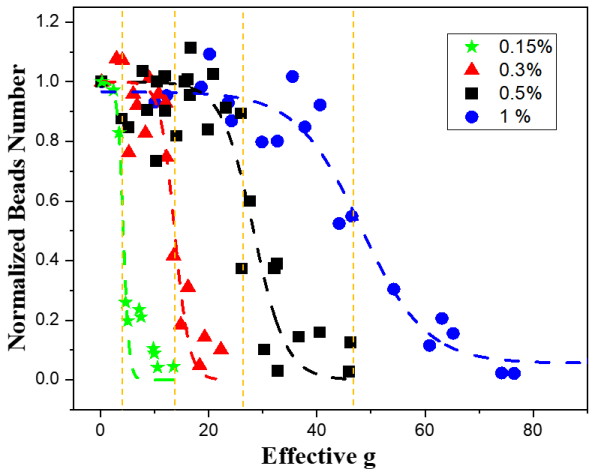

Figure 3.15: The graph illustrates the relationship between gravitational stress and the quantity of remaining particles in Carbopol samples at varying concentrations. As the concentration increases, the remaining particles diminish under higher gravitational forces. The critical gravitational stress, defined as the point where 50% of particles remain, shows a increase with concentration. Symbols represent different concentrations: circles for 1 wt%, squares for 0.5 wt%, triangle for 0.3 wt% and stars for 0.15%.

However, this may be influenced by the degree of swelling[2,9]. Indeed, the relationship between bulk yield stress and critical gravitational stress for sedimentation, while approximately linear, demonstrates the importance of considering microstructural details, as evidenced by small deviations between samples with identical σ_y but differing solvents or pH[37].

Specifically, at equivalent yield stresses, neutralized suspensions (with larger, more swollen microgels) typically exhibit slightly lower $\sigma_{g,crit}$ than non-neutralized suspensions (with smaller, denser microgels). In fact, Figure 3.16 shows that neutralized suspensions have a slope of 0.19, but non-neutralized suspensions have a slope of 0.15. The 20% slope difference implies a larger fluidized region in non-neutralized suspensions. This suggests that the smaller, denser microgels in the non-neutralized suspensions, despite requiring higher C971 NF concentrations to achieve the same yield stress (Chapter 2, Figure 2.14), exhibit superior particle trapping ability, explaining the slightly higher $\sigma_{g,crit}$ observed in Figure 3.16. In other words, larger, more swollen microgels (in the neutralized suspension) with the same bulk yield stress are less capable of trapping and releasing particles than smaller, dense microgels.

Experiments conducted using non-aqueous solvents (PG) also exhibited a linear correlation between yield stress and critical gravitational stress (Figure 3.17). Remarkably, this behavior closely resembles that observed in aqueous samples. The slopes of the linear fits (Figure 3.17) are similar, approximately 0.15 for neutralized samples and 0.13 for non-neutralized samples. While this difference is not statistically significant, it aligns with the discussion in Chapter 2 regarding the reduced influence of pH on non-aqueous solutions compared to aqueous solutions.

A comparison of aqueous and non-aqueous systems reveals the significant effect of solvent choice. As discussed in Chapter 2, microgel size is larger in aqueous suspensions than in non-aqueous suspensions. Consequently, the fluidification region is broader in

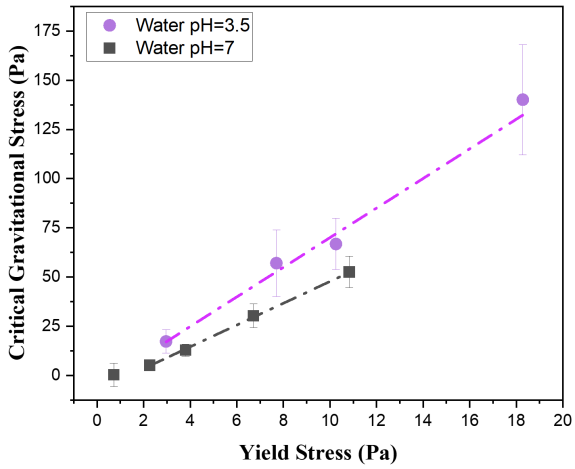

Figure 3.16: The correlation between critical gravitational stress ($\sigma_{g,crit}$) and bulk yield stress (σ_y) in water-based suspensions. Data are shown for neutralized (black squares) and non-neutralized (purple circles) samples, with linear fits indicating slopes of 5.3 and 6.8, respectively (corresponding to inverse slopes of 0.19 and 0.15).

non-aqueous solvents due to the higher density of microgels in these samples. These observations underscore the influence of microstructural factors on sedimentation[9].

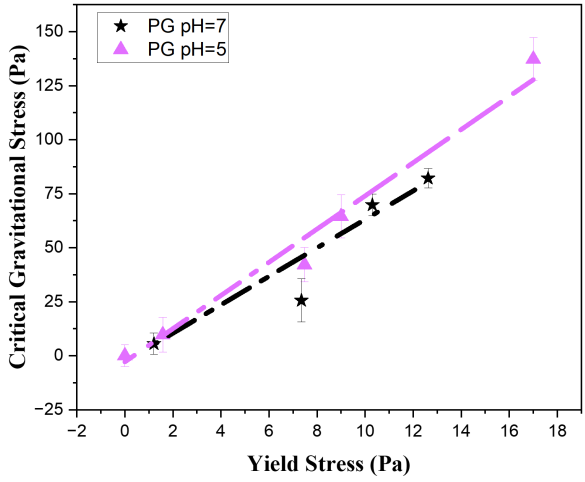

Figure 3.17: Correlation between critical gravitational stress ($\sigma_{g,crit}$) and bulk yield stress (σ_y) for PG suspensions. Data are presented for neutralized (black stars) and non-neutralized (purple triangles) samples. Linear fits yield slopes of 6.6 and 7.7, respectively, corresponding to inverse slopes of 0.15 and 0.13)

3.3.2 Centrifugation as a localized creep experiment and particle size separation

Applying gravitational stress (σ_g) via centrifugation mimics a localized creep experiment[32]. Indeed, previous active microrheology experiments, applying optical stress on microparticles embedded in YSF and mimicking a localized creep experiment, showed a good correlation between small-scale experiments and bulk yield stress values[45]. Here, the controlled increase in σ_g reveals sequential sedimentation based on particle size (Figure 3.14 d and e). Larger particles sediment first, with smaller particles remaining entrapped until higher σ_g is reached. This corresponds to an inverted sieve, holding small particles rather than larger ones. The numerical challenges in accurately resolving the surface of the yielded region, as highlighted in studies of creeping flow around a sphere[32], are also relevant to interpreting the results obtained via centrifugation.

Figures 3.14 d, e and 3.7 c show a systematic decrease in the average size of remaining particles with increasing σ_g. However, the reduction in particle number increases uncertainty in the average size estimate due to decreased sample size. Therefore, higher σ_g leads to higher variability in the average size of remaining tracers. This highlights a limitation to the technique 3.15.

3.3.3 Sedimentation transient in YSF

The sedimentation kinetics of a 1 wt% C971 NF aqueous suspension were investigated as a benchmark system to elucidate microparticle behavior within a yield stress fluid. Figure 3.18 presents tracer concentration profiles under three different centrifugal force regimes. These were derived from the intensity profile of transmitted light, using the calibration procedure detailed in Figure 3.13. In these profiles, blue traces indicate early stages of centrifugation, while red regions indicate later time intervals (2 hours).

Figure 3.18 illustrates a scenario where the centrifugal force is below the critical yield stress at any position along the sample, resulting in no observable sedimentation and a constant intensity profile. In contrast, Figure 3.18 b shows that sedimentation occurs along the whole monitored portion of the sample, because centrifugal forces slightly exceed the yield stress. The concentration profiles decrease over time as particles leave that part of the vial (on the left side of the image). The sedimentation velocity exhibits a radial dependence, increasing with distance from the centrifuge's center (which lies on the right of the image), because of two concurring factors: Firstly, the centrifugal force acting on each bead increases linearly with its radial distance from the rotation axis ($F_c \propto r$). This results in a radially increasing outward force, accelerating beads towards the outer wall of the cell. Secondly, the Carbopol suspension exhibits shear-thinning behavior. The increased bead velocity resulting from the centrifugal force leads to a reduction in the apparent viscosity of the suspension. This decrease in viscosity further enhances the bead sedimentation rate, creating a positive feedback loop where increased centrifugal force leads to higher velocities and lower viscosity, accelerating the overall process.

The complexity of the observed sedimentation profile arises because, upon exceeding the yield stress, particles near the center must traverse the entire sample length to sediment, while particles at the periphery sediment more readily (as the particles settle at different rates depending on their position within the centrifuge, the upper particles replace the lower particles). Figure 3.18 c shows rapid sedimentation under a significantly higher centrifugal force across the whole sample. These profiles offer valuable qualitative insights into the transition from solid-like to liquid-like behavior in the sample, although the full quantitative analysis of the profiles in Figures 3.18b and 3.18c is impaired by two primary limitations: (1) inhomogeneities in the illumination system; (2)

poor space resolution; and (3) the camera's insufficient frame rate to accurately resolve particle motion at higher rotational speeds (e.g., 3000 rpm). To address these limitations, future experiments would require a more homogeneous illumination system, better coupling of the detector, and a high-speed camera capable of capturing individual rotational cycles or, alternatively, a system to obtain an accurate average over many cycles via optical triggering.

3.4 Conclusion

The trapping of microscale particles within yield-stress fluids (YSF) was investigated, focusing on Carbopol microgel suspensions. While previous research extensively explored sedimentation in YSF for mm-scale particles, this work addressed the behavior of microparticles in highly concentrated microgels, bridging the gap between macroscopic rheological properties and microscopic structure. Our methodology employed two centrifuge systems: a steady-state system using microtubes and capillary tests to determine $\sigma_{g,crit}$ and a time-resolved system incorporating a line camera and custom apparatus for real-time sedimentation kinetics observation. The steady-state measurements revealed a linear correlation between σ_y and $\sigma_{g,crit}$ across various Carbopol concentrations, pH levels, and solvents (aqueous and propylene glycol). For aqueous systems, the slope of this correlation is 0.19 ± 0.02, consistent with theoretical predictions and suggesting a fluidized region around the particle approximately five times its volume. Deviations from this theoretical slope were observed in non-neutralized samples and non-aqueous solvents, likely due to microstructural differences in microgel swelling. Neutralized suspensions (with larger, swollen microgels) showed slightly lower $\sigma_{g,crit}$ values compared to non-neutralized suspensions at equivalent σ_y, highlighting the impact of microstructure. Importantly, we observed a consistent linear proportionality between σ_y and $\sigma_{g,crit}$ across the entire concentration range, from the initial onset of sedimentation to the plateau region. Centrifugation effectively emulated a localized creep experiment, demonstrating size-dependent sedimentation; larger particles sedimented first, followed by smaller ones with increasing $\sigma_{g,crit}$. In conclusion, this study demonstrates a robust correlation between bulk yield stress and critical gravitational stress for microparticle sedimentation in Carbopol microgel suspensions. Our findings thus suggest a rapid, indirect method for estimating yield stress (σ_y) using centrifugation to determine a critical gravitational stress ($\sigma_{g,crit}$). This method involves dispersing microparticles within the YSF and then measuring the gravitational stress required to initiate significant particle sedimentation (defined here as 50% particle retention). The method's effectiveness is limited by particle size and suspension concentration. When the particle size approaches that of the microgels, or when high concentrations necessitate excessively high centrifugal forces, the method becomes unreliable due to potential microgel structural collapse.

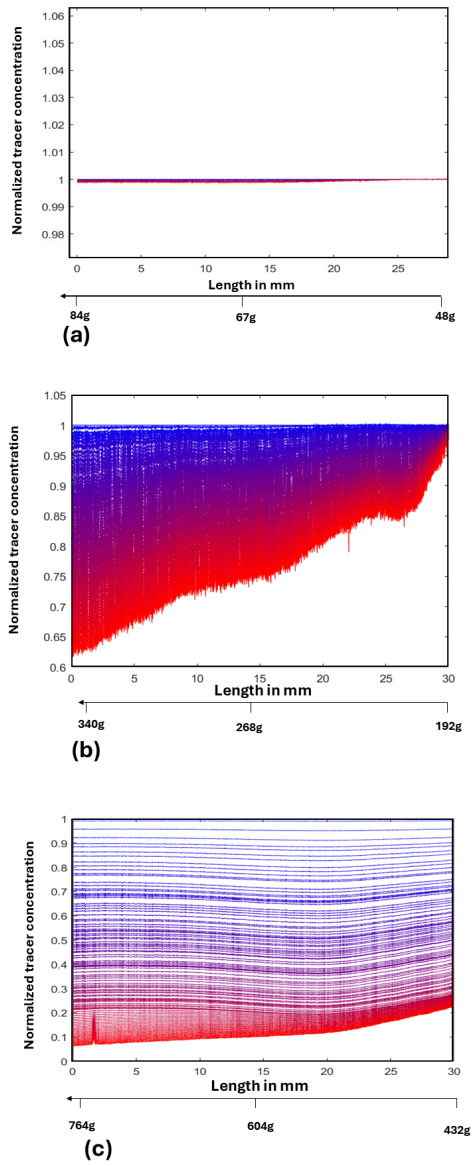

Figure 3.18: Normalized tracer concentration profiles illustrating the sedimentation kinetics of a 1 wt% C971 NF aqueous suspension under varying centrifugal forces (larger centrifugation time from blue to red). Profiles are shown for (a) 1000 rpm (120 min, sub-yield stress conditions), (b) 2000 rpm (120 min, near-yield stress conditions), and (c) 3000 rpm (60 min, super-yield stress conditions).

Bibliography

[1] A. Beris, J. Tsamopoulos, R. Armstrong, and R. Brown. Creeping motion of a sphere through a bingham plastic. *Journal of Fluid Mechanics*, 158:219–244, 1985.

[2] A. Madani, S. Storey, J. A. Olson, I. Frigaard, J. Salmela, and D. Martinez. Fractionation of non-brownian rod-like particle suspensions in a viscoplastic fluid. *Chemical engineering science*, 65(5):1762–1772, 2010.

[3] J. Liétor-Santos, C. Kim, P. Lu, A. Fernández-Nieves, and D. Weitz. Gravitational compression of colloidal gels. *The European Physical Journal E*, 28(2):159–164, 2009.

[4] D. Atapattu, R. Chhabra, and P. Uhlherr. Wall effect for spheres falling at small reynolds number in a viscoplastic medium. *Journal of Non-Newtonian Fluid Mechanics*, 38(1):31–42, 1990.

[5] G. Brambilla, S. Buzzaccaro, R. Piazza, L. Berthier, and L. Cipelletti. Highly nonlinear dynamics in a slowly sedimenting colloidal gel. *Physical review letters*, 106(11): 118302, 2011.

[6] A. N. Beris, J. A. Tsamopoulos, R. C. Armstrong, and R. A. Brown. Creeping motion of a sphere through a bingham plastic. *J. Fluid Mech.*, 158:219–244, 1985.

[7] M. Beaulne and E. Mitsoulis. Creeping motion of a sphere in tubes filled with herschel–bulkley fluids. *Journal of non-newtonian fluid mechanics*, 72(1):55–71, 1997.

[8] J. Blackery and E. Mitsoulis. Creeping motion of a sphere in tubes filled with a bingham plastic material. *J. Non-Newtonian Fluid Mech.*, 70(1-2):59–77, 1997.

[9] H. Emady, M. Caggioni, and P. Spicer. Colloidal microstructure effects on particle sedimentation in yield stress fluids. *Journal of Rheology*, 57(6):1761–1772, 2013.

[10] O. Merkak and et al. Migration and sedimentation of spherical particles in a yield stress fluid flowing in a horizontal cylindrical pipe. *AIChE journal*, 55(10):2515–2525, 2009.

[11] L. Jossic and A. Magnin. Drag and stability of objects in a yield stress fluid. *AIChE journal*, 47(12):2666–2672, 2001.

[12] H. Tabuteau and et al. Drag force on a sphere in steady motion through a yield-stress fluid. *Journal of Rheology*, 51(1):125–137, 2007.

[13] G. Ovarlez and et al. Shear-induced sedimentation in yield stress fluids. *Journal of Non-Newtonian Fluid Mechanics*, 177-178:19–28, 2012.

[14] M. Gueslin and et al. Flow induced by a sphere settling in an aging yield-stress fluid. *Physics of Fluids*, 18(10):103101, 2006.

[15] Y. Holenberg, O. M. Lavrenteva, U. Shavit, and A. Nir. Particle tracking velocimetry and particle image velocimetry study of the slow motion of rough and smooth solid spheres in a yield-stress fluid. *Physical Review E—Statistical, Nonlinear, and Soft Matter Physics*, 86(6):066301, 2012.

[16] A. Putz and et al. Settling of an isolated spherical particle in a yield stress shear thinning fluid. *Physics of Fluids*, 20(3):033102, 2008.

[17] M. L. Kilfoil, E. E. Pashkovski, J. A. Masters, and D. Weitz. Dynamics of weakly aggregated colloidal particles. *Philosophical Transactions of the Royal Society of London. Series A: Mathematical, Physical and Engineering Sciences*, 361(1805):753–766, 2003.

[18] J. Y. Huh, M. L. Lynch, and E. M. Furst. Microscopic structure and collapse of depletion-induced gels in vesicle-polymer mixtures. *Physical Review E—Statistical, Nonlinear, and Soft Matter Physics*, 76(5):051409, 2007.

[19] R. Buscall, T. H. Choudhury, M. A. Faers, J. W. Goodwin, P. A. Luckham, and S. J. Partridge. Towards rationalising collapse times for the delayed sedimentation of weakly-aggregated colloidal gels. *Soft Matter*, 5(7):1345–1349, 2009.

[20] P. Bartlett, L. J. Teece, and M. A. Faers. Sudden collapse of a colloidal gel. *Physical Review E—Statistical, Nonlinear, and Soft Matter Physics*, 85(2):021404, 2012.

[21] M. Karg, A. Pich, T. Hellweg, T. Hoare, L. A. Lyon, J. Crassous, D. Suzuki, R. A. Gumerov, S. Schneider, I. I. Potemkin, et al. Nanogels and microgels: From model colloids to applications, recent developments, and future trends. *Langmuir*, 35(19): 6231–6255, 2019.

[22] B. H. Tan, K. C. Tam, Y. C. Lam, and C. B. Tan. Microstructure and rheology of stimuli-responsive microgel systems—effect of cross-linked density. *Advances in colloid and interface science*, 113(2-3):111–120, 2005.

[23] E. Dieuzy, G. Aguirre, S. Auguste, K. Chougrani, V. Alard, L. Billon, and C. Derail. Microstructure-driven self-assembly and rheological properties of multi-responsive soft microgel suspensions. *Journal of Colloid and Interface Science*, 581:806–815, 2021.

[24] L. Cipelletti and L. Ramos. Slow dynamics in glassy soft matter. *Journal of Physics: Condensed Matter*, 17(6):R253, 2005.

[25] E. Zaccarelli. Colloidal gels: equilibrium and non-equilibrium routes. *Journal of Physics: Condensed Matter*, 19(32):323101, 2007.

[26] C. Patrick Royall, S. R. Williams, T. Ohtsuka, and H. Tanaka. Direct observation of a

local structural mechanism for dynamic arrest. *Nature materials*, 7(7):556–561, 2008.

[27] P. Laxton and J. Berg. Gel trapping of dense colloids. *Journal of Colloid and Interface Science*, 285(1):152–157, 2005.

[28] D. D. Atapattu, R. P. Chhabra, and P. H. T. Uhlherr. Wall effect for spheres falling at small reynolds number in a viscoplastic medium. *J. Non-Newtonian Fluid Mech.*, 38 (1):31–42, 1990.

[29] D. D. Atapattu, R. P. Chhabra, and P. Uhlherr. Creeping sphere motion in herschel–bulkley fluids: Flow field and drag. *J. Non-Newtonian Fluid Mech.*, 59(1-3): 245–265, 1995.

[30] L. Jossic and A. Magnin. Drag and stability of objects in a yield stress fluid. *AIChE journal*, 47(12):2666–2672, 2001.

[31] O. Merkak, L. Jossic, and A. Magnin. Spheres and interactions between spheres moving at very low velocities in a yield stress fluid. *J. Non-Newtonian Fluid Mech.*, 133(2-3):99–108, 2006.

[32] B. T. Liu, S. J. Muller, and M. M. Denn. Convergence of a regularization method for creeping flow of a bingham material about a rigid sphere. *J. Non-Newtonian Fluid Mech.*, 102(1-3):179–191, 2002.

[33] M. Beaulne and E. Mitsoulis. Creeping motion of a sphere in tubes filled with herschel–bulkley fluids. *J. Non-Newtonian Fluid Mech.*, 72(1):55–71, 1997.

[34] R. P. Chhabra. *Bubbles, Drops, and Particles in Non-Newtonian Fluids*. CRC press, 2007.

[35] N. P. Chafe and J. de Bruyn. Drag and relaxation in a bentonite clay suspension. *J. Non-Newtonian Fluid Mech.*, 131(1-3):44–52, 2005.

[36] H. Tabuteau and et al. Drag force on a sphere moving through an aging system. *The European Physical Journal E*, 22(4):337–341, 2007.

[37] B. J. Briscoe, M. Glaese, P. F. Luckham, and S. Ren. The falling of spheres through bingham fluids. *Colloids and Surfaces A: Physicochemical and Engineering Aspects*, 65 (1-2):69–75, 1992.

[38] D. Bonn and M. Denn. Yield stress fluids slowly yield to analysis. *Science*, 324(5928): 1401–1402, 2009.

[39] S. M. Fielding, P. Sollich, and M. E. Cates. Aging and rheology in soft materials. *Journal of Rheology*, 44(2):323–369, 2000.

[40] G. Yin and M. J. Solomon. Soft glassy rheology model applied to stress relaxation of a thermoreversible colloidal gel. *Journal of Rheology*, 52(4):785–800, 2008.

[41] R. P. Chhabra. *Bubbles, drops, and particles in non-Newtonian fluids*. CRC press, 2006.

[42] J.-M. Piau. Carbopol gels: Elastoviscoplastic and slippery glasses made of individ-

ual swollen sponges: Meso-and macroscopic properties, constitutive equations and scaling laws. *Journal of non-newtonian fluid mechanics*, 144(1):1–29, 2007.

[43] P. Lefrançois, E. Ibarboure, B. Payré, E. Gontier, J.-F. Le Meins, and C. Schatz. Insights into c arbopol gel formulations: microscopy analysis of the microstructure and the influence of polyol additives. *Journal of Applied Polymer Science*, 132(46), 2015.

[44] P. Coussot. Yield stress fluid flows: A review of experimental data. *Journal of Non-Newtonian Fluid Mechanics*, 211:31–49, 2014.

[45] V. Vitali, G. Nava, A. Corno, M. Pezzotti, F. Bragheri, P. Paiè, R. Osellame, M. A. Ortenzi, I. Cristiani, P. Minzioni, et al. Yield stress "in a flash": investigation of nonlinearity and yielding in soft materials with an optofluidic microrheometer. *Soft Matter*, 17(11):3105–3112, 2021.

CHAPTER 4

Large field-of-view heterogeneity maps

4.1 Introduction

From an industrial perspective, material uniformity is often perceived as the outcome of a well-designed process. However, many consumer products, such as skin creams and toothpaste, exhibit complex microstructures with local compositional and rheological properties that can vary significantly across 0.1-1 mm length scales. Contrary to conventional assumptions, these rheological heterogeneities often contribute positively to both the appearance and performance of these products[1–4]. Moreover, in industrial process development, a scale-up problem often occurs: the development of a product is done with pilot scale processing, producing a limited quantity of prototype products and then the process is changed to produce large quantities at manufacturing scale. During scale-up it is important to maintain the same resulting properties and quality of the product, which is correlated with its microstructure.

Several approaches are available to analyze the microstructure and particle size in a given sample at different scales[5,6], from Static and Dynamic Light Scattering (SLS, DLS)[7,8] or X-ray diffraction[9,10] for the nm scale up to granulometry for the mm scale. However, in situations when the system contains substantial aggregates or interaction among nano- micro-particles, light scattering data interpretation is difficult. Video-based microscopy techniques are attractive in such situations because they provide a more direct and reliable way to gain insights on the sample microstructure.

Indeed, video-based microrheological techniques for studying rheological heterogeneities in soft materials[6,11–13] have advanced our understanding of how formulation and processing decisions impact the final properties (e.g., viscosity, yield stress) and behaviors (e.g., stability, spreadability) of complex soft matter systems.

For example, this methodology has been employed in studies aiming at classifying Carbopol microgel suspensions[11]. Tracking the Brownian motion of tracers, the authors were able to unveil the presence of heterogeneities in a model aqueous dispersion of Carbopol, which they attributed to the microgel polymer preparation process. However, the limited field of view imposed by the high magnification, required to achieve the space resolution to track Brownian motion and infer viscoelastic behavior, limits the ability to explore rheological heterogeneity beyond 10-100 μm length scales. This limitation motivates us to seek an approach able to extend the observed length scale, to gain quantitative information on rheological heterogeneity at larger length scales.

We propose here a simple approach that fills this gap based on low-magnification microscopy, tracking of dispersed tracers, and effective classification of the prevailing regimes of motion in sample regions following a weak pressure gradient induced within the sample. In this chapter, we present measurements on weak gel obtained with Stabylen 30[14,15], a common thickener polymer in industry, and different Carbopol samples. We

quantify the impact of different preparation protocols on rheology and microstructure and we highlight how heterogeneity in the range of 100-1000 μm can be used to control the final texture of formulated products.

4.2 Materials and methods

4.2.1 Sample preparation

For this study, water-based yield stress fluids composed of Acrylates/Vinyl Isodecanoate Crosspolymer, a cross-linked acrylic polymer with enhanced lipophilic characteristics, commonly known as Stabylen 30, were received by 3V Sigma US and used as received. Our investigation focused on two main objectives: evaluating the effect of different preparation procedures on the mesostructured samples and comparing the properties of lab-scale samples with those produced at the plant scale to address industrial demands.

We compare four distinct powder incorporation processes; two of the processes are performed at the "pilot scale", the learning scale for industrial processes, used during the research and development phase of a project. The other two processes are the relative manufacturing scale used for industrial production.

The utilized equipment was from two different suppliers:

The Quadro, pilot scale HV0 model mill was purchased from Quadro USA (High Shear Mixer Manufacturer | Quadro Liquids). It allows the continuous addition of powder ingredients to a liquid stream. To optimize the dispersion of the powder, it employs a rotor-stator mill with a gap of >1 mm, considered "large gap" in this study. With a motor power of about 5.5 kW, Quadro is considered in this study a pilot scale unit, used in research and development environments, with a maximum flow capacity of 9.5 l/min. The Manufacturing scale version is the model HV3 with a motor power of 44 kW and a maximum flow rate of 280 gallons/min.

The dry blender, pilot scale model AC+2116 mill was purchased from Ampco USA. It allows the continuous addition of powder ingredients to a liquid stream. To optimize the dispersion of the powder, it employs a rotor-stator mill with a gap <1 mm, considered a "small gap" in this study. With a motor power of 5 Horse Power, the dry blender is considered in this study a pilot scale unit, for research and development use, with a maximum flow rate capacity of ~37 gallons/min. The manufacturing scale, Model AC+4329, has a 22 kW motor and a maximum flow rate of 460 l/min.

For simplicity, we will refer to the different processes as:

- **Small gap mill pilot scale:** Quadro pilot scale powder incorporation system 6000 RPM, 8 liters per min flow rate. 100 g/min powder dosing;
- **Large gap mill pilot scale:** Dry blender pilot scale powder incorporation system 8000 RPM, 8 liters per min flow rate. 100 g/min powder dosing;
- **Small gap mill manufacturing scale:** Quadro manufacturing scale powder incorporation system 5000 RPM, 250 liters per min flow rate. 100 g/min powder dosing;
- **Large gap mill manufacturing scale:** Dry blender manufacturing scale powder incorporation system 6800 RPM, 250 liters per min flow rate. 100 g/min powder dosing

Four solutions of Stabylen 30 thickening polymer were prepared in water with the same concentration, 0.5% w/w Stabylen 30 and 99.5% DI water, with the different protocols.

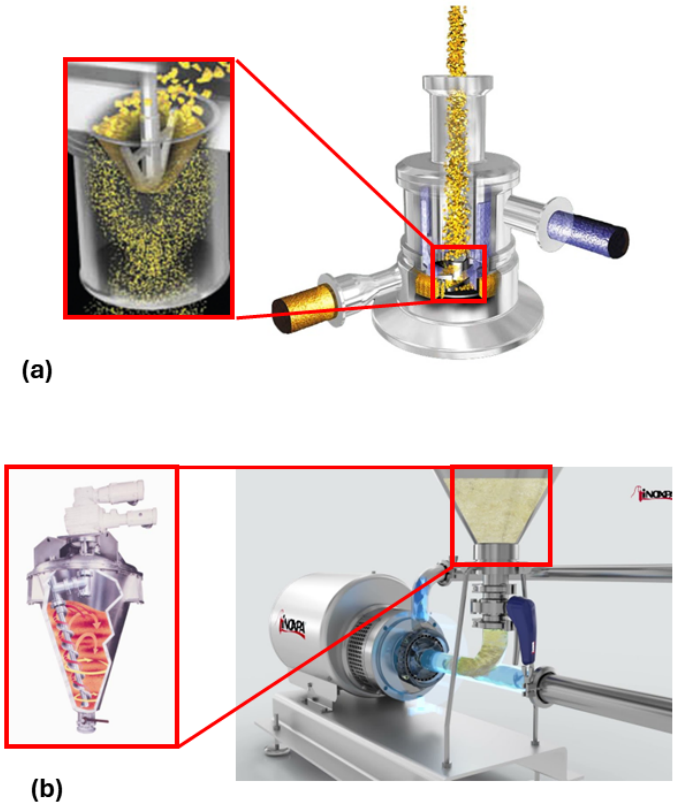

Figure 4.1: Schematic representation of two mixing methods: (a) small-gap mill (Quadro) and (b) large-gap mill (dry blender).

The typical concentration at which it is commonly used in many products because of its yield stress and viscoelastic properties. To further validate our proposed approach, Carbopol® 971P NF Polymer, Carbopol® 974P NF Polymer, and Carbopol® Ultrez 20 Polymer samples were also prepared as discussed in Chapter 1 and used as reference materials.

4.2.2 Bulk rheology of Stabylen 30

To standardize system evaluation, a flow curve test was performed using a DHR3 stress-controlled rheometer from TA Instruments, equipped with a cone and plate geometry (60 mm radius, 1 degr angle). The temperature control is provided by the plate. Steady-state viscosity measurements were performed on a shear rate ($\dot{\gamma}$) range of 0.001 to 100 s^{-1}. For each measurement point, the instrument verifies the steady state by repeating the measurement of the average stress over a 3 s interval for consecutive intervals. The measurement point is accepted if the average stress remains within a 2% variation over 3 consecutive intervals. The resulting flow curves (shear stress versus shear rate) were analyzed to determine viscosity as a function of shear rate and to identify any yield stress or non-Newtonian behavior.

In this study, we are especially interested in the effect of the sample preparation process on the final rheological properties of Stabylen 30 formulations and dense microgel systems. The expected microstructure for the 4 samples of 0.5% w/w Stabylen 30 in water is a jammed microgel system in which the polymer microgel particles volume fraction exceeds the random close packing, inducing the kinetic arrest of the system with the resulting onset of yield stress. However, the rheological properties are significantly influenced by sample heterogeneities, a direct consequence of the sample preparation method. Stabylen 30 exhibits shear-thinning behavior: high applied shear stress leads to microgel cluster fragmentation into smaller particles. On their turn, variations in cluster size distribution directly impact viscosity. The overall impact of cluster size distribution on bulk mechanical properties is not obvious and may depend on the specific properties of different systems. In microgels, increased ionic strength, which induces both shrinking and aggregation of microgels by screening electrostatic repulsion, has been reported to decrease viscosity [16]. However, in both colloidal and microgel suspensions, a positive correlation is in general observed between larger clusters and increased viscosities and elastic moduli of suspensions [6,17].

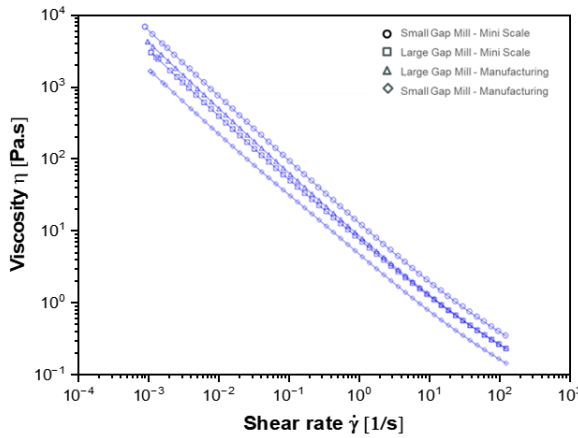

Figure 4.2: Flow curve, viscosity as a function of shear rate measured at room temperature for the 4 samples described. Note that the composition is the same for all samples, but the rheology varies significantly as a function of the processing equipment type and scale.

Rheometer data reveal viscosity variations across samples prepared using different scales (manufacturing vs. pilot scale in the small gap mill, see Figure 4.2). These differences clearly indicate variations in microstructure. Analysis of flow curves highlights these differences, emphasizing the critical influence of processing on the final rheological outcome. The near-identical rheological profiles observed at different scales in the Large gap mill suggest that the specific processing conditions while differing in scale, yielded comparable microstructures. The aim of the experimental characterization is to assess such correlation.

4.3 Microrheological mapping

4.3.1 Microscopy and imaging

A dilution process was applied to ensure that the samples did not exhibit characteristics of the jammed regime, crucial for tracer movement across the dense microgel layer. The concentration of Stabylen 30 was reduced 16-fold (Figure 4.3a), achieving a final concentration of 0.031 wt%. Although dilution is clearly affecting the bulk rheology, we observed that it allows to capture and preserve micro- and meso-structural features of the material, which would be otherwise hidden in concentrated samples. 0.05 wt% of 1.5 μm fluorescent polystyrene tracers were evenly dispersed within the diluted samples. The size of particles was chosen to be big enough to be easily detectable at low magnification, yet small enough to passively follow the solvent motion.

The samples were placed between two slides (Figure 4.3b,c), allowing stabilization of the upper slide for 2 minutes. In the following minutes, convective displacement of tracers in the accessible areas of the sample sets in, initiated by capillary forces. We utilized a Keyence VHX 7000 digital microscope that allows a large field of view, This process was recorded with the integrated video camera at 30 fps, producing a 60-second video.

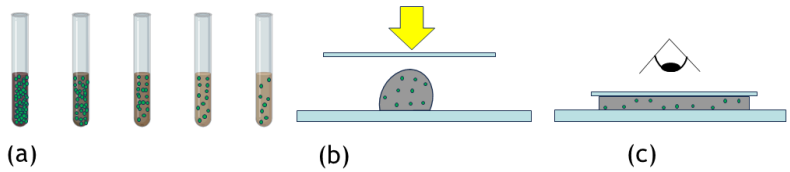

Figure 4.3: Schematic representation of the video microscopy experimental setup. The three steps are indicated: a) sample dilution b) microscopy slide loading c) video acquisition.

4.3.2 Particle tracking

The acquisition of time-resolved images for particle tracking yielded comprehensive insights into the sample's microstructure. Single frames reveal a homogeneous distribution of tracers within the transparent gel (Figure 4.4a). Care was taken to optimize the contrast of the tracers, as well as to get the best trade-off between space resolution and large field-of-view. Moreover, long exposure allows to highlight the overall motion of the tracers (Figure 4.4b). It is apparent in the Figure that certain areas are not reached by tracers, revealing structural heterogeneity.

4.3.3 Space-resolved dynamics

The combination of these image sequences with particle tracking algorithms allowed for in-depth analysis of particle motion in each video[18]. The main objective was to classify particle trajectories on the basis of their mean square displacement (MSD)[19,20]. As shown in Figure 4.5, tracers not only span the sample in a spatially heterogeneous way, but also display different types of motion. Indeed, a fraction of the particles, which we deem as trapped, display a fixed position, vibrating around it. Another group of particles, which we term diffusive, moves with linear scaling of MSD with time, possibly correlated to intermittent binding to clusters and diffusion in isolated portions of the

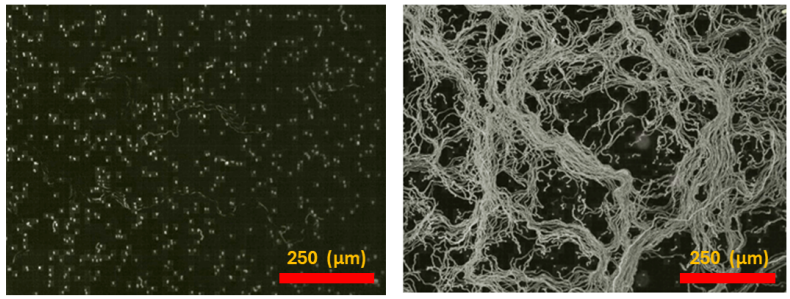

Figure 4.4: Example of microscopy video results for sample large gap mill– manufacturing scale: a) single frame showing the presence of tracers dispersed in the optically transparent gel, b) long exposure image from the same video showing the projection of all frames into a single frame showing the movement of the tracers. It is evident that some regions are inaccessible by tracers, indicating the presence of rheological constraints.

sample. A third fraction of tracers, termed ballistic, freely follow the streamlines in a persistent, viscous motion. The algorithm begins the process by generating a logarithmic plot that compares the MSD as a function of the lag time for each particle trajectory. The slope of the log-log plot is subsequently computed, and based on this slope, trajectories are classified into one of three separate groups (see colors in Fig. 4.5): trapped, with MSD slope = 0 0.5; diffusive, with MSD slope = 1 0.5; or ballistic, with MSD slope = 2 0.5. These categories provide a visual representation of the different modes of motion, with distinct MSD patterns, which reflect different microstructural features in the sample.

Subsequently, we plot all the trajectories followed by the particles, assigning a color determined by their motion type (Figure 4.6a), which helps to grasp the movement of particles in the system and makes it easier to identify areas with unique motion characteristics. However, several trajectories may overlap.

Therefore, to explore and visualize the microstructure of the system, we use a method where each pixel acts as a local rheology indicator in a 2D map. We count the classified trajectories passing through each pixel and assign distinct RGB colors based on their occurrence. This color map graphically represents the spatial arrangement of different regimes of motion and indicates the rheological variation within the sample, from the most accessible to the most inaccessible regions (Figure 4.6b). The areas inaccessible to tracers or characterized by trapped particles indicate the presence in the samples of gel regions; with this approach, we can also estimate their size distribution.

4.3.4 Validation

While our proposed technique does not directly characterize the microstructure of microgels, it can quickly estimate gel domain sizes in the samples and reveal new insights into the structure at the mesoscale. Indeed, we could observe microgel clusters reaching sizes over a hundred micrometers, which are often overlooked by traditional approaches for different reasons: bulk rheology requires a gap size much larger than the largest building blocks of the material but is typically limited to tens of microns; instead, typical video-based microrheology requires high magnification to obtain good resolution, at the cost of a reduced field-of-view.

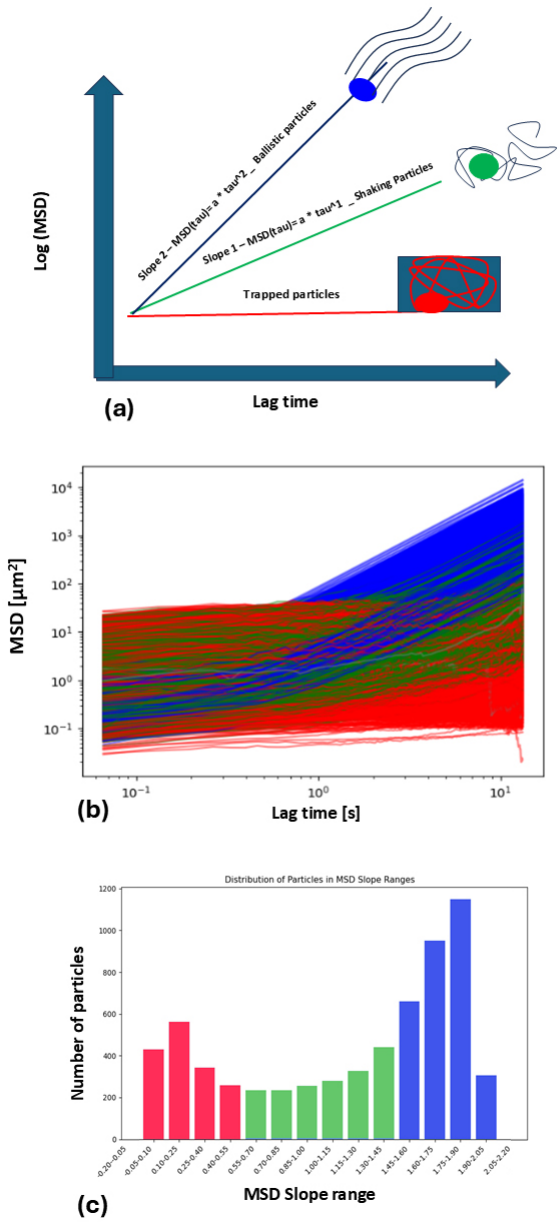

Figure 4.5: (a): An illustration of how tracers were classified into three categories (b): Classified MSD of tracers versus lag times, (c) Histogram of MSD exponents.

Moreover, it is worth noting that the proposed approach is based on the power law exponent of tracers' MSD, which is not influenced by the absolute velocity. This strategy is particularly advantageous for investigating fluids spanning very different viscosities: higher viscosities only require the acquisition of longer videos, but the classification cri-

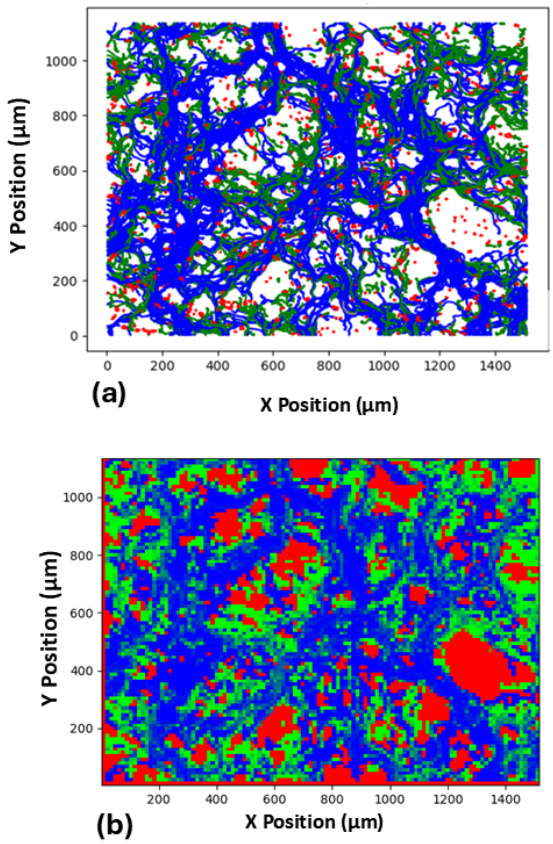

Figure 4.6: (a) Classified particle trajectory map based on MSD slope for Stabylen 30 made in a large gap mill – manufacturing scale. White regions: inaccessible area, Red regions: trajectories of trapped particles, green regions: trajectories of diffusive particles, blue regions: trajectories of ballistic particles. (b) Heterogeneity map: The color pixel map is displayed as a gradient that transitions from red to blue, organized in increasing order from the least flexible to the most flexible area.

teria do not change.

However, several parameters require accurate control and testing, to ensure the robustness of our analysis. For instance, the right extent of sample dilution is essential to allow tracer movement without losing access to structural features, and sufficient tracer concentration is necessary for adequate resolution of the reconstructed maps. Proper timing of acquisition can also be critical because a 2 minute delay allows for most of the strong internal flows, due to the mechanical stress upon sample squeezing, to relax.

Separate channels for tracer trajectories

To better understand the role of different tracer populations, each family of trajectories was plotted separately (see Figure 4.7). These single-channel maps reveal that trapped (red) particles are localized rather homogeneously throughout the whole sample, except in some regions, which are almost empty. A few particles occasionally appear in such

inaccessible regions, probably trapped between the sample and the substrate. Diffusive (green) tracers are mostly present at the boundaries of the red regions, possibly corresponding to an exchange between the trapped population and the freely moving ones. Ballistic (blue) particles form "rivers" of persistent flow permeating through the sample.

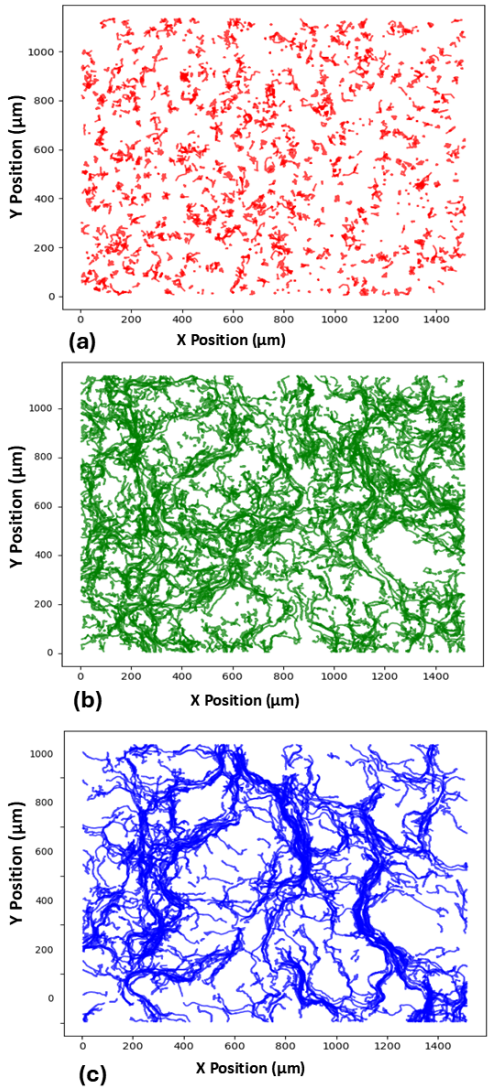

Figure 4.7: Separate classified trajectory maps: (a) Trapped particles in red, (b) Diffusive particles in green, (c) Ballistic particles in blue.

Time dependence

Various time intervals were examined within the same sample after the first 2 minutes to verify the consistency of the proposed analysis and its possible time dependence and to

determine the optimal acquisition length. Initially, the proportion of constrained tracers is higher, decreasing over time as the number of diffusive and ballistic tracers increases (Figure 4.8). Around 140 seconds, the relative population fractions stabilize, indicating that from that time on the analysis reflects the steady state behavior. Shorter acquisitions may misinterpret regions due to insufficient observation time.

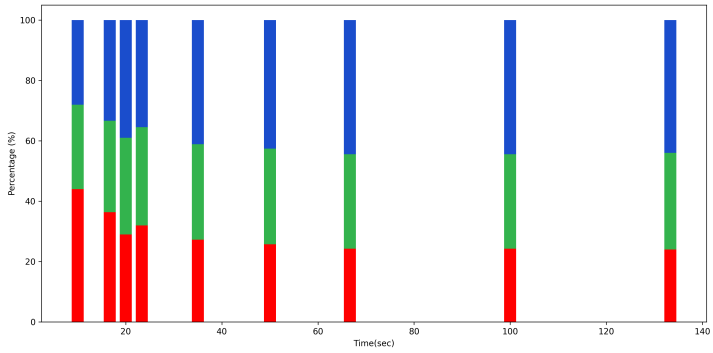

Figure 4.8: Percentage of trajectories over time, classified as trapped (red), diffusive (green) and ballistic (blue).

Reproducibility

To evaluate the reproducibility of the method, a single sample (Carbopol C971 Nf 0.05% wt) was tested multiple times. Figure 4.9 shows quantitatively similar, although not identical, heterogeneity maps upon repetition, with consistent size distributions.

4.4 Microstructural heterogeneity mapping

4.4.1 Stabylen 30

Heterogeneity maps were extracted for Stabylen 30 samples at the same concentration but with different preparation protocols, as shown in Figure 4.10. The clear difference among the maps is best captured by considering the size distributions of microgel clusters, which display significant variations depending on the adopted protocol. We can confirm that Stabylen 30 exhibits strong shear sensitivity, as the polymer microgel clusters get fragmented into smaller sizes upon exposure to high-stress processes. At the same time, a clear pattern in viscosities emerges from bulk rheology measurements (flow curves in Figure 4.2): with the small gap mill method, the viscosity of the pilot scale is significantly larger than in the manufacturing scale. On the contrary, the Large gap mill produces nearly identical results at two distinct scales. Microrheology mapping can provide some insights about the microstructural origin of the viscosity variation: small gap mill samples exhibit a marked decrease in average cluster size when scaling the protocol from pilot- to manufacturing scale, from 330 μm to 80 μm, impacting the material's overall rheology (see Figure 4.10). Conversely, the Large gap mill samples are characterized by similar average cluster sizes.

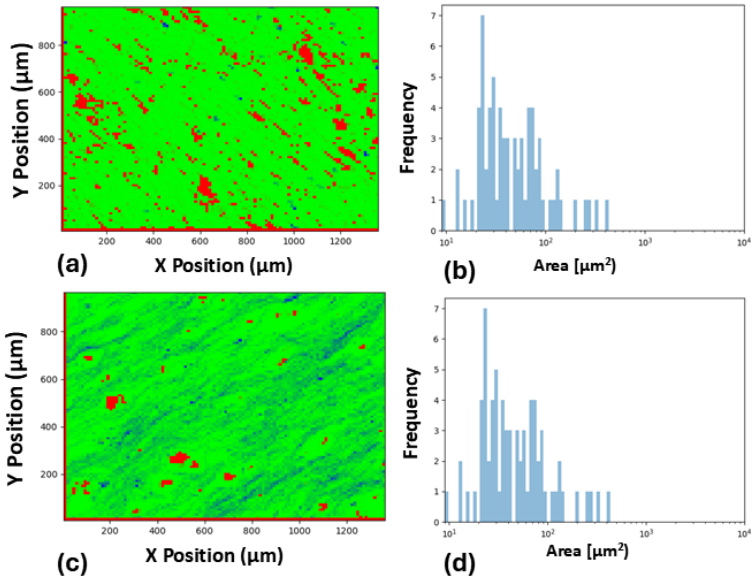

Figure 4.9: Carbopol 971NF and its distribution of sizes, same sample repeated two times.

4.4.2 Carbopol

Different microgel types within the Carbopol family can yield significantly different rheological performance, which may be beneficial or detrimental for a given application. We tested the ability of the proposed heterogeneity maps to quantify structural differences at the mesoscopic scale. In particular, we compared Carbopol 971 NF and Ultrez 20 at 0.5 wt%, which display rather different flow curves (Figure 4.11). After 10-fold dilution, down to 0.05 wt%, heterogeneity maps were extracted for the two samples (Figure 4.12).

Also in this case, the cluster size distributions show a direct correspondence with bulk rheology. Ultrez 20, the sample with larger viscosity, also exhibits larger aggregates than C971 NF at the same concentration and with the same preparation protocol.

4.5 Conclusions

We have proposed and validated a simple approach to evaluate large-scale heterogeneity, based on tracking of dispersed tracers and classifications of sample regions according to the time dependence of the mean square displacement of tracers, from trapping to diffusion to persistent flow. This method offers a straightforward and efficient means to assess the heterogeneity of different microstructures, particularly in systems with complex features that are difficult to interpret. We have employed this technique to rationalize the observed bulk rheology variation in a set of samples with the same composition but prepared with different processes. Indeed, we find a good correlation between the observed drop in viscosity induced by high-shear, and microstructural heterogeneity.

Application to Carbopol samples further validated the ability of microrheology-based

maps to reconduct measured differences in rheology behavior to different microstructural counterparts. The method could overcome the limitations of traditional rheology and microscopy techniques, providing a rapid and insightful assessment of mesoscale heterogeneity crucial for optimizing industrial processes and predicting product performance.

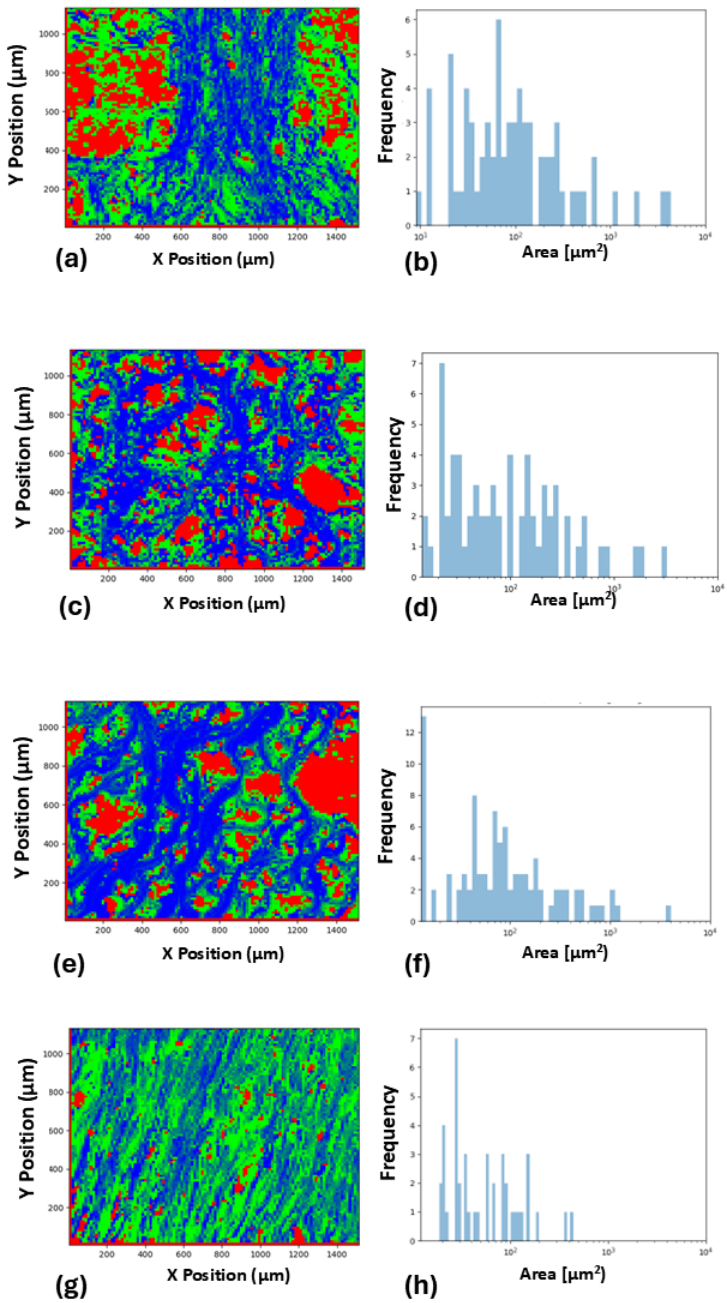

Figure 4.10: Heterogeneity maps and size distributions of inaccessible areas. (a, b) Mini-scale small-gap mill (average size: 338.56 μm). (c, d) Mini-scale large-gap mill (average size: 202.90 μm). (e, f) Manufacturing-scale large-gap mill (average size: 333.13 μm). (g, h) Manufacturing-scale small-gap mill (average size: 77.19 μm). The results illustrate the influence of mill type and scale on the size and distribution of inaccessible areas.

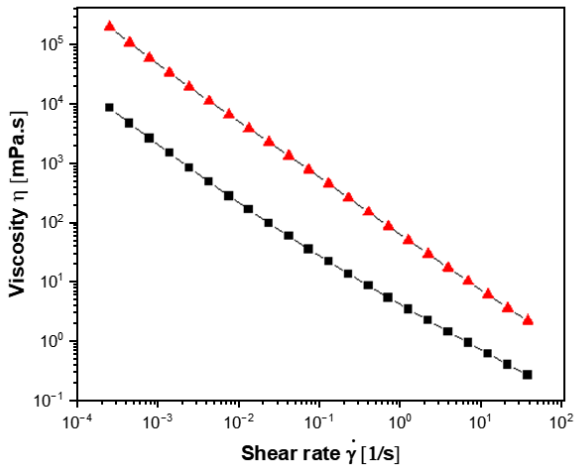

Figure 4.11: Shear viscosity (η) vs. shear rate ($\dot{\gamma}$) for 0.5 wt% aqueous suspensions of Carbopol 971 NF (black square) and Ultrez 20 (red triangle) at 25°C.

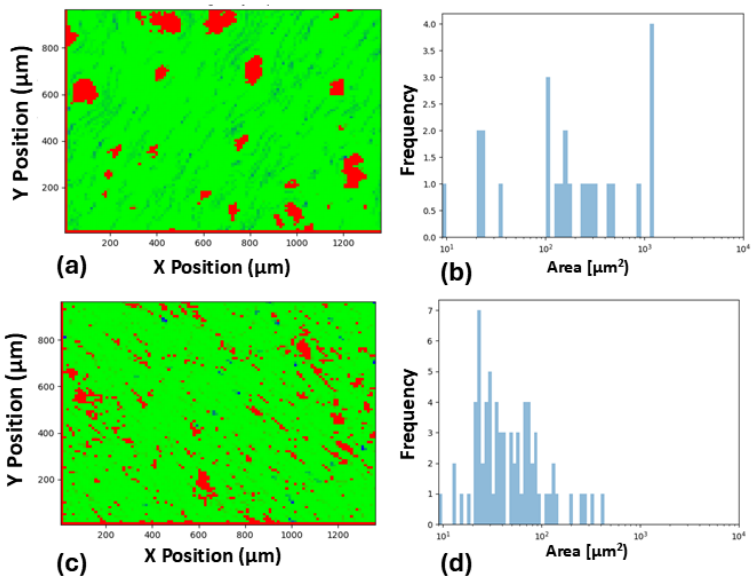

Figure 4.12: Heterogeneity maps and size distributions of inaccessible areas. (a) and (b): Ultrez 20 0.05%wt and its cluster size distribution; (c) and (d): Carbopol 971NF and its cluster size distribution.

Bibliography

[1] I. A. Gutowski, D. Lee, J. R. de Bruyn, and B. J. Frisken. Scaling and mesostructure of carbopol dispersions. *Rheologica acta*, 51:441–450, 2012.

[2] J.-Y. Kim, J.-Y. Song, E.-J. Lee, and S.-K. Park. Rheological properties and microstructures of carbopol gel network system. *Colloid and Polymer Science*, 281(7): 614–623, 2003.

[3] E. Younes, M. Himl, Z. Stary, V. Bertola, and T. Burghelea. On the elusive nature of carbopol gels: "model", weakly thixotropic, or time-dependent viscoplastic materials? *Journal of Non-Newtonian Fluid Mechanics*, 281:104315, 2020. doi: 10.1016/j.jnnfm.2020.104315.

[4] R. Graziano, V. Preziosi, D. Uva, G. Tomaiuolo, B. Mohebbi, J. Claussen, and S. Guido. The microstructure of carbopol in water under static and flow conditions and its effect on the yield stress. *Journal of Colloid and Interface Science*, 582: 1067–1074, 2021. doi: 10.1016/j.jcis.2020.09.003.

[5] M. Caggioni, P. Spicer, D. Blair, S. Lindberg, and D. Weitz. Rheology and microrheology of a microstructured fluid: The gellan gum case. *Journal of Rheology*, 51(5): 851–865, 2007.

[6] C. Oelschlaeger, J. Marten, F. Péridont, and N. Willenbacher. Imaging of the microstructure of carbopol dispersions and correlation with their macroelasticity: A micro- and macrorheological study. *Journal of Rheology*, 66(4):749–760, 2022. doi: 10.1122/8.0000452.

[7] D. Lee, I. A. Gutowski, A. E. Bailey, L. Rubatat, J. R. de Bruyn, and B. J. Frisken. Investigating the microstructure of a yield-stress fluid by light scattering. *Physical Review E—Statistical, Nonlinear, and Soft Matter Physics*, 83(3):031401, 2011.

[8] J.-M. Piau. Carbopol gels: Elastoviscoplastic and slippery glasses made of individual swollen sponges: Meso-and macroscopic properties, constitutive equations and scaling laws. *Journal of non-newtonian fluid mechanics*, 144(1):1–29, 2007.

[9] S. Sahoo, C. Chakraborti, S. Naik, S. Mishra, and U. Nanda. Structural analysis of ciprofloxacin-carbopol polymeric composites by x-ray diffraction and fourier transform infra-red spectroscopy. *Tropical Journal of Pharmaceutical Research*, 10(3), 2011.

[10] J. R. Retama, B. Lopez-Ruiz, and E. Lopez-Cabarcos. Microstructural modifications induced by the entrapped glucose oxidase in cross-linked polyacrylamide microgels used as glucose sensors. *Biomaterials*, 24(17):2965–2973, 2003.

[11] J. Liang, F. Teng, T.-M. Chou, and M. Libera. Measuring microgel swell ratio by cryo-sem. *Polymer*, 116:1–4, 2017. doi: 10.1016/j.polymer.2017.03.050.

[12] M. J. Garcia-Salinas and A. M. Donald. Use of environmental scanning electron microscopy to image poly (n-isopropylacrylamide) microgel particles. *Journal of colloid and interface science*, 342(2):629–635, 2010. doi: 10.1016/j.jcis.2009.10.064.

[13] J. Liang, X. Xiao, T.-M. Chou, and M. Libera. Analytical cryo-scanning electron microscopy of hydrated polymers and microgels. *Accounts of Chemical Research*, 54 (10):2386–2396, 2021. doi: 10.1021/acs.accounts.1c00109.

[14] D. V. Belsito, R. A. Hill, C. D. Klaassen, D. Liebler, J. G. Marks Jr, P. D. Heldreth, P. D. Ivan Boyer, and C. Senior Toxicologist. Crosslinked alkyl acrylates as used in cosmetics. 2011.

[15] M. M. Fiume, B. Heldreth, I. Boyer, W. F. Bergfeld, D. V. Belsito, R. A. Hill, C. D. Klaassen, D. C. Liebler, J. G. Marks Jr, R. C. Shank, et al. Safety assessment of cross-linked alkyl acrylates as used in cosmetics. *International journal of toxicology*, 36(5_suppl2):59S–88S, 2017.

[16] Z. Shao, A. S. Negi, and C. O. Osuji. Role of interparticle attraction in the yielding response of microgel suspensions. *Soft Matter*, 9(22):5492–5500, 2013.

[17] C. Weis, C. Oelschlaeger, D. Dijkstra, M. Ranft, and N. Willenbacher. Microstructure, local dynamics, and flow behavior of colloidal suspensions with weak attractive interactions. *Scientific reports*, 6(1):33498, 2016.

[18] F. Hering, M. Merle, D. Wierzimok, and B. Jähne. A robust technique for tracking particles over long image sequences. In *Proc. of ISPRS Intercommission Workshop'From Pixels to Sequences', Zurich, March*, pages 22–24. Citeseer, 1995.

[19] N. Gal, D. Lechtman-Goldstein, and D. Weihs. Particle tracking in living cells: a review of the mean square displacement method and beyond. *Rheologica Acta*, 52: 425–443, 2013.

[20] J. Apgar, Y. Tseng, E. Fedorov, M. B. Herwig, S. C. Almo, and D. Wirtz. Multiple-particle tracking measurements of heterogeneities in solutions of actin filaments and actin bundles. *Biophysical journal*, 79(2):1095–1106, 2000.

CHAPTER 5

Motion of yield stress fluid droplets on lubricated surfaces

Droplets of yield stress fluids (YSF) hardly move on solid surfaces due to their high viscosity. The use of highly slippery lubricated surfaces can shed light on the mobility of YSF droplets, which include everyday soft materials, such as toothpaste or mayonnaise, and biological fluids, such as mucus.
The spreading and mobility of droplets of aqueous solutions of swollen Carbopol microgels, a model system for YSF, were studied on lubricant-infused surfaces. Dynamical phase diagrams were established by varying the concentration of the solutions and the inclination angle of the surfaces. Carbopol droplets deposited on lubricated surfaces could move even at low inclination angles. The droplets were found to slide because of the slip of the flowing oil that covered the solid substrate. However, as the descending speed increased, the droplets rolled down. Rolling was favored at high inclinations and low concentrations. A simple criterion based on the ratio between the yield stress of the Carbopol solutions and the gravitational stress acting on the Carbopol droplets was found to nicely identify the transition between the two regimes.

This chapter is based on a collaboration with the Laboratory of Physics of Surfaces and Interfaces (Department of Physics and Astronomy "G.Galilei", University of Padova), led by Prof. Giampaolo Mistura. In this work, I was responsible for the rheological characterization of the samples. The results were published as:

Mattia Carneri, Davide Ferraro, Afshin Azarpour, Alessio Meggiolaro, Sebastian Cremaschini, Daniele Filippi, Matteo Pierno, Giuliano Zanchetta, and Giampaolo Mistura
"Sliding and rolling of yield stress fluid droplets on highly slippery lubricated surfaces"
Journal of Colloid and Interface Science, Volume 644, 15 August 2023, Pages 487-495

5.1 Introduction

Wetting is one of the fundamental interfacial phenomena[1], which affects the shape and motion of liquid droplets on solid surfaces and fluid flows in confined geometries[2,3]. It is relevant in a wide range of applications in the biomedical, environmental and energy sectors. The influence of surface chemical composition and roughness has been extensively investigated for Newtonian liquids[4], with particular emphasis on the possibility of controlling wettability and obtaining superhydrophobic surfaces[5], but much less is known for more complex fluids and surfaces. A promising approach to omniphobicity is offered by lubricant-infused surfaces (LIS), made of textured materials imbibed with a low surface tension oil[6,7]. These bioinspired surfaces exhibit various unique properties attributed to their liquid-like and molecularly smooth nature, including excellent liquid

repellency, self-healing, anti-icing, anticorrosion, enhanced heat transfer and antibiofouling[3,8–13]. In particular, they enable low friction droplet motion although the presence of numerous phases, drop, lubricant, solid matrix and vapor, yields a rich tribological scenario[14–18]. Their slippery nature makes them the best candidate for the study of highly viscous non-Newtonian fluids, which barely move on solid surfaces[19]. Then, it is possible to investigate the coupling between dynamic wetting and the rich rheology of soft, structured fluids, such as polymeric solutions, surfactant solutions, gels, or packed microgels, which exhibit viscoelastic behavior in between simple viscous fluids and elastic solids, depending on the probed time scales or the forces at play[20,21]. Indeed, we recently reported[22] an unexpected oscillatory motion of viscoelastic droplets on LIS, despite the homogeneity of the surface and polymeric solution, which can be considered as a sort of novel Weissenberg effect for moving droplets[22].

A particular class of non-Newtonian fluids is represented by yield stress fluids (YSF), which include everyday soft materials such as toothpaste, shaving foam or mayonnaise, body fluids such as mucus, and much harder products such as concrete. Their common feature is that they can flow (that is, deform indefinitely) only if they are subjected to stress above a critical value; otherwise, they deform in a finite way, like solids[23]. It is rather common that suspensions of dispersed particles in a solvent behave as a yield stress fluid when the volume fraction occupied by the particles is above a critical value[24]. Their closed-packed, amorphous structures are responsible for their rheological behavior: the particles are jammed and can only flow past one another appreciably if a sufficiently high stress, greater than the yield stress, is applied[25]. This threshold can be identified by measuring the stress while applying a continuous shear deformation to the sample at a decreasing strain rate: a non-vanishing stress appears for YSF, which corresponds to a diverging viscosity. However, the motion of a concentrated dispersion depends not only on the bulk flow properties but also on the nature of the confining surfaces.

Aqueous suspensions of swollen Carbopol microgels and aqueous solutions of cross-linked Xanthan polymers are model systems for yield stress fluids, whose rheological properties have been extensively studied[23,25,26]. The flow characteristics of such materials are difficult to predict, as they involve permanently or transiently coexisting solid and liquid regions, which are generally impossible to locate a priori and have been scarcely investigated until recently[27]. Significant slip is observed in the spreading of Carbopol and Xanthan droplets on untreated glass surfaces[28], which is explained in terms of a repulsive electric interaction between the negative polymer chains and the negative surface charges in contact with aqueous solutions due to the dissociation of the terminal silanol groups. After the initial spreading phase, the motion stops and a mechanical equilibrium is reached, characterized by a stable contact angle. Contrary to what is observed with Newtonian fluids and what is expected from classical thermodynamics, the final contact angle increases with the size of Carbopol droplets[29]. If the spreading of a droplet occurs on a thin film of the same material, the Carbopol droplet reaches a final equilibrium shape once the driving stresses inside the droplet fall below the yield stress[30], in contrast to a Newtonian droplet that spreads continuously until a completely flat film is formed. If a YSF droplet is placed on a dry superhydrophobic surface, the resulting adhesive stress is similar in magnitude to the gravitational and yield stresses. This allows the motion of Xanthan droplets descending an inclined superhydrophobic surface to be clearly differentiated in pure rolling, sliding, and sticking by varying the surface inclination and Xanthan concentration[31]. Spreading LISs, in which the lubricant impregnates the surface micro-textures and covers them, can be designed to allow the mobility of the yield stress fluids that would otherwise be immobile under

the same flow conditions[32]. For example, Carbopol droplets, which are found to adhere to both flat hydrophobic and patterned superhydrophobic surfaces, move readily on a spreading LIS impregnated with silicone oil. In other words, a spreading LIS acts as a stable Newtonian lubricating layer with an effective viscosity that depends on the viscosity of the lubricating fluid and the aspect ratio of the microtexture. However, the nature of the motion of YSF droplets, for example, whether they slide or roll down from an inclined surface, has hardly been explored in the literature. The aim of this work is to fill this gap by providing a comprehensive picture of the mobility of YSF droplets on slippery lubricated surfaces within a wide range of yield stress values.

5.2 Materials and Methods

5.2.1 Lubricant infused surfaces (LIS)

As slippery surfaces, we prepared hybrid substrates formed by glass slides coated with an LIS. Standard glass microscope slides were cleaned with common detergents and rinsed in acetone and purified water baths. A $\sim$25 μm thick porous polytetrafluoroethylene (PTFE) membrane (Sterlitech Corporation) was placed on one face of the slide and wetted with ethanol: the evaporation of ethanol leads to capillary adhesion of the membrane to the slide[33]. With a dip coater (Kibron Inc. LayerX 274), the membrane attached to the slide was then infused with fluorinated oil (Fomblin PFPE Perfluoropolyether Y LVAC 06/6) having a viscosity of 120 mPa s at T = 20 °C, using the procedure reported in[18]. To ensure a controlled thickness of the liquid layer above the membrane of about 0.5 μm, the withdrawal velocity was set at 0.12 mm/min, see reference[22] for more details.

5.2.2 Yield stress fluids

Different yield stress fluids, based on swollen microgels, were prepared and characterized. Namely, we studied two aqueous solutions of the polyacrylic acid Carbopol Aqua SF2 and Carbopol 971 P NF (Lubrizol) at different polymer mass fractions. The two families differ in their typical microgel radius (about 0.25 and 2 μm, respectively) and in their yield stress values as a function of concentration[34]. Carbopol Aqua SF2 (SF2) samples were diluted to the final concentration in MilliQ water, from a concentrated batch solution at low pH. The pH gradually increased by adding drops of NaOH 10 M; around pH 7, the microgels swell and the solution becomes fully transparent, developing a yield stress above a concentration of approximately 0.2%[35]. Carbopol 971P NF (971P) is available in powder form. It was dispersed in MilliQ water at the final concentration. The pH of the solution was increased to 7 by adding drops of NaOH 10 M, resulting in a fully transparent yield stress fluid above 0.05%[36]. All samples were gently mixed for several days and the pH was monitored and adjusted to obtain homogeneous suspensions that allow imaging of internal tracers[36]. The density ρ of all the investigated solutions was close to that of water, while there are no reliable measurements of the surface tension γ of Carbopol suspensions reported in the literature[30]. We tried to measure it directly with the pendant drop method[37], but the droplet curvature, and therefore the derived γ, varied considerably over time and depended on the infusion rate; as a result, we obtained values within the range 48-68 mN/m. Consequently, droplets are expected to be cloaked by a thin lubricant film once they are deposited on silicone or fluorinated oil lubricated surfaces[14,38]. Finally, pure glycerol was used as a Newtonian reference for the motion of droplets on slippery lubricated surfaces.

The rheological tests of the YSF solutions were performed on a commercial rheometer (MCR 302, Anton Paar GmbH) using a cone and plate geometry with a cone radius and angle of 25 mm and 1°, respectively. The temperature was kept at 22 °C with a Peltier element. Fresh samples were loaded for each series of experiments and reproducibility was verified by repeating a single test several times. Samples were pre-sheared at high shear rates for hundreds of seconds and then left to rest for a similar time to guarantee reproducible and time-independent behavior. From oscillatory experiments at $\omega = 1$ rad/s at increasing amplitudes in the range of $0.1 - 400\%$, we estimated the limits of the linear viscoelastic regime; we then extracted the linear viscoelastic properties from small-amplitude oscillatory shear experiments in the frequency range $\omega = 0.1 - 100$ rad/s at strain $\gamma = 1\%$. To estimate the yield stress σ_{yield}, flow curve tests were performed by applying a constant strain rate, decreasing from 100 to 0.01 s^{-1}, using logarithmically increasing sampling times to guarantee steady-state conditions at all shear rates. Data below 0.1 s^{-1} were not considered, as they often revealed the appearance of slip at the interface. The stress data, shown in Figure 5.1, were fitted according to the three-component (TC) model[39], which provides both a clearer physical insight and a better description of the experimental data than the Herschel–Bulkley model[23]. However, the yield stress estimates of the two models and their dependence on concentration were always consistent. As reported in Table 5.1, for both Carbopol samples σ_{yield} increases roughly linearly with concentration in the investigated ranges; a similar dependence is observed for the low-frequency elastic modulus G.

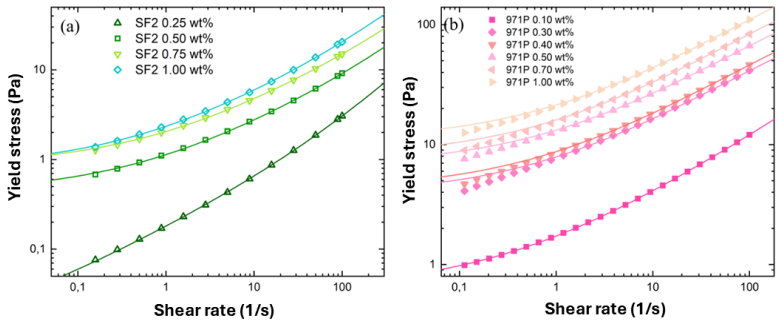

Figure 5.1: Shear stress σ vs. shear strain $\dot{\gamma}$ curves of Carbopol SF2 (a) and 971P (b) solutions on a log–log scale. The continuous curves show the corresponding three-component (TC) fits.

5.2.3 Optical setup

To monitor the motion of the droplets on the LIS, we used the optical setup shown in Figure 5.2[40]. A rotating stage controlled by a computer could change the angle of inclination with respect to the horizontal α of the lubricated substrate with 0.5°precision. A vertical syringe pump was mounted on an X-Y table. In this way, it was possible to dose droplets of known volume Ω in the range between 10 and 40 μl on a well-defined position of the substrate. To favor drop detachment, a short silicone tubing was attached to the tip of the stainless-steel needle. To minimize inertial effects, we slowly extruded the droplets onto the surface and placed the tubing tip 2 mm above the LIS. The lateral profile of the drop was viewed using a CMOS camera (BASLER acA800-510um) mounted along the rotation axis of the stage and equipped with a macro zoom lens (LINOS MeVis

Concentration (wt%)	σ_{yield} (Pa)	G′ (Pa)
Carbopol SF2		
0.25	0.2 ± 0.1	3 ± 1
0.50	0.6 ± 0.1	8 ± 1
0.75	0.7 ± 0.1	10 ± 1
1.00	1.2 ± 0.1	15 ± 1
Carbopol 971P		
0.10	0.6 ± 0.1	5 ± 1
0.30	3.8 ± 0.1	25 ± 2
0.40	4.2 ± 0.1	27 ± 2
0.50	6.7 ± 0.1	44 ± 2
0.70	7.9 ± 0.1	48 ± 2
1.00	10.8 ± 0.1	66 ± 2

Table 5.1: Main rheological properties of the Carbopol yield stress fluids.

C 50mm/f 1.8). To enhance the optical contrast, the droplet was backlighted with a white LED source. Movies of the drop motion were acquired at sample rate intervals between 100 and 2000 fps and analyzed using a custom-made LabVIEW script.

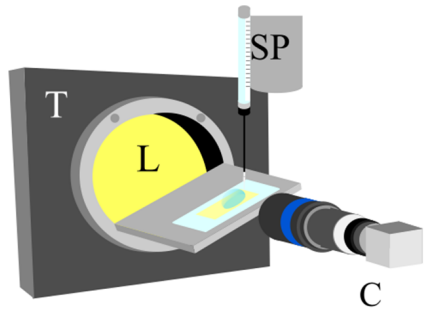

Figure 5.2: Optical setup: T=tilter, L=LED source, SP=syringe pump, C=camera.

5.3 Results

5.3.1 Droplet spreading

Figure 5.3 shows the time evolution of the droplet profile as derived from video recordings of the formation and deposition of droplets of volume $\Omega = 20\ \mu$l on a horizontal LIS. The graph in Figure 5.3(a) indicates the diameter D of the wetted surface, together with some representative snapshots of the initial and final profiles, while Figure 5.3(b) reports the corresponding contact angle θ. The initial time corresponds to the detachment of the droplet from the needle at the completion of the infusion process, which typically takes a few seconds. In the case of glycerol, the droplets reach the final configurations almost instantaneously. Instead, droplets of both Carbopol solutions exhibit a slow but significant expansion of the wetted area, accompanied by a decrease in the contact angle: in the case of SF2 0.50 wt%, the relative increase in D is greater than 10% over 5 minutes.

Varying the syringe flow rate between 0.06 and 0.54 ml/min did not produce any significant variation. In all experiments presented in the following, the extrusion flow rate was 0.3 ml/min, comparable to that used in a recent study[30].

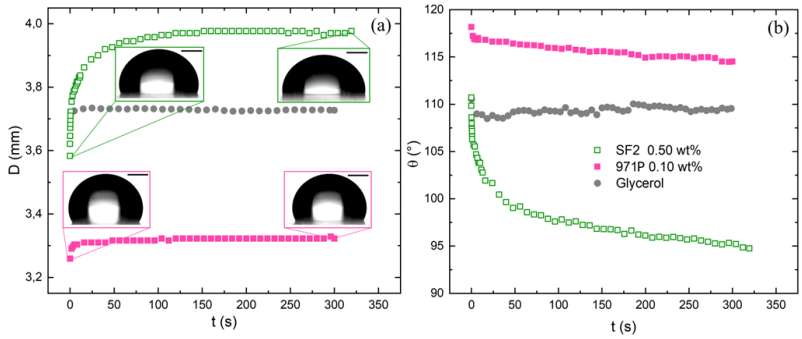

Figure 5.3: Temporal variation of the diameter D of the wetted area (a) and the corresponding contact angle θ (b) of different droplets of volume 20 μl deposited on a horizontal LIS. The scale bar of the four representative snapshots of the droplet contour is 1 mm.

The spreading of Carbopol droplets depends on their concentration, as shown in Figure 5.4. Interestingly, the two types of Carbopol present significant differences. In the case of SF2, the pronounced variation observed in D is related to the corresponding decrease in θ as the solution becomes more concentrated. Actually, the continuous lines in Figure 5.4(a) represent the diameter of the area wetted by a hemispherical cap of volume Ω and an instantaneous contact angle θ for selected Carbopol concentrations[41]. In the beginning, the lines lie below the corresponding experimental data, but eventually, they nicely overlap, suggesting that the initial shape assumed by the SF2 droplets is somewhat peaked and slowly relaxes to that of a perfect hemisphere. The good agreement between the experimental data and the geometrical calculations[41] implies that the observed phenomenology is mainly an interfacial effect: SF2 droplets spread until the contact line becomes pinned by surface tension, with D reaching different final values as a result of the different contact angles. A quite distinct behavior is observed in the case of 971P droplets. The three solutions have the same θ, yet D decreases significantly with concentration, suggesting that its dependence is primarily rheological. Indeed, this behavior is similar to that reported in the spreading of Carbopol drops over a thin film of the same material, where, as the yield stress increases, the final radius becomes correspondingly smaller[30]. This can be explained by assuming that the spread of a droplet, yielding under the effect of capillary and gravitational stresses, stops as they fall below the yield stress σ_{yield}.

Apart from these differences, for both types of solution, the time constant t_f required to reach the final configuration decreases with concentration: for example, t_f is equal to approximately 5 minutes for SF2 0.25 wt% and drops to 30 s for SF2 1 wt%. Furthermore, t_f is significantly shorter for 971P droplets: for 971P 0.10 wt% ($\sigma_{yield} = 0.63$ Pa), t_f is approximately 10 s, while for SF2 0.50 wt%, possessing a similar threshold value ($\sigma_{yield} = 0.60$ Pa), t_f is approximately 50 s.

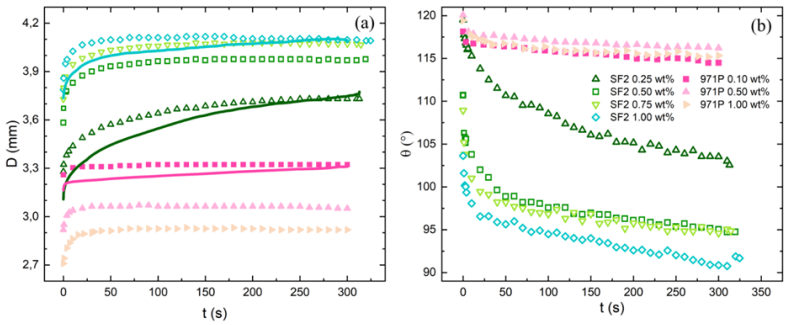

Figure 5.4: Temporal variation of the diameter D of the contact line (a) and the contact angle θ (b) of Carbopol drops at different concentrations and volume 20 μl deposited on a horizontal LIS. The continuous lines are the diameters of the wetted areas of hemispherical caps derived from the corresponding contact angles, as explained in the text.

5.3.2 Droplet motion

We have then studied the gravity-induced motion of Carbopol droplets on inclined surfaces. Figure 5.5 shows a representative set of consecutive measurements of SF2 0.25 wt% droplets deposited manually with a micropipette on a LIS inclined by an angle $\alpha = 3$ (empty symbols). The curves represent the temporal dependence of the front contact point of the descending droplets having $\Omega = 20$ μl. Clearly, the data show a set of quite different, non-linear curves that reflect the simultaneous relaxation processes following droplet generation and deposition, as discussed in the previous section. To remove this artifact, droplets generated with the syringe pump were gently deposited on a horizontal LIS. After a sufficiently long time to allow a complete stop of the spreading process, the LIS was quickly tilted to the same $\alpha = 3$, and the droplet motion was recorded. The resulting curves are indicated as full symbols in Figure 5.5. The straight lines indicate a viscosity dominated motion, as expected [14,15]. Small variations in their slope, less than 5%, can be taken as the degree of reproducibility of these measurements. All the measurements discussed in the rest of the section were taken following the latter procedure. We have considered only $\alpha \geq 3$ because, for smaller angles, the motion becomes very slow (velocity below approximately 0.01 mm/s) and the results may be affected by droplet evaporation. Actually, the height of the YSF droplets decreases by about 10% over 10 minutes, the minimum time required for the droplet to cover the length of the slide at $\alpha < 3$.

At low inclinations, Carbopol droplets are found to slide: the selected snapshots of Figure 5.6(a), which refer to a droplet of 971P 0.50 wt% and volume $\Omega = 20$ μl descending a lubricated surface inclined by an angle $\alpha = 10$. If instead α is increased above 20°, the droplets not only move faster, as expected, but also change the nature of the motion to rolling as shown in Figure 5.6(b), which corresponds to $\alpha = 45$: representative triangles that join three tracers rotate over time. From introductory mechanics, it is well known that a rigid sphere rolls down a rough inclined plane, while a rigid cube slides down it. In the case of a liquid drop, a variety of motions becomes possible because a deformable body maintains contact with the surface over a finite area [42], which have been theoretically analyzed in detail for the simple case of two-dimensional droplets [43–45]. For a viscous droplet, two distinct motions are typically observed. A nonwetting droplet on

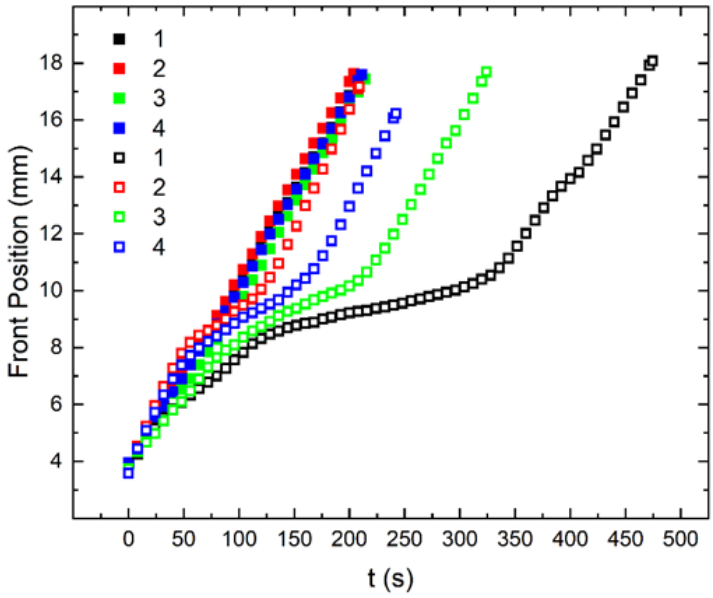

Figure 5.5: Time evolution of the front position of the contact line of four consecutive droplets of SF2 0.25 wt% with volume $\Omega = 20$ μl deposited on lubricated surfaces inclined by $\alpha = 3$. Empty symbols represent the motion of droplets deposited manually with a micropipette on the already tilted surface. The full symbols refer to droplets deposited on the horizontal surface using a syringe pump; after spreading, the surface is quickly tilted to $\alpha = 3$ and the resulting droplet descent motion is recorded.

a superhydrophobic surface rolls down[46,47] while, if the droplet partially wets a solid surface, it slides along it[48–50]. In the case of slippery lubricated surfaces, all studies of partially wetting Newtonian droplets indicate only rolling motion on LIS[14–16]. Carbopol droplets moving on LIS can instead undergo either sliding or rolling, depending on initial conditions such as Ω and α. Interestingly, low-concentration Carbopol droplets on lubricated surfaces exhibit the standard behavior observed with Newtonian droplets on LIS[14–16], that is, they roll down. For example, Figure 5.6(c) refer to droplets of 971P 0.10 wt% that descend from a LIS inclined to $\alpha = 10$. If we compare this sequence of snapshots with that of Figure 5.6(a), we clearly see that the less concentrated droplets not only move much faster (about a factor 30) due to their lower viscosity but also roll and do not slide. In summary, experimental evidence suggests that the change from sliding to rolling is a peculiar property of YSF droplets descending slippery surfaces. A somewhat similar behavior was reported in the case of much larger YSF drops, $\Omega = 250$ μl, made of Xanthan gum and descending a dry superhydrophobic surface[31]: sliding was observed at low inclinations, followed by rolling at higher α. Surprisingly, concentrated Xanthan droplets were pinned to superhydrophobic surfaces inclined to angles greater than ~ 10, while water droplets are very mobile on these surfaces: droplets as small as 1 μl easily roll down at inclinations of 1°. Instead, on lubricated surfaces, the sliding speed of YSF droplets with $\Omega = 20$ μl is comparable to that found with much larger drops, $\Omega = 250$ μl, on dry superhydrophobic surfaces, a clear indication that LISs

are much more slippery than superhydrophobic dry rough surfaces, ideal for the study of viscous non-Newtonian droplets.

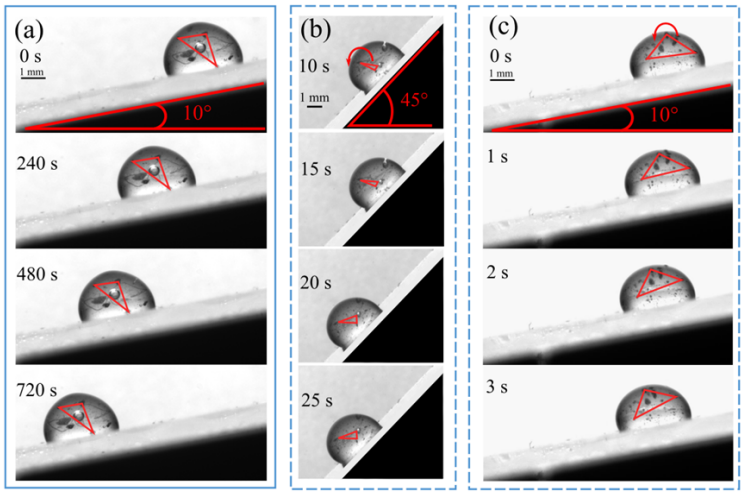

Figure 5.6: Snapshots of (a) sliding and (b) rolling of droplets of 971P 0.50 wt%: at 10°inclination, the air bubbles in the droplet show no relative motion inside of the droplet, indicating a sliding motion; at 45°inclination, the red triangle rotates indicating the rolling motion of the droplet. (c) Snapshots of droplets of 971P 0.10 wt% showing rolling at an inclination angle of 10°. All droplets have volume $\Omega = 20$ μl.

The dynamical phase diagrams shown in Figure 5.7 summarize the different types of motion exhibited by the descending droplets of the 971P and SF2 solutions, as the Carbopol concentration and the angle of inclination α vary. In the case of 971P droplets, as α increases, sliding is first observed, followed by rolling. Rolling is favored at high inclinations and low concentrations. Interestingly, the analogous phase diagram of SF2 droplets exhibits only rolling, in agreement with previous studies of Newtonian droplets on LISs. Next, we discuss these two regimes in more detail.

We first focus on the sliding regime, in which the 971P droplets do not undergo any shear. Figure 5.8 shows that the sliding droplets move downward with a steady velocity U that is proportional to $\sin\alpha$ for two representative 971P solutions, indicative of a typical Stokes behavior regulated by a constant viscosity and where U is due to the flow of the oil film that covers the filter. Consequently, we model the system as a solid droplet moving with velocity U separated by an oil film of thickness h from the filter, as schematically pictured in the inset of Figure 5.8. Given the expected small value of h, the flow profile in the oil film is $u(z) = Uz/h$, which yields a shear stress at the oil-droplet boundary $\sigma_{zx} = \mu_{oil}U/h$, where μ_{oil} is the oil viscosity. In stationary conditions, σ_{zx} must be equal to the gravitational stress $\sigma_{grav} = b\rho g \sin\alpha$, where b is the maximum height of the droplet having density ρ deposited on a LIS inclined by an angle α, and g is the acceleration of gravity[31]. A linear fit to the sliding data in Figure 5.8 provides an estimate of the oil film thickness h ~ 0.3 μm, in agreement with the value derived from dip coating. The fact that h is much larger than the intrinsic slip length of a few nm measured for Carbopol flowing past a solid wall[25] confirms that the sliding of the 971P

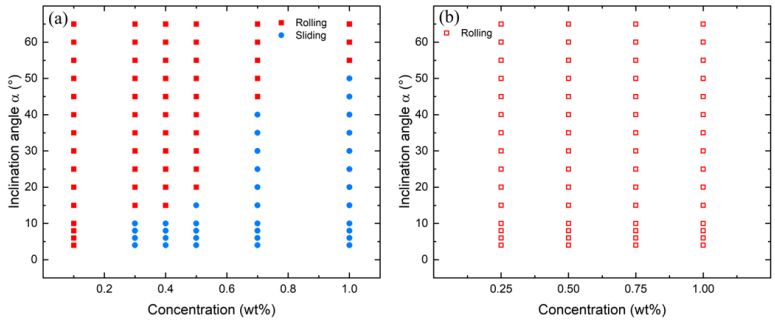

Figure 5.7: Dynamical phase diagrams of 971P (a) and SF2 (b) droplets at different concentrations moving on lubricated surfaces at different angles of inclination. The droplets have volume $\Omega = 20$ μl.

droplets is dominated by the slip caused by the flowing oil. This conclusion also agrees with the results of recent bulk experiments carried out with a conventional rheometer where Carbopol is confined between a flat plate and a spreading LIS[32]. The fact that, in the zoom of Figure 5.8(b), the 971P 1.0 wt% datapoints at high inclinations lie well above the extrapolated straight line may be an indication that at these velocities, and thus shear stresses, wall slip also contributes to the overall droplet velocity[51].

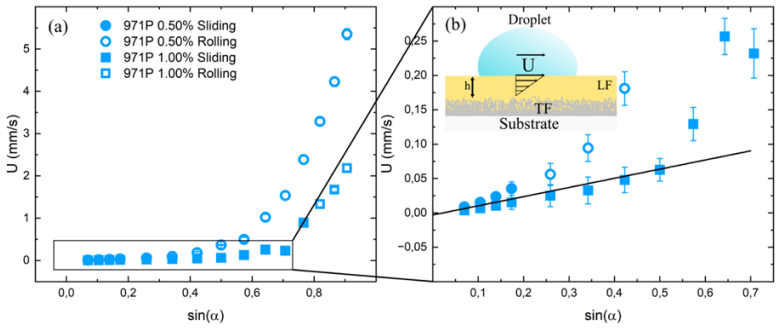

Figure 5.8: (a) Steady velocity of droplets of 971P at two different concentrations descending lubricated surfaces at different angles of inclination. The droplets have volume $\Omega = 20$ μl. (b) Enlargement of the data enclosed in the rectangular box. The inset shows a pictorial view of the interface between a droplet sliding with velocity U on a lubricant film LF of thickness h coating a Teflon filter TF infused with the same lubricant. This lubricant infused surface covers the glass slide S.

We now analyze under what conditions Carbopol droplets roll. In a recent investigation of the mobility of Xanthan drops on dry superhydrophobic surfaces, it was argued that the ratio of yield and gravitational stresses $\sigma_{yield}/\sigma_{grav}$ differentiates the rolling and sliding regimes. In detail, when the gravitational stress overcomes the yield stress, the drop is fluidized at least in its lower part in contact with the lubricated surface and thus

rolls down on a slippery surface. To some extent, this scaling is analogous to the criteriom proposed in chapter 3 for the untrapping of a solid inclusion in a YSF, dictated by the same ratio but with very different prefactors, determined by the geometry of the system. We rescaled the data in Figure 5.7 in the new phase diagram shown in Figure 5.9, where the two types of motion are classified in terms of the yield stress σ_{yield} of the various solutions as measured from the bulk rheology, normalized to the corresponding gravitational stress σ_{grav}. The criterion originally proposed for rolling of YSF droplets on dry superhydrophobic surfaces is also found to be well satisfied on lubricated surfaces: in the case of SF2 droplets, all the explored conditions are characterized by $\sigma_{yield}/\sigma_{grav} < 1$. While 971P droplets undergo rolling when $\sigma_{yield}/\sigma_{grav} < 1$. Such a good agreement is somewhat surprising considering the higher complexity of the interface, where there is both slip in the oil film and shear of the YSF[32]. Conversely, sliding of 971P droplets is found for $\sigma_{yield}/\sigma_{grav} > 1$. In this case, sliding is also observed in a gray area extending somewhat below 1 and is not unexpected given the simplicity of this argument. Actually, we did not expect to imagine that this criterion, which compares the bulk rheology of the Carbopol solutions (σ_{yield}) to the experimental conditions (Ω and α), worked so remarkably well to account for our measurements. Further information may come from high-resolution, local imaging of the bottom layers of the sliding/rolling droplets.

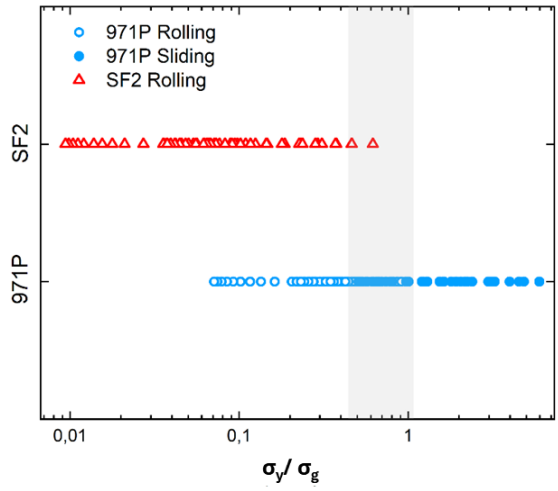

Figure 5.9: Phase diagram in which the type of droplet motion is classified in terms of the ratio $\sigma_{yield}/\sigma_{grav}$ for droplets of 971P and SF2 solutions.

5.4 Conclusions

We studied the dynamic wetting on an engineered substrate focusing on both spreading and mobility of a yield stress fluid based on a suspension of swollen Carbopol microgels. By changing their concentration[23,35], it was possible to vary their bulk yield stress σ_{yield}, that is the minimum stress required to fluidize the suspension. The characterization of the mobility of Carbopol droplets on an inclined plane was only made possible by the use of lubricant infused surfaces[22,32]. Indeed, we report for the first time that

millimeter-size YSF droplets show distinct sliding and rolling regimes on such slippery surfaces. Sliding occurs when the droplets are more solid-like, and their velocity is determined by the shear flow of the oil film that covers the solid substrate. Instead, when the gravitational stress exceeds a certain threshold, the droplet is partially fluidized and can thus deform and roll down, as generally reported for ordinary Newtonian droplets [14–16]. A simple criterion based on the ratio $\sigma_{yield}/\sigma_{grav}$ was found to capture the transition between the two regimes: rolling when $\sigma_{yield}/\sigma_{grav} \lesssim 1$ and sliding when $\sigma_{yield}/\sigma_{grav} \gtrsim 1$. Such a scaling could be used as a reliable gauge in the design of microfluidic devices that involve the control of the motion of YSF droplets. Particle imaging velocimetry of dispersed tracers [28], integrated by dedicated numerical simulations [30,52], can provide further useful insight into the local rearrangements at the oil-YSF interface and the extent of fluidization within sliding/rolling droplets.

Our results confirm that the study of the gravity induced motion of droplets on slippery lubricated surfaces can provide a simple but powerful tool to address the interfacial and bulk properties of a wide range of complex fluids, such as colloidal suspensions or polymeric solutions. Surprisingly, these fluids would barely move on superhydrophobic dry rough surfaces, which are known to present very little friction to the motion of water droplets [53,54], but that, however, lose some of their useful characteristics when exposed to complex fluids [31,55].

Bibliography

[1] P. De Gennes, F. Brochard-Wyart, and D. Quere. *Capillarity and wetting phenomena: drops, bubbles, pearls, waves*. Springer Science & Business Media, 2004.

[2] L. Bocquet and E. Charlaix. Nanofluidics, from bulk to interfaces. *Chemical Society Reviews*, 39(3):1073–1095, 2010.

[3] G. Mistura and M. Pierno. Drop mobility on chemically heterogeneous and lubricant-impregnated surfaces. *Advances in Physics: X*, 2(5):591–607, 2017.

[4] D. Bonn, J. Eggers, J. O. Indekeu, J. Meunier, and E. Rolley. Wetting and spreading. *Reviews of Modern Physics*, 81:739, 2009.

[5] P. Roach, N. J. Shirtcliffe, and M. I. Newton. Progress in superhydrophobic surface development. *Soft Matter*, 4(2):224–240, 2008.

[6] A. Lafuma and D. Quéré. Slippery pre-suffused surfaces. *EPL (Europhysics Letters)*, 96(5):56001, 2011.

[7] T.-S. Wong, S. H. Kang, S. K. Y. Tang, E. J. Smythe, B. D. Hatton, A. Grinthal, and J. Aizenberg. Bioinspired self-repairing slippery surfaces with pressure-stable omniphobicity. *Nature*, 477(7363):443–447, 2011.

[8] S. Anand, A. T. Paxson, R. Dhiman, J. D. Smith, and K. K. Varanasi. Enhanced condensation on lubricant-impregnated nanotextured surfaces. *ACS nano*, 6(11): 10122–10129, 2012.

[9] M. J. Kreder, J. Alvarenga, P. Kim, and J. Aizenberg. Design of anti-icing surfaces: smooth, textured or slippery? *Nature Reviews Materials*, 1(1):15003, 2016.

[10] D. C. Leslie, A. Waterhouse, J.-B. Berthet, T. M. Valentin, A. L. Watters, A. Jain, P. Kim, B. D. Hatton, A. Nedder, K. Donovan, et al. A bioinspired omniphobic surface coating on medical devices prevents thrombosis and biofouling. *Nature biotechnology*, 32(11):1134–1140, 2014.

[11] J. Li, E. Ueda, D. Paulssen, and P. A. Levkin. Slippery lubricant-infused surfaces: properties and emerging applications. *Advanced Functional Materials*, 29(18): 1802317, 2019.

[12] D. P. Regan and C. Howell. Droplet manipulation with bioinspired liquid-infused surfaces: A review of recent progress and potential for integrated detection. *Current Opinion in Colloid & Interface Science*, 39:137–147, 2019.

[13] J. Wang, L. Wang, N. Sun, R. Tierney, H. Li, M. Corsetti, L. Williams, P. K. Wong, and T.-S. Wong. Viscoelastic solid-repellent coatings for extreme water saving and global sanitation. *Nature Sustainability*, 2(12):1097–1105, 2019.

[14] J. D. Smith, R. Dhiman, S. Anand, E. Reza-Garduno, R. E. Cohen, G. H. McKinley, and K. K. Varanasi. Droplet mobility on lubricant-impregnated surfaces. *Soft Matter*, 9(6):1772–1780, 2013.

[15] A. Keiser, L. Keiser, C. Clanet, and D. Quéré. Drop friction on liquid-infused materials. *Soft Matter*, 13(39):6981–6987, 2017.

[16] D. Daniel, J. V. I. Timonen, R. P. Li, S. J. Velling, and J. Aizenberg. Oleoplaning droplets on lubricated surfaces. *Nature Physics*, 13(10):1020–1025, 2017.

[17] C. Rigoni, D. Ferraro, M. Carlassara, D. Filippi, S. Varagnolo, M. Pierno, D. Talbot, A. Abou-Hassan, and G. Mistura. Dynamics of ferrofluid drops on magnetically patterned surfaces. *Langmuir*, 34(30):8917–8922, 2018.

[18] P. Sartori, E. Guglielmin, D. Ferraro, D. Filippi, A. Zaltron, M. Pierno, and G. Mistura. Motion of newtonian drops deposited on liquid-impregnated surfaces induced by vertical vibrations. *Journal of Fluid Mechanics*, 876:R4, 2019.

[19] S. Varagnolo, D. Filippi, G. Mistura, M. Pierno, and M. Sbragaglia. Stretching of viscoelastic drops in steady sliding. *Soft Matter*, 13(17):3116–3124, 2017.

[20] J. D. Ferry. *Viscoelastic properties of polymers*. John Wiley & Sons, 1980.

[21] G. Zanchetta, S. Mirzaagha, V. Guida, F. Zonfrilli, M. Caggioni, N. Grizzuti, R. Pasquino, and V. Trappe. Colloidal fibers as structurant for worm-like micellar solutions. *Colloid and Polymer Science*, 296(8):1379–1385, 2018.

[22] P. Sartori, D. Ferraro, M. Dassie, A. Meggiolaro, D. Filippi, A. Zaltron, M. Pierno, and G. Mistura. Oscillatory motion of viscoelastic drops on slippery lubricated surfaces. *Communications Physics*, 5(1):1–8, 2022.

[23] P. Coussot. Yield stress fluid flows: A review of experimental data. *Journal of Non-Newtonian Fluid Mechanics*, 211:31–49, 2014.

[24] R. Borrega, M. Cloitre, I. Betremieux, B. Ernst, and L. Leibler. Concentration dependence of the low-shear viscosity of polyelectrolyte micro-networks: From hard spheres to soft microgels. *Europhysics Letters*, 47(6):729, 1999.

[25] S. P. Meeker, R. T. Bonnecaze, and M. Cloitre. Slip and flow in soft particle pastes. *Physical Review Letters*, 92(19):198302, 2004.

[26] P. Coussot, L. Tocquer, C. Lanos, and G. Ovarlez. Macroscopic vs. local rheology of yield stress fluids. *Journal of Non-Newtonian Fluid Mechanics*, 158(1-3):85–90, 2009.

[27] R. Benzi, T. Divoux, C. Barentin, S. Manneville, M. Sbragaglia, and F. Toschi. Continuum modeling of shear startup in soft glassy materials. *Physical Review E*, 104(3): 034605, 2021.

[28] M. Jalaal, N. J. Balmforth, and B. Stoeber. Slip of spreading viscoplastic droplets. *Langmuir*, 31(44):12071–12075, 2015.

[29] G. Martouzet, L. Jorgensen, Y. Pelet, A.-L. Biance, and C. Barentin. Dynamic arrest during the spreading of a yield stress fluid drop. *Physical Review Fluids*, 6(4):043302, 2021.

[30] M. Jalaal, B. Stoeber, and N. Balmforth. Spreading of viscoplastic droplets. *Journal of Fluid Mechanics*, 914:A21, 2021.

[31] M. Kim, E. Lee, D.-Y. Kim, and R. Kwak. Decoupled rolling, sliding and sticking of a viscoplastic drop on a superhydrophobic surface. *Journal of Fluid Mechanics*, 908: A41, 2021.

[32] L. Rapoport, B. R. Solomon, and K. K. Varanasi. Mobility of yield stress fluids on lubricant-impregnated surfaces. *ACS Applied Materials & Interfaces*, 11(17):16123–16129, 2019.

[33] A. Wixforth, C. Strobl, C. Gauer, A. Tögl, J. Scriba, and Z. v. Guttenberg. Acoustic manipulation of small droplets. *Analytical and bioanalytical chemistry*, 379(4):982–991, 2004.

[34] T. A. Waigh. Microrheology of complex fluids. *Reports on Progress in Physics*, 68(3): 685, 2005.

[35] V. Vitali, G. Nava, A. Corno, M. Pezzotti, F. Bragheri, P. Paiè, R. Osellame, M. A. Ortenzi, I. Cristiani, P. Minzioni, et al. Yield stress "in a flash": investigation of nonlinearity and yielding in soft materials with an optofluidic microrheometer. *Soft Matter*, 17(11):3105–3112, 2021.

[36] P. Edera, M. Brizioli, G. Zanchetta, G. Petekidis, F. Giavazzi, and R. Cerbino. Deformation profiles and microscopic dynamics of complex fluids during oscillatory shear experiments. *Soft Matter*, 17(28):8553–8566, 2021.

[37] D. Ferraro, M. Serra, D. Filippi, L. Zago, E. Guglielmin, M. Pierno, S. Descroix, J.-L. Viovy, and G. Mistura. Controlling the distance of highly confined droplets in a capillary by interfacial tension for merging on-demand. *Lab on a Chip*, 19(1):136–146, 2019.

[38] S. Sett, X. Yan, G. Barac, L. W. Bolton, and N. Miljkovic. Lubricant-infused surfaces for low-surface-tension fluids: Promise versus reality. *ACS Applied Materials & Interfaces*, 9(41):36400–36408, 2017.

[39] M. Caggioni, V. Trappe, and P. T. Spicer. Variations of the herschel–bulkley exponent reflecting contributions of the viscous continuous phase to the shear rate-dependent stress of soft glassy materials. *Journal of Rheology*, 64(2):413–422, 2020.

[40] C. Semprebon, S. Varagnolo, D. Filippi, L. Perlini, M. Pierno, M. Brinkmann, and

G. Mistura. Deviation of sliding drops at a chemical step. *Soft Matter*, 12(32):8268–8273, 2016.

[41] T. Toth, D. Ferraro, E. Chiarello, M. Pierno, G. Mistura, G. Bissacco, and C. Semprebon. Suspension of water droplets on individual pillars. *Langmuir*, 27(8):4742–4748, 2011.

[42] L. Mahadevan and Y. Pomeau. Rolling droplets. *Physics of Fluids*, 11(12):2449–2453, 1999.

[43] S. R. Hodges, O. E. Jensen, and J. M. Rallison. Sliding, slipping and rolling: the sedimentation of a viscous drop down a gently inclined plane. *Journal of Fluid Mechanics*, 512:95–131, 2004.

[44] B. M. Mognetti, H. Kusumaatmaja, and J. M. Yeomans. Drop dynamics on hydrophobic and superhydrophobic surfaces. *Faraday Discussions*, 146:153–165, 2010.

[45] S. P. Thampi, R. Adhikari, and R. Govindarajan. Do liquid drops roll or slide on inclined surfaces? *Langmuir*, 29(10):3339–3346, 2013.

[46] D. Richard and D. Quéré. Viscous drops rolling on a tilted non-wettable solid. *Europhysics Letters*, 48(3):286–291, 1999.

[47] V. Lombardi, M. La Rocca, A. Montessori, S. Succi, and P. Prestininzi. On the fate of a drop jumping over a gap. *Journal of Fluid Mechanics*, 949:A27, 2022.

[48] H. Y. Kim, H. J. Lee, and B. H. Kang. Sliding of liquid drops down an inclined solid surface. *Journal of Colloid and Interface Science*, 247(2):372–380, 2002.

[49] N. Le Grand, A. Daerr, and L. Limat. Shape and motion of drops sliding down an inclined plane. *Journal of Fluid Mechanics*, 541:293–315, 2005.

[50] S. Varagnolo, D. Ferraro, P. Fantinel, M. Pierno, G. Mistura, G. Amati, L. Biferale, and M. Sbragaglia. Stick-slip sliding of water drops on chemically heterogeneous surfaces. *Physical review letters*, 111(6):066101, 2013.

[51] J. Pemeja, B. Géraud, C. Barentin, and M. Le Merrer. Wall slip regimes in jammed suspensions of soft microgels. *Physical Review Fluids*, 4(3):033302, 2019.

[52] P. Saramito and A. Wachs. Progress in numerical simulation of yield stress fluid flows. *Rheologica Acta*, 56(3):211–230, 2017.

[53] T. Mouterde, P.-S. Raux, C. Clanet, and D. Quéré. Superhydrophobic frictions. *Proceedings of the National Academy of Sciences*, 116(17):8220–8223, 2019.

[54] P. Sarkiris, K. Ellinas, D. Gkiolas, D. Mathioulakis, and E. Gogolides. Motion of drops with different viscosities on micro-nanotextured surfaces of varying topography and wetting properties. *Advanced Functional Materials*, 29(19):1902905, 2019.

[55] H. Xu, A. Clarke, J. P. Rothstein, and R. J. Poole. Viscoelastic drops moving on hydrophilic and superhydrophobic surfaces. *Journal of Colloid and Interface Science*, 513:53–61, 2018.

CHAPTER 6

Appendix: Rheo-microscopy on viscoelastic surfact solutions

This chapter reports the results of a collaboration with prof. Rossana Pasquino and dr. Ilaria Cusano (Dipartimento di Ingegneria Chimica, dei Materiali e della Produzione Industriale, University of Napoli "Federico II"). My main responsibility was to conduct microscopy-based reconstruction of flow profiles and the onset of instabilities in a wormlike system in correlation with the nonlinear rheological behavior investigated in Naples. The results were submitted as a research article to *Journal of Colloid and Interface Science*:

Ilaria Cusano, Afshin Azarpour *et al.*
"Exploring the nonlinear behavior of long loosely entangled wormlike micelles: a rheology and rheo-microscopy study"

Introduction

Surfactants, a class of self-assembling amphiphilic molecules, possess intriguing properties that are the focus of research and industrial applications[1,2]. In solution, these molecules tend to rearrange into ordered colloidal structures, called micelles, which limit the exposure of their hydrophobic tails to water. Such structures may undergo conformational changes in response to temperature[3], pH[4], or the presence of additives[5]. In particular, the addition of a penetrating salt, characterized by having at least one aromatic ring, induces a spherical-to-wormlike micellar transition[6,7]. Such wormlike micelles (WLMs) display most intriguing viscoelastic properties, analogous to those observed in polymers. The key distinction between polymers and WLMs lies in the nature of the bonds that are created between the molecules. Unlike the stronger covalent bonds that connect polymer chains, micellar bonds are physical[8] and subject to continuous breakage and reformation at the microstructural length scale, hence the epithet of living polymers. Increasing the salt concentration in solution can induce further conformational transitions, leading to entangled[9] or branched micelles[10], or even a shift to vesicles and lamellar phases[11]. By performing linear rheology tests, information can be deduced on the micellar self-assemblies, and on their characteristic relaxation times[12]. Mesoscopic WLMs length scales can be evaluated from viscoelastic spectra using established scaling laws[13].
In general, the relaxation dynamics of WLMs are well described by the Cates model[14], which is based on two specific relaxation phenomena: a reptation process, which characterizes the sliding of the worm within a tubular constraint created by the surrounding WLMs, and a breaking and reforming time, which considers micelles rearrangement.

The two characteristic times can be evaluated from linear viscoelasticity tests according to the equations:

$$\tau_b = \frac{1}{\omega_{min}} \tag{6.1}$$

$$\tau_r = \frac{\tau_d^2}{\tau_b} \tag{6.2}$$

where τ_b and τ_r are the breaking and reptation times, respectively; ω_{min} is the angular frequency which corresponds to the minimum of the loss modulus, G''_{min}, and τ_d is the disengagement time, evaluated as the inverse of the crossover frequency at which the viscoelastic moduli cross in a dynamic test. The average entanglement number, Z, can also be expressed as the ratio between G'_{min} and G''_{min}. G'_{min} is the value of the storage modulus at the angular frequency at which G''_{min} is detected. Additionally, the Cates model enables to estimate the characteristic lengths of the wormlike micelles, including the entanglement length, l_e, and the contour length L_c, which are the typical distance between two network nodes and an underestimation of the total length of the WLMs, respectively[14,15]. Unfortunately, it is only possible to estimate these lengths once the persistence length, l_p, which correlates with the stiffness of the micelle, has been determined. Indeed, it is difficult to achieve a broad range in frequency exclusively through rheology. At very high frequencies, where bending modes of Kuhn segments dominate, another crossover frequency, ω_0, can be detected[16]. If measurable, the persistence length can be estimated through[17]

$$\omega_0 = \frac{k_B T}{8\eta_s {l_p}^3} \tag{6.3}$$

where k_B is the Boltzmann constant, T is the experimental temperature, η_s is the solvent viscosity. As such, the experimental tests typically combine standard rheology with specialized devices or optical techniques[17–19].

Following Cates, several authors have focused their efforts on further elaborating the description of WLMs relaxation dynamics[20–23]. In this context, Tan et al.[24] developed new expressions for the linear viscoelastic properties as a function of l_e and L_c by correlating the predictions of the mesoscopic pointer algorithm[23,25] with the microscopic slip-spring model[26]:

$$G_0 = \frac{\alpha^3}{3+\alpha^3} \cdot 9.75 \frac{k_B T}{\alpha^{1.8} l_p^3} + \frac{3}{3+\alpha^3} \cdot \frac{28}{5\pi} \frac{\varphi k_B T}{d^2 \alpha l_p} \tag{6.4}$$

$$\frac{G'_{\text{min}}}{G''_{\text{min}}} = 0.317 \left(\frac{L_c}{l_e} \right)^{0.82} \tag{6.5}$$

where α is a so-called semi-flexibility factor (defined as the ratio between l_e and l_p), φ is the micelles volume fraction, d is the micelle diameter. In this scenario, cryo-EM is an effective technique to couple with WLMs rheology, as it allows direct visualization of the micelles and their morphology[27–29].

In our recent work in very dilute wormlike micellar solutions, the whole relaxation spectrum was covered by linear rheology[13]. More specifically, we have found that diluted micellar solutions of cetylpyridinium chloride (CPyCl), a widely studied ionic surfactant, and diclofenac sodium (Diclo), a non-steroidal anti-inflammatory drug, are characterized by exceptionally long and rigid WLMs, enabling the measurement of all characteristic parameters without the need for additional techniques beyond linear rheology.

Moreover, the properties of the CPyCl-Diclo systems also make them a non-trivial test bench for the investigation of the rich nonlinear behaviour of WLMs when subjected to strong flows, a scenario that is frequently encountered in industrial contexts. The Weissemberg number, defined as $Wi_d = \tau_d \dot{\gamma}$, where $\dot{\gamma}$ is the applied shear rate, is the threshold between linear and nonlinear regime. When Wi_d exceeds 1, the system is subjected to a strong force field and WLMs' flow can exhibit complex features: shear thinning, which represents the result of the alignment and stretching of the micelles along the flow direction[10,30,31]; shear banding, which is a flow instability resulting in the micellar solution splitting into bands of different concentrations and shear rates across the gap[3,32,33]; and strain hardening, which is the sudden increase in the shear stress growth coefficient[34].

More specifically, WLMs can show non-equilibrium phase coexistence arising along the gradient direction between an isotropic solution and an aligned (paranematic) band with lower viscosity than the quiescent phase[35–37]. These bands result from mechanical instability, producing two branches (shear bands), one at low and the other at high shear rates. Band sizes typically follow the lever rule. In a simple shear-banding scenario, the fluid is divided into just two clear regions separated by a thin, steady interface of very small width.

The phenomenon of strain hardening in micellar solutions was first identified in 1988 by Shikata et al.[30], who conducted nonlinear step strain and step rate experiments on a system of cetyltrimethylammonium bromide (CTAB) and sodium salicylate (NaSal). Later studies by Brown et al.[38] investigated this phenomenon in more detail in the same systems, identifying strain hardening only when the strain overcame 3.5. In 1994, Proud'homme and Warr[39] observed strain hardening during extensional tests, and suggested a possible correlation between this phenomenon and WLMs scission, proposing that the observed decrease in stress growth coefficient post-hardening was due to the breakage of WLMs. Rothstein[40] later corroborated this hypothesis by performing extensional tests on the CTAB/NaSal systems using a filament stretching rheometer, determining a scission energy close to $4k_BT$, consistent with predictions made by Turner and Cates in 1992[41]. Since then, various studies have further explored strain hardening, providing evidence of its correlation with the WLMs finite extensibility. Indeed, it is well-established that the WLMs network can store energy up to a certain maximum deformation, after which scission can eventually take place[34,42–46].

In most complex fluids, nonlinear bulk rheological response often corresponds to local alignment and structural rearrangements occurring at the microscale. These can be triggered and probed through active microrheology approaches which provide access to local mechanical properties by applying an external force to an embedded microparticle[47,48]. However, such methods miss the coupling of structural rearrangements with macroscopic deformations, which requires the application of a technique capable of nano-, micro- or mesoscale resolution to the sample, while it is subjected to bulk stress/strain application. For example, rheo-SANS (Small Angle Neutron Scattering) gives access to non-affine local flow fields of WLMs during large amplitude oscillations[49], and rheo-microscopy can provide critical information on deformation profiles[50], degree of alignment[51], or local rearrangements[52].

In the present work, an investigation is conducted into a distinctive sample, based on CPyCl and Diclo, which displays the entire relaxation time spectra within the experimental frequency window in linear rheology, and a distinguished nonlinear response in start-up flow. Its flow curve is built in a wide range of shear rates, by combining classical rotational rheometry with a printer used as a capillary rheometer. The evaluation of the theoretical scission energy and its actual correlation with the energy cumulated

by the shear work during a steady test are discussed. To gain insight into the origin of the peculiar rheological behavior displayed by CPyCl-Diclo, we run parallel rheo-microscopy experiments of shear start-up, estimating the time-dependent deformation profiles across the gap during the accumulation of strain, combined with cryo-EM analysis of the micelles. We discuss a non-trivial correlation between WLMs banding and scission.

Materials and Methods

Materials

The sample, 16.7 mM CPyCl 11.0 mM Diclo, was prepared by dissolving both chemicals (available as powders from Sigma-Aldrich) in double-distilled water, according to the methodology detailed in [13].

Rheology

Linear viscoelasticity tests were conducted on a stress-controlled rheometer DHR-2, from TA Instruments, equipped with 40 mm-diameter sandblasted parallel plates. A Peltier cell was employed for temperature control and a solvent trap used to prevent evaporation. Once the linear viscoelasticity regime was identified, dynamic frequency sweep tests (DFST) were conducted in the angular frequencies range of $[100; 0.05] rad/s$, with a strain of 10% and a constant temperature of 25°C.
Nonlinear rheology tests were performed with a strain-controlled ARES rheometer (TA instruments, USA), equipped with a 50 mm-diameter cone-plate geometry. The transient behaviour of the micellar solution was investigated through step-rate tests at a series of fixed shear rates, under room temperature (kept at 25°C). For each investigated shear rate, a fresh sample was loaded.
Since nonlinear shear measurements are affected by instabilities as the sample is subjected to strong flow [53], a 3D bioprinter (BIOX Cellink, Göteborg, Sweden), operated as a capillary rheometer, was used to achieve very high shear rates. The test procedure was conducted according to the protocol outlined in [54]. The experiments were carried out at 25°C, using a nozzle of 33 mm in length and 0.413 mm in diameter, within the pressure range $[3; 30] kPa$. Given the high lenght-to-diameter ratio, the flow can be assumed to be fully developed. Shear stress and viscosity as a function of shear rate were obtained by applying the standard relations for capillary rheometry [55] when a known pressure drop is applied.
Extensional rheology tests were conducted using a home-made experimental setup, which was developed based on the *Ambient DoS rheometer* described in [56]. A syringe pump was employed to create the droplet, at a fixed flow rate of 22 μl/min. Filament formation was achieved by adopting the *stationary drop* [57] approach. This involved the gradual elevation of the bottom plate, until contact with the drop was established, at a distance of approximately 1.5 mm from the nozzle. A high-speed camera (iX Cameras, i-SPEED 203) with a frame rate of 50 frames per second (fps) was then used to capture the resulting images. Finally, a MATLAB routine was built to process the data.

Rheo-microscopy

The sample was loaded between the two parallel plates of a linear strain-controlled shear-cell (RheOptiCAD, CAD Instruments, France)[58], modified to enable bright-field imaging and coupled to a Nikon Eclipse Ti-S inverted microscope. Although the linear geometry limits the total attainable strain, it guarantees a uniform strain at the confining surfaces, while providing optical access to the sample. The glass slides were sandblasted to minimize slip of the sample, except for a small central window kept clear for optical access. We can impose continuous displacement of one plate, while keeping the opposite plate fixed, or simultaneous motion of both plates to achieve higher total strain and shear rate. Polystyrene microparticles (diameter 1.04 μm, Microparticles GmbH) were dispersed in the sample at a volume fraction of about $5 \cdot 10^{-4}$ to optically reconstruct the flow field in the sample, without affecting its rheological properties. The gap was kept constant at 300 μm, well above any relevant length scale of the system. The focus was adjusted at different heights across the gap. The vertical resolution is about 20 micrometers, as obtained by keeping the condenser (LWD, NA=0.52) diaphragm open, thus reducing the coherence of illumination and minimizing the depth-of-focus and the thickness of the layer in which tracers are visible[50]. Measurements were performed at a constant temperature of 25°C. Images were acquired using a $10\times$ objective and a CMOS camera (Ximea xiC MC031MG-SY) with a rectangular region of interest (ROI) of $617\,\mu\mathrm{m} \times 183\,\mu\mathrm{m}$, or a high-speed sCMOS camera (Teledyne Prime BSI Express) with a ROI of $1163\,\mu\mathrm{m} \times 144\,\mu\mathrm{m}$. The frame rate was adjusted between $10\,\mathrm{Hz}$ and $557\,\mathrm{Hz}$, depending on the imposed shear rate. This configuration enabled high-resolution reconstruction of the trajectories of hundreds of tracer particles within a single experiment over sufficiently long time intervals. Image processing was performed using a custom Python code to identify potential heterogeneities within the imaging planes and extract the average tracer velocity for each height and time interval.

Cryo-EM

Cryo-EM samples were prepared at 25°C using a Vitrobot Mark 4 in a water vapor-saturated environment. A 5 μL droplet was applied to a Quantifoil R1.2/1.3 copper grid. Excess solution was removed via blotting with filter paper on rotating foam pads under controlled conditions. After a 10–15 second relaxation period, the grid was plunged into liquid ethane, vitrified, and stored in liquid nitrogen. The vitrified samples were analyzed with a 200 kV Glacios TEM using a Falcon 4 direct detector at low-dose conditions, with nominal magnifications ranging between 73k and 190k[59].

Results and discussion

Rheological response

Figure 6.1 reports the linear viscoelastic moduli, along with the complex viscosity, as a function of the angular frequency. The sample shows a strong viscoelastic behaviour, typical of a wormlike micellar network. The micelles relax on a very long time scale, with a total relaxation time of the order of seconds (the inverse of the crossover at low frequencies, τ_d), and present an elastic plateau, G_0, spanning more than two decades in frequency. As already shown in a recent work[13], the very low surfactant concentration allows to cover the entire relaxation spectrum. The inverse of the crossover at high frequencies, τ_0, has been extrapolated from the linear viscoelastic response and allows a

direct estimation of the wormlike micelles persistence length (Equation 6.3). The reptation time τ_r of the micelles can be easily evaluated through Equation 6.2. The relatively low zero-frequency viscosity (roughly 10 Pa·s) and the high relaxation time suggest the presence of very long, loosely entangled ($Z = 6$, evaluated as stated in the Introduction) wormlike micelles, with a contour length roughly close to 20 micrometers, obtained by using Equation 6.4 and Equation 6.5. The complete set of viscoelastic parameters and characteristic lengths are summarized in Table 6.1. A direct visualization of the micelles through cryo-EM is reported in Figure 6.2, confirming the morphology inferred by the linear viscoelasticity. Micelles indeed appear very long (no chain ends can be distinguished in the images) and entangled.

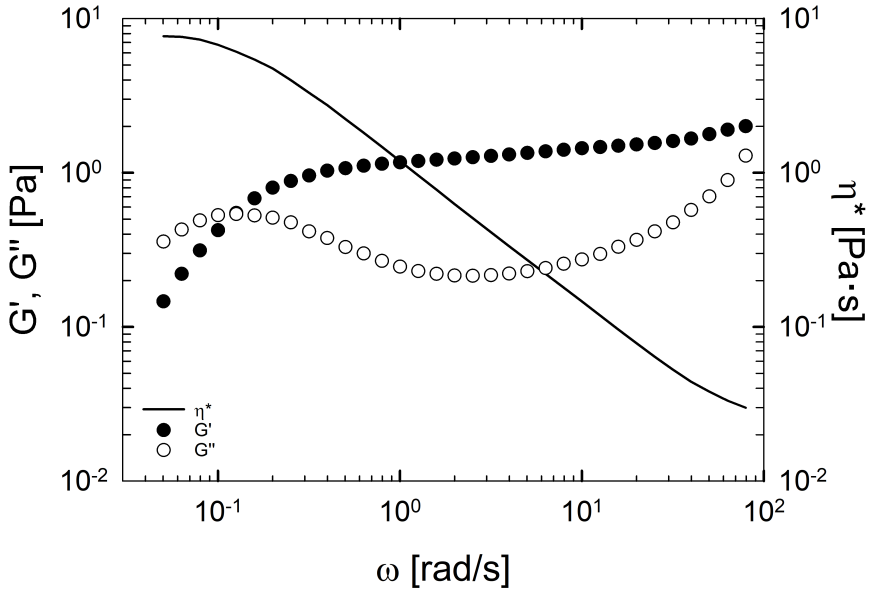

Figure 6.1: Linear viscoelastic moduli of the investigated surfactant solution (left axis) and corresponding complex viscosity (right axis).

Table 6.1: Characteristic viscoelastic parameters and extrapolated lengths.

$G_0\ [Pa]$	$\tau_d\ [s]$	$\tau_b\ [s]$	$\tau_r\ [s]$	$\tau_0\ [s]$	$Z\ [-]$	$l_p\ [nm]$	$l_e\ [nm]$	$L_c\ [nm]$
1.26	7.9	0.4	156	0.008	6	160	530	19200

Figure 6.3 shows the results of the capillary-thinning experiment on the micellar solution. In Fig. 6.3 a), six snapshots of the filament are reported, acquired during the test. From these images, the temporal evolution of the filament thinning can be tracked [60]. The transition from the viscocapillary region, VC, distinguished by an hourglass shape, to the elastocapillary region, EC, characterized by a column shape of the filament, is then followed by the occurrence of the pinch-off in the region of finite extensibility, FE. Fig. 6.3 b) displays the filament diameter as a function of time. The three capillarity regions can also be identified. In the initial time interval, the VC Newtonian behavior barely

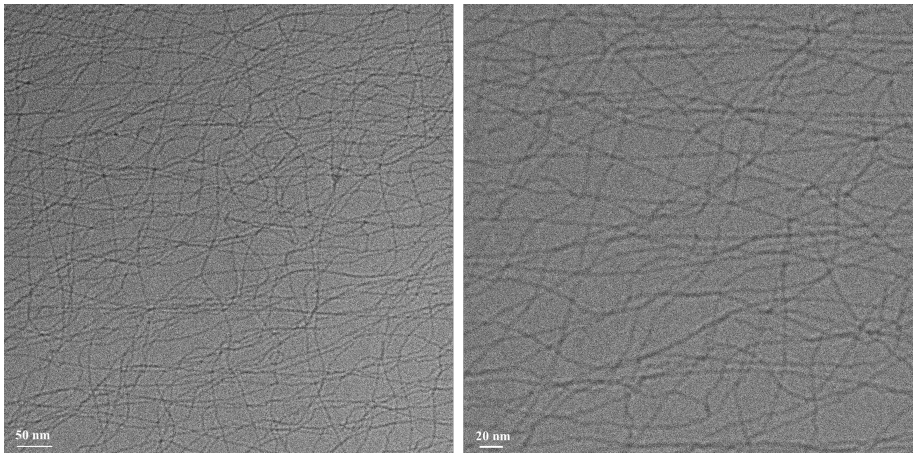

Figure 6.2: Cryo-EM images of the CPyCl-Diclo micelles at 16.7mMCpyCl 11.0mM Diclo composition. The scale bar is displayed at the bottom left of each image.

appears, characterized by a linear decrease of the diameter with time. Then, in the central portion of the graph, which extends until approximately 60 seconds, the behaviour departs from Newtonian, with D_{min} exhibiting an exponential reduction over time (EC behaviour). In the final section, the FE phase, the diameter exhibits again a linear decrease over time, indicating the return to Newtonian behaviour, at enhanced extensional rate, until the filament breaks. A regression procedure was conducted in the EC region to evaluate the constant extensional rate, $\dot{\varepsilon}$, and the extensional relaxation time, λ_E, in accordance with the equations:

$$\dot{\varepsilon}(t) = -\left[\frac{2}{D(t)}\right]\left(\frac{\mathrm{d}D(t)}{\mathrm{d}t}\right) \tag{6.6}$$

$$D \sim \exp\left(-\frac{t}{3\lambda}\right) \tag{6.7}$$

The procedure returned two values, the stretching rate and the extensional relaxation time equal to $0.03s^{-1}$ and $25.5s$, respectively. The latter is roughly 3 times the shear relaxation time, τ_d (Table 6.1), a factor already observed for other micellar solutions [56,61].

Start up experiments were performed in a wide range of shear rates/Weissenberg (Wi) numbers, as reported in Figure 6.4a. In the legend, two Wi numbers are reported at the same value of the shear rate: the first one is obtained by multiplying the shear rate by τ_d and the other by τ_b. We will refer to Wi_d and Wi_b, respectively. At low shear rates (when both Wi_s are lower than 1), the stress growth coefficient monotonically increases up to a steady state. When Wi_d overcomes unity, and Wi_b is still lower than 1, viscosity shows a peak, before reaching the steady state value. In this regime, micelles behave like polymer chains, aligning, stretching and tumbling in the flow direction, as already discussed elsewhere [62]. When Wi_d>1 and Wi_b is roughly close to one, a pronounced strain hardening appears, followed by a well defined maximum and a subsequent sudden viscosity drop, which brings to a "noisy" steady state value. In this shear rate range, the micellar system cannot renew itself with the well-known breaking/reptation-fluctuation mechanism described in the literature: the system remains frozen, displaying a rubber-

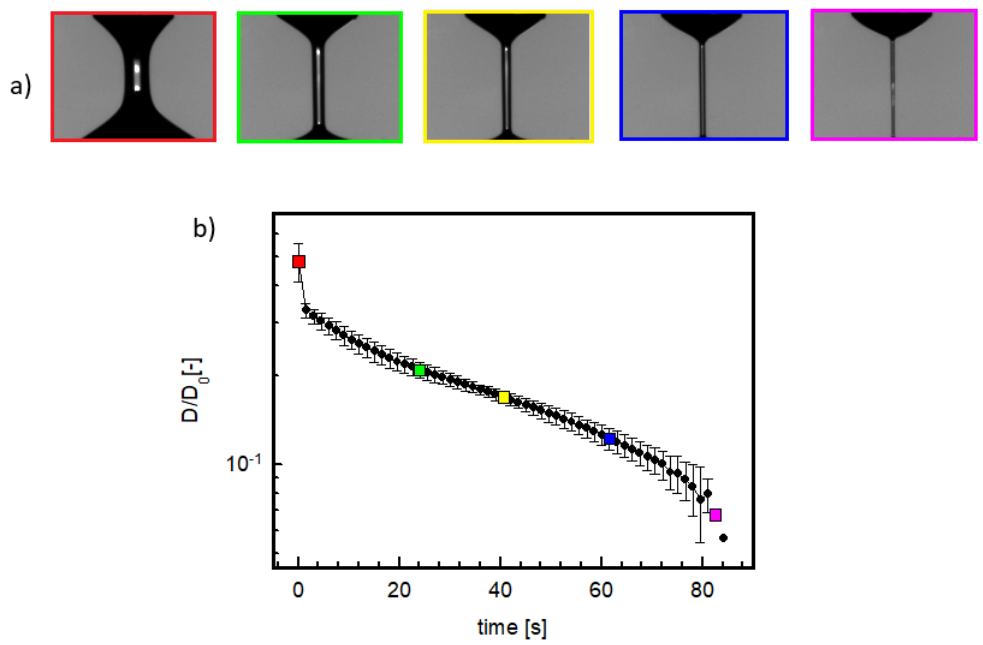

Figure 6.3: Extensional test at $0.03s^{-1}$ on the micellar solution with the DoS setup. (a) Snapshots during the experiment; (b) Thinning diameter for the filament measured as a function of time. The colored squares refer to the time at which the snapshots are taken.

like response. The frozen micellar structure is highly complex, with a characteristic time much longer than τ_d.

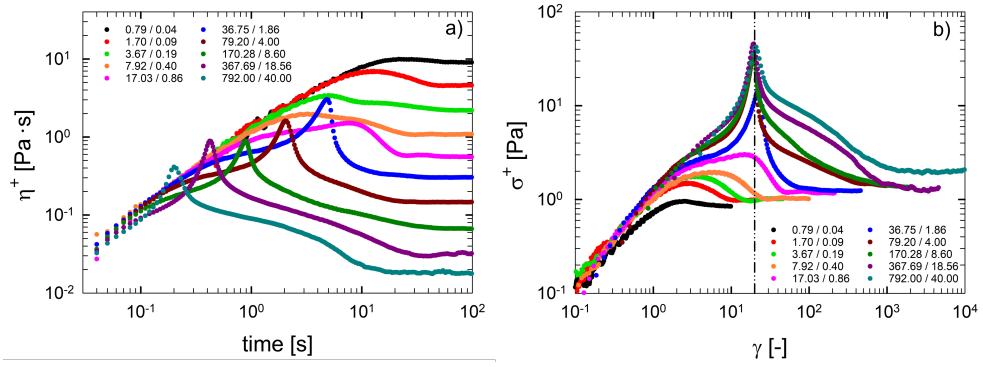

Figure 6.4: (a) The stress growth coefficient as a function of time and (b) the shear stress growth function *vs* strain for the investigated solution at different applied shear rates. The legend reports two distinct Wi numbers: the first is obtained with the disengagement time, τ_d, while the second takes into account the breaking and reforming time, τ_b.

The same data are shown in Figure 6.4b, where the stress growth function is now reported as a function of strain, evaluated as the product of the experimental time and

the imposed shear rate. It is apparent that the data for the fastest flows superimpose to form a single master curve. This feature strongly suggests that at these rates the material behaves as a permanent rubber. Similar responses have been discussed in Inoue et al[34] and Pasquino et al[46]. The upturn at $\gamma = 8$ is clearly due to the finite extensibility of the network strands, whereas the peak at $\gamma_{max} = 20$ is due to a major collapse of the network structure. To rationalize the characteristic times for the onset of this behavior, we have reviewed a few systems in literature, with similar start-up responses[34,46]. It appears clear that all the surfactant systems show hardening when a critical shear rate is reached, usually placed in between $1/\tau_d$ and $1/\tau_b$.

WLMs scission

Start up measurements suggest that the micellar network experiences an abrupt relaxation at roughly 20 strain units. The latter could be considered as a critical value, above which the micellar network breaks *en masse*, under the applied shear work. Although the picture may seem quite quirky, we can compare the scission energy exerted by the experimental shear work with the predicted scission energy for a single chain, from existing theoretical models[12,63]. The experimental scission energy corresponding to the observed drop at γ_{max} can be evaluated through elasticity theory[64] as:

$$E_{sciss,exp} = \frac{1}{2}k\gamma_{max}^2 L_c^2 = \frac{1}{2}\frac{A}{L_c}G_0\gamma_{max}^2 L_c^2 = \frac{1}{2}AG_0\gamma_{max}^2 L_c \tag{6.8}$$

With A the cross section of the WLMs, the diameter being equal to twice the hydrophobic chain length of the surfactant molecule ($A = 1.76 \cdot 10^{-17}\ m^2$). The estimated $E_{sciss,exp}$ is 0.85 10^{-19} Joule.

We can compare this value with the theoretical scission energy, required to create two new chain ends from a single test chain, by pulling them in opposite direction[63]:

$$E_{\text{sciss}} \sim 2k_BT \ln\left(\frac{N_{\text{agg}}}{\varphi^{0.5}}\right) \tag{6.9}$$

Here, N_{agg} is the number of surfactant molecules per micelle, obtained as the number of molecules in a single section per cylinder length unit[65] multiplied by the micelle contour length, reported in Table 6.1. φ is the volume fraction of the surfactant. The theoretical scission energy is equal to roughly 34 $k_BT \sim 1.4 \cdot 10^{-19}$ Joule. The two estimates agree surprisingly well, but are significantly higher than the values reported in literature[40,66]. This is probably due to the high number of aggregation per single micelle and the low surfactant volume fraction, peculiar of this system.

WLMs flow curve

The viscosity steady state values at each shear rate can be plotted as a function of Wi_d (and Wi_b). To extend the range of Wi_d under investigation, we combined shear and capillary rheology measurements, as outlined in the materials and methods section. The lack of data in the Wi_d range between 10^3 and 10^4 arises from strong flow instabilities (in rotational rheology) and insufficient pressure (in capillary rheology).
Figure 6.5 combines the flow curves as a function of Wi_d, the steady state values obtained with the start-up measurements, and the values at very high rates obtained with the capillary rheometry experiments. Shear stress shows a slight increase for Wi_d<1, after which a Wi-independent trend emerges, also found with the continuous flow curve (blue line), conventionally associated with a shear banding phenomenon[67]. The stress

plateau lasts for more than two decades, after which a monotonic increase of the stress at Wi_d values higher than 400 is detected, as expected[36,66]. At very high deformation rates, indeed, the growth in the stress is again linear with respect to the shear rate, due to the presence and deformation of shorter micellar strands.
The viscosity of the micellar solution presents a shear thinning behaviour in the whole investigated strain rate interval. The long worms align in the flow direction, and eventually stretch at very high shear rates[68]. For very high Wi_d values, the viscosity shows a secondary plateau value, very close to the viscosity value of the suspending medium, i.e. water.

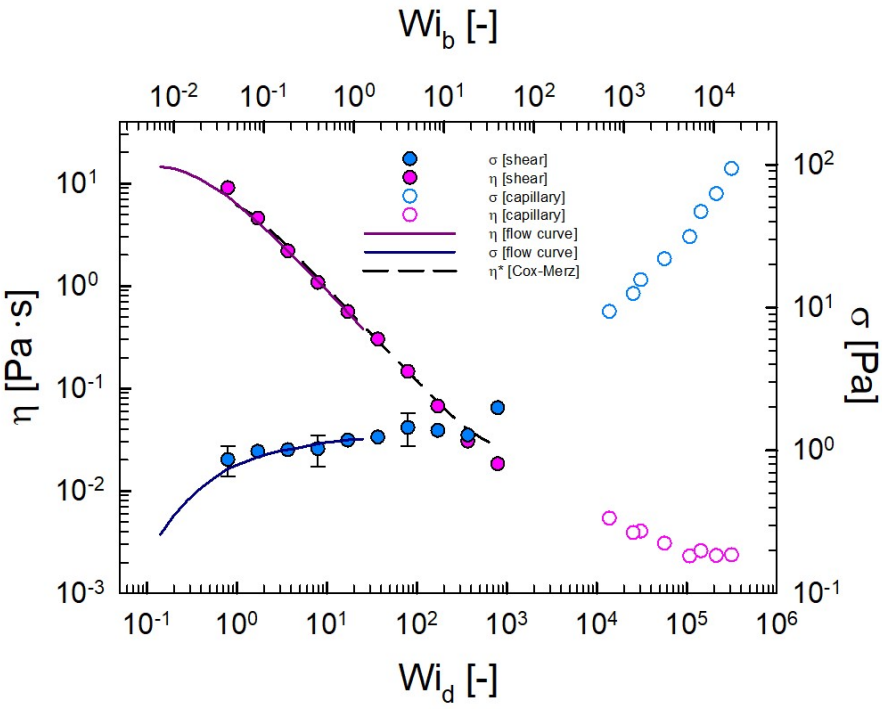

Figure 6.5: Viscosity and shear stress flow curves of the investigated surfactant solution, acquired with both rotational and capillary rheometers. The dashed line is the complex viscosity.

Rheo-microscopy

Previous neutron scattering experiments on viscoelastic WLMs reported the appearance of shear banding above a critical strain value[69], suggesting that a similar phenomenon may occur in our sample. This would also be consistent with the observed stress plateau in the flow curve. To assess this hypothesis in our system, we performed rheo-microscopy experiments, measuring the velocity of tracer particles at different heights in the gap and thus reconstructing flow profiles. Figure 6.6 reports several of such profiles, for different imposed strain rates and for different times - or strains. Each inset plot shows the normalized shear rate value (x axis) at different positions along the gap (y axis). While at very low imposed shear rates all profiles are linear (Wi_d<1), corresponding to affine deformation, for larger shear rates (Wi_d>1) the profiles display the onset of shear banding for high enough cumulated strains. At even higher rates, banding seems to weaken. Unfortunately, the linear shear cell cannot cover the entire range of shear rates and strains accessible with a rotational rheometer. Nevertheless, it is apparent, also in this case, that the profiles show instability when Wi_d is roughly 1, and the deformation becomes significant, while they tend to approach again an affine behaviour when reaching Wi_b. Of course, the comparison between the microscopic and the mascrocopic responses cannot be fully quantitative, since the two geometries are different and the rheological response is, in any case, a picture of the "average" sample behavior.

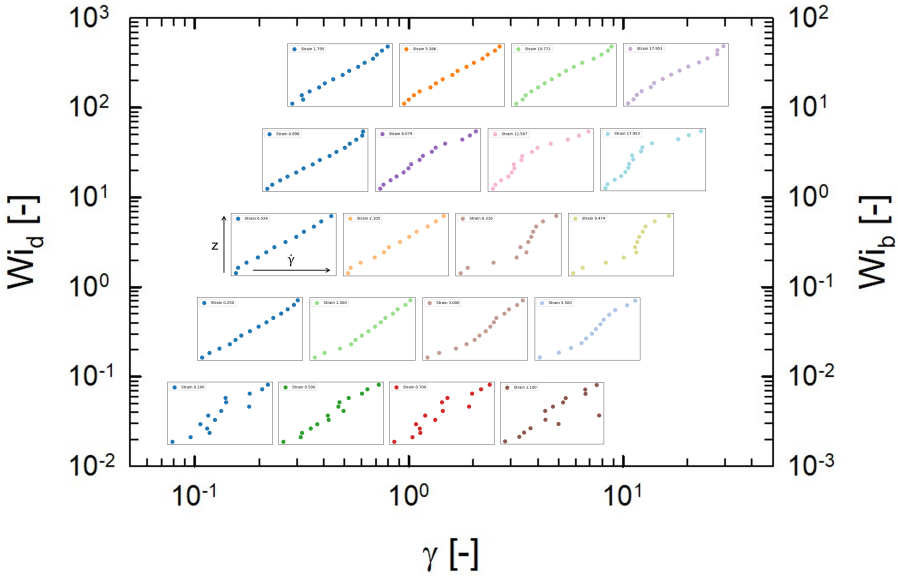

Figure 6.6: Overview of the velocity profiles across the gap for different values of imposed shear rate and for different strain positions. Each inset plot shows the normalized shear rate value (x axis) at different positions along the gap (y axis). The values of the cumulated strain, Wi_d and Wi_b are also reported.

Discussion and conclusions

An in-depth study was conducted on a selected solution of WLMs, combining several techniques, such as shear/extensional/capillary rheology, cryo-EM, and rheo-microscopy. Linear rheology allows to cover the entire relaxation spectrum of the sample, enabling the estimation of the main characteristic parameters and lengths. Micelles were found to be significantly long and poorly entangled, exhibiting a reptation time of the order of hundreds of seconds. This has also been confirmed through linear extensional rheology. Cryo-EM images proved the presence of extremely long micelles and of a loosely entangled network.
The nonlinear rheological response of these WLMs in start-up flow revealed two main phenomena: shear banding and strain hardening. These phenomena happen on completely different time scales. Shear banding appears much before any breaking event takes place, and the characteristic time for the onset of the banding transition is the total relaxation time. The transition from a homogeneous flow field to an inhomogeneous one characterized by the presence of two bands is confirmed through rheo-microscopy.
When the shear rate exceeds the inverse of the breaking and renewing process of the WLMs, these chains are somehow frozen and there is the experimental evidence of their finite extensibility. A rubber-like response is detected, with a catastrophic breakage phenomenon appearing at 20 strain units, above which the system totally collapses. When the system is disrupted and composed by smaller micelles and/or disconnected surfactant molecules in water the solution does not anymore band. By borrowing existing formulas from the rubber elasticity, it has been possible to experimentally evaluate the scission energy, which was found in very good agreement with the theoretical one.
This study sheds a light on the dynamics in fast flows of long and entangled wormlike surfactant solutions, being able to differentiate and decouple banding and breaking. The physical correlation, if any, between the two phenomena, as well as the reasons for the onset of the shear banding to occur, are still pending.

Bibliography

[1] J. Yang. Viscoelastic wormlike micelles and their applications. *Current Opinion in Colloid & Interface Science*, 7(5):276–281, 2002. doi: 10.1016/S1359-0294(02)00071-7.

[2] Z. Chu, C. A. Dreiss, and Y. Feng. Smart wormlike micelles. *Chem. Soc. Rev.*, 42: 7174–7203, 2013. doi: 10.1039/C3CS35490C.

[3] H. Rehage and H. Hoffmann. Rheological properties of viscoelastic surfactant systems. *The Journal of Physical Chemistry*, 92(16):4712–4719, 1988. doi: 10.1021/j100327a031.

[4] R. G. Larson. *The Structure and Rheology of Complex Fluids*. Oxford University Press, Inc., 1999.

[5] H. Hoffmann and G. Ebert. Surfactants, micelles and fascinating phenomena. *Angewandte Chemie International Edition in English*, 27(7):902–912, 1988. doi: 10.1002/anie.198809021.

[6] Z. Lin, J. J. Cai, L. E. Scriven, and H. T. Davis. Spherical-to-wormlike micelle transition in ctab solutions. *The Journal of Physical Chemistry*, 98(23):5984–5993, 1994. doi: 10.1021/j100074a027.

[7] T. H. Ito, P. C. M. L. Miranda, N. H. Morgon, G. Heerdt, C. A. Dreiss, and E. Sabadini. Molecular variations in aromatic cosolutes: Critical role in the rheology of cationic wormlike micelles. *Langmuir*, 30(39):11535–11542, 2014. doi: 10.1021/la502649j.

[8] P. Venkatesan, Y. Cheng, and D. Kahne. Hydrogen bonding in micelle formation. *Journal of the American Chemical Society*, 116(15):6955–6956, 1994. doi: 10.1021/ja00094a068.

[9] H. Rehage and H. Hoffmann. Viscoelastic surfactant solutions: model systems for rheological research. *Molecular Physics*, 74(5):933–973, 1991. doi: 10.1080/00268979100102721.

[10] C. A. Dreiss. Wormlike micelles: where do we stand? recent developments, linear rheology and scattering techniques. *Soft Matter*, 3:956–970, 2007. doi: 10.1039/B705775J.

[11] N. Vlachy, M. Drechsler, J.-M. Verbavatz, D. Touraud, and W. Kunz. Role of the surfactant headgroup on the counterion specificity in the micelle-to-vesicle transition through salt addition. *Journal of Colloid and Interface Science*, 319(2):542–548, 2008. ISSN 0021-9797. doi: 10.1016/j.jcis.2007.11.048.

[12] M. E. Cates and S. J. Candau. Statics and dynamics of worm-like surfactant micelles. *Journal of Physics: Condensed Matter*, 2(33):6869, 1990. doi: 10.1088/0953-8984/2/33/001.

[13] I. Cusano, I. Ionita, P. R. Gonzalez, D. Danino, N. Grizzuti, and R. Pasquino. Drug-induced transitions from micelles to vesicles in ionic surfactant solutions. *Colloids and Surfaces A: Physicochemical and Engineering Aspects*, 690:133793, 2024. ISSN 0927-7757. doi: 10.1016/j.colsurfa.2024.133793.

[14] M. E. Cates. Reptation of living polymers: dynamics of entangled polymers in the presence of reversible chain-scission reactions. *Macromolecules*, 20(9):2289–2296, 1987. doi: 10.1021/ma00175a038.

[15] R. Granek and M. E. Cates. Stress relaxation in living polymers: Results from a poisson renewal model. *The Journal of Chemical Physics*, 96(6):4758–4767, Mar 1992. ISSN 0021-9606. doi: 10.1063/1.462787.

[16] M. Rubinstein and R. H. Colby. *Polymer Physics*. Oxford University Press, 2003.

[17] C. Oelschlaeger, M. Schopferer, F. Scheffold, and N. Willenbacher. Linear-to-branched micelles transition: A rheometry and diffusing wave spectroscopy (dws) study. *Langmuir*, 25(2):716–723, 2009. doi: 10.1021/la802323x.

[18] H. von Berlepsch, L. Harnau, and P. Reineker. Persistence length of wormlike micelles from dynamic light scattering. *The Journal of Physical Chemistry B*, 102(39):7518–7522, 1998. doi: 10.1021/jp980677x.

[19] Marignan, J., Appell, J., Bassereau, P., Porte, G., and May, R.P. Local structures of the surfactant aggregates in dilute solutions deduced from small angle neutron scattering patterns. *J. Phys. France*, 50(24):3553–3566, 1989. doi: 10.1051/jphys:0198900500240355300.

[20] F. Lequeux. Reptation of connected wormlike micelles. *Europhysics Letters*, 19(8):675, 1992. doi: 10.1209/0295-5075/19/8/003.

[21] W. Zou and R. G. Larson. A mesoscopic simulation method for predicting the rheology of semi-dilute wormlike micellar solutions. *Journal of Rheology*, 58(3):681–721, May 2014. ISSN 0148-6055. doi: 10.1122/1.4868875.

[22] J. D. Peterson, W. Zou, R. G. Larson, and M. E. Cates. Wormlike micelles revisited: A comparison of models for linear rheology. *Journal of Non-Newtonian Fluid Mechanics*, 322:105149, 2023. ISSN 0377-0257. doi: https://doi.org/10.1016/j.jnnfm.2023.105149.

[23] W. Zou, G. Tan, M. Weaver, P. Koenig, and R. G. Larson. Mesoscopic modeling of the effect of branching on the viscoelasticity of entangled wormlike micellar solutions.

Phys. Rev. Res., 5:043024, 2023. doi: 10.1103/PhysRevResearch.5.043024.

[24] G. Tan and R. G. Larson. Quantitative modeling of threadlike micellar solution rheology. *Rheologica Acta*, 61(7):443–457, 2022. doi: 10.1007/s00397-022-01341-4.

[25] W. Zou, G. Tan, H. Jiang, K. Vogtt, M. Weaver, P. Koenig, G. Beaucage, and R. G. Larson. From well-entangled to partially-entangled wormlike micelles. *Soft Matter*, 15:642–655, 2019. doi: 10.1039/C8SM02223B.

[26] G. Tan, W. Zou, M. Weaver, and R. G. Larson. Determining threadlike micelle lengths from rheometry. *Journal of Rheology*, 65(1):59–71, Dec 2020. ISSN 0148-6055. doi: 10.1122/8.0000152.

[27] E. Kesselman and D. Danino. Direct-imaging cryo-transmission electron microscopy of wormlike micelles. In *Wormlike Micelles: Advances in Systems, Characterisation and Applications*. The Royal Society of Chemistry, 2017. ISBN 978-1-78262-516-2. doi: 10.1039/9781782629788-00171.

[28] D. Danino and T. Zemb. On the shape and connections of micelles: electron microscopy imaging inspiring thermodynamic modelling. *Current Opinion in Colloid & Interface Science*, 61:101607, 2022. ISSN 1359-0294. doi: https://doi.org/10.1016/j.cocis.2022.101607.

[29] L. Abezgauz, K. Kuperkar, P. A. Hassan, O. Ramon, P. Bahadur, and D. Danino. Effect of hofmeister anions on micellization and micellar growth of the surfactant cetylpyridinium chloride. *Journal of Colloid and Interface Science*, 342:83–92, 2010. ISSN 0021-9797. doi: https://doi.org/10.1016/j.jcis.2009.08.045.

[30] T. Shikata, H. Hirata, E. Takatori, and K. Osaki. Nonlinear viscoelastic behavior of aqueous detergent solutions. *Journal of Non-Newtonian Fluid Mechanics*, 28(2):171–182, 1988. doi: 10.1016/0377-0257(88)85038-9.

[31] J. Berret and D. C. Roux. Rheology of nematic wormlike micelles. *Journal of Rheology*, 39(4):725–741, 1995. doi: 10.1122/1.550654.

[32] J.-F. Berret. Transient rheology of wormlike micelles. *Langmuir*, 13(8):2227–2234, 1997. doi: 10.1021/la961078p.

[33] P. D. Olmsted. Perspectives on shear banding in complex fluids. *Rheologica Acta*, 47 (3):283–300, 2008. doi: 10.1007/s00397-008-0260-9.

[34] T. Inoue, Y. Inoue, and H. Watanabe. Nonlinear rheology of ctab/nasal aqueous solutions: Finite extensibility of a network of wormlike micelles. *Langmuir*, 21(4): 1201–1208, 2005. doi: 10.1021/la048292v.

[35] S. Varchanis, S. J. Haward, C. C. Hopkins, J. Tsamopoulos, and A. Q. Shen. Evaluation of constitutive models for shear-banding wormlike micellar solutions in simple and complex flows. *Journal of Non-Newtonian Fluid Mechanics*, 307:104855, 2022. ISSN 0377-0257. doi: https://doi.org/10.1016/j.jnnfm.2022.104855.

[36] R. L. Moorcroft and S. M. Fielding. Shear banding in time-dependent flows of polymers and wormlike micelles. *Journal of Rheology*, 58(1):103–147, 2014. ISSN 0148-

6055. doi: 10.1122/1.4842155.

[37] J.-B. Salmon, A. Colin, S. Manneville, and F. m. c. Molino. Velocity profiles in shear-banding wormlike micelles. *Phys. Rev. Lett.*, 90:228303, Jun 2003. doi: 10.1103/PhysRevLett.90.228303. URL https://link.aps.org/doi/10.1103/PhysRevLett.90.228303.

[38] E. F. Brown, W. R. Burghardt, and D. C. Venerus. Tests of the lodge meissner relation in anomalous nonlinear step strain of an entangled wormlike micelle solution. *Langmuir*, 13:3902–3904, 1997. doi: 10.1021/la9700376. URL https://doi.org/10.1021/la9700376.

[39] R. K. Prud'homme and G. G. Warr. Elongational flow of solutions of rodlike micelles. *Langmuir*, 10(10):3419–3426, 1994. doi: 10.1021/la00022a010.

[40] J. P. Rothstein. Transient extensional rheology of wormlike micelle solutions. *Journal of Rheology*, 47(5):1227–1247, 2003. doi: 10.1122/1.1603242.

[41] M. S. Turner and M. E. Cates. Flow-induced phase transitions in rod-like micelles. *Journal of Physics: Condensed Matter*, 4(14):3719, 1992. doi: 10.1088/0953-8984/4/14/005.

[42] A. Bhardwaj, D. Richter, M. Chellamuthu, and J. P. Rothstein. The effect of preshear on the extensional rheology of wormlike micelle solutions. *Rheologica Acta*, 46 (6):861–875, 2007. doi: 10.1007/s00397-007-0168-9.

[43] S. Majumdar and A. K. Sood. Nonlinear viscoelasticity of entangled wormlike micellar fluid under large-amplitude oscillatory shear: Role of elastic taylor-couette instability. *Phys. Rev. E*, 89, 2014. doi: 10.1103/PhysRevE.89.062314.

[44] D. Sachsenheimer, B. Hochstein, and N. Willenbacher. Experimental study on the capillary thinning of entangled polymer solutions. *Rheologica Acta*, 53(9):725–739, 2014. doi: 10.1007/s00397-014-0789-8.

[45] S. Fujii, H. Morikawa, M. Ito, and T. Takahashi. Transient behavior of stress in a wormlike micellar solution under oscillatory shear. *Colloid and Polymer Science*, 293 (11):3237–3248, 2015. doi: 10.1007/s00396-015-3674-9.

[46] R. Pasquino, P. R. Avallone, S. Costanzo, I. Inbal, D. Danino, V. Ianniello, G. Ianniruberto, G. Marrucci, and N. Grizzuti. On the startup behavior of wormlike micellar networks: The effect of different salts bound to the same surfactant molecule. *Journal of Rheology*, 67(2):353–364, Mar 2023. doi: 10.1122/8.0000537.

[47] V. Vitali, G. Nava, G. Zanchetta, F. Bragheri, A. Crespi, R. Osellame, T. Bellini, I. Cristiani, and P. Minzioni. Integrated optofluidic chip for oscillatory microrheology. *Scientific Reports*, 10(1):5831, 2020. doi: 10.1038/s41598-020-62628-1.

[48] V. Vitali, G. Nava, A. Corno, M. Pezzotti, F. Bragheri, P. Paiè, R. Osellame, M. A. Ortenzi, I. Cristiani, P. Minzioni, T. Bellini, and G. Zanchetta. Yield stress "in a flash": investigation of nonlinearity and yielding in soft materials with an optofluidic microrheometer. *Soft Matter*, 17:3105–3112, 2021. doi: 10.1039/D0SM02168G.

[49] A. K. Gurnon, C. R. Lopez-Barron, A. P. R. Eberle, L. Porcar, and N. J. Wagner. Spatiotemporal stress and structure evolution in dynamically sheared polymer-like micellar solutions. *Soft Matter*, 10:2889–2898, 2014. doi: 10.1039/C3SM53113A.

[50] P. Edera, M. Brizioli, G. Zanchetta, G. Petekidis, F. Giavazzi, and R. Cerbino. Deformation profiles and microscopic dynamics of complex fluids during oscillatory shear experiments. *Soft Matter*, 17:8553–8566, 2021. doi: 10.1039/D1SM01068A.

[51] G. Zanchetta, E. Rocchi, and L. Piazza. Seeing is believing: Coupling between liquid crystalline ordering and rheological behaviour in cellulose nanocrystals suspensions. *Chemical Engineering Transactions*, 57:1933–1938, 2017. doi: 10.3303/CET1757323.

[52] S. Villa, P. Edera, M. Brizioli, V. Trappe, F. Giavazzi, and R. Cerbino. Quantitative rheo-microscopy of soft matter. *Frontiers in Physics*, 10, 2022. doi: 10.3389/fphy.2022.1013805. URL `https://www.frontiersin.org/journals/physics/articles/10.3389/fphy.2022.1013805`.

[53] R. H. Ewoldt, M. T. Johnston, and L. M. Caretta. *Experimental Challenges of Shear Rheology: How to Avoid Bad Data*, pages 207–241. Springer New York, New York, NY, 2015. ISBN 978-1-4939-2065-5. doi: 10.1007/978-1-4939-2065-5_6.

[54] S. Russo Spena, B. Visone, and N. Grizzuti. An engineering approach to the 3d printing of k-carrageenan/konjac glucomannan hydrogels. *International Journal of Food Science & Technology*, 59(6):4122–4133, 2024. doi: 10.1111/ijfs.17170.

[55] C. W. Macosko. *Rheology: Principles, Measurements, and Applications*. Wiley - VCH Publishers, New York, 1994.

[56] D. Y. Zhang and M. A. Calabrese. Temperature-controlled dripping-onto-substrate (dos) extensional rheometry of polymer micelle solutions. *Soft Matter*, 18:3993–4008, 2022. doi: 10.1039/D2SM00377E.

[57] K. T. Lauser, A. L. Rueter, and M. A. Calabrese. Small-volume extensional rheology of concentrated protein and protein-excipient solutions. *Soft Matter*, 17:9624–9635, 2021. doi: 10.1039/D1SM01253C.

[58] J.-B. Boitte, C. Vizcaïno, L. Benyahia, J.-M. Herry, C. Michon, and M. Hayert. A novel rheo-optical device for studying complex fluids in a double shear plate geometry. *Review of Scientific Instruments*, 84(1), 2013. ISSN 0034-6748. doi: 10.1063/1.4774395.

[59] D. Danino. Cryo-tem of soft molecular assemblies. *Current Opinion in Colloid & Interface Science*, 17(6):316–329, 2012. ISSN 1359-0294. doi: https://doi.org/10.1016/j.cocis.2012.10.003.

[60] V. Calabrese, A. Q. Shen, and S. J. Haward. How do polymers stretch in capillary-driven extensional flows? *Macromolecules*, 2024. doi: 10.1021/acs.macromol.4c01604.

[61] D. Y. Zhang and M. A. Calabrese. Temperature-controlled dripping-onto-substrate

(dos) extensional rheometry of polymer micelle solutions. *Soft Matter*, 18:3993–4008, 2022. doi: 10.1039/D2SM00377E.

[62] D. Gaudino, S. Costanzo, G. Ianniruberto, N. Grizzuti, and R. Pasquino. Linear wormlike micelles behave similarly to entangled linear polymers in fast shear flows. *Journal of Rheology*, 64(4):879–888, 2020. doi: 10.1122/8.0000003.

[63] B. Wen, B. Bai, and R. G. Larson. Surfactant desorption and scission free energies for cylindrical and spherical micelles from umbrella-sampling molecular dynamics simulations. *Journal of Colloid and Interface Science*, 599:773–784, 2021. ISSN 0021-9797. doi: 10.1016/j.jcis.2021.04.138.

[64] E. Lifshitz, A. Kosevich, and L. Pitaevskii. Chapter i - fundamental equations. In *Theory of Elasticity (Third Edition)*, pages 1–37. Butterworth-Heinemann, Oxford, third edition edition, 1986. doi: 10.1016/B978-0-08-057069-3.50008-5.

[65] T. Shikata, S. J. Dahman, and D. S. Pearson. Rheo-optical behavior of wormlike micelles. *Langmuir*, 10(10):3470–3476, 1994. doi: 10.1021/la00022a019.

[66] P. A. Vasquez, G. H. McKinley, and L. Pamela Cook. A network scission model for wormlike micellar solutions: I. model formulation and viscometric flow predictions. *Journal of Non-Newtonian Fluid Mechanics*, 144(2):122–139, 2007. ISSN 0377-0257. doi: 10.1016/j.jnnfm.2007.03.007.

[67] E. Miller and J. P. Rothstein. Transient evolution of shear-banding wormlike micellar solutions. *Journal of Non-Newtonian Fluid Mechanics*, 143(1):22–37, 2007. ISSN 0377-0257. doi: 10.1016/j.jnnfm.2006.12.005.

[68] J.-F. Berret. *Rheology of Wormlike Micelles: Equilibrium Properties and Shear Banding Transitions*, pages 667–720. Springer Netherlands, 2006. ISBN 978-1-4020-3689-7. doi: 10.1007/1-4020-3689-2_20.

[69] S. A. Rogers, M. A. Calabrese, and N. J. Wagner. Rheology of branched wormlike micelles. *Current Opinion in Colloid & Interface Science*, 19(6):530–535, 2014. ISSN 1359-0294. doi: 10.1016/j.cocis.2014.10.006.